

Preparation and Detection of Ytterbium Rydberg Atoms and Molecules

Florian Pausewang

Masterarbeit in Physik
angefertigt im Institut für Angewandte Physik

vorgelegt der
Mathematisch-Naturwissenschaftlichen Fakultät
der
Rheinischen Friedrich-Wilhelms-Universität
Bonn

April 2025

I hereby declare that this thesis was formulated by myself and that no sources or tools other than those cited were used.

Bonn,
Date

.....
Signature

- 1. Supervisor: Prof. Dr. Sebastian Hofferberth
- 2. Supervisor: Prof. Dr. Daqing Wang

Contents

1	Introduction	1
2	Ultracold ytterbium Rydberg atoms	3
2.1	Preparation of ultracold ytterbium atoms	4
2.2	Rydberg excitation	7
2.3	Detection schemes of Rydberg atoms	9
2.3.1	Rydberg state detection by few-photon probing	9
2.3.2	Rydberg state detection by ionization	10
2.3.2.1	Electric field control	10
2.3.2.2	MCP - Working principle and characterization	16
2.3.2.3	Further characterization of the ion detection	22
2.4	Experimental sequence	26
3	Ytterbium Rydberg atoms in electric fields	28
3.1	Field ionization of ytterbium Rydberg atoms	28
3.2	Two-photon ionization of ytterbium	35
3.3	AC and DC Stark shifts of ytterbium	40
3.3.1	Static dipole polarizability	40
3.3.2	Light shift of the Control laser	43
4	Ultralong-range ytterbium Rydberg molecules	46
4.1	Introduction to Rydberg molecules	46
4.2	Measurement considerations	49
4.3	Spectroscopy of Rydberg molecules	52
4.4	Permanent electric dipole moment of Rydberg molecules	57
5	Towards Rydberg nonlinear quantum optics	62
6	Conclusions	66
A	Appendix: Details on fitting Rydberg molecule spectra	68
B	Details on the Rydberg excitation in a cloud simulation	74
	Bibliography	77
	List of Abbreviations	84

Introduction

The ability to manipulate and control individual single photons is a primary goal in the broader field of applied quantum science and in quantum optics [1, 2]. In the domain of nonlinear quantum optics, the subject of this thesis, the primary challenge lies in the generation of effective photon-photon interactions through strong coupling to matter and well controllable tunability of the light-matter interaction [3, 4]. Achieving this objective is of paramount importance for the fundamental exploration of the frontiers of quantum physics. Furthermore, it is a critical component of the development of next-generation quantum applications, such as the quantum-by-quantum control of light fields, single-photon switches and transistors, all-optical deterministic quantum logic, and the realization of strongly correlated states of light and matter [4].

One possible approach to this issue is by addressing it with *Rydberg* nonlinear quantum optics. This field utilizes the strong atom-atom interaction between Rydberg states $|r\rangle$ in a two-photon excitation scheme to create strong nonlinearities in an optical medium [3–5]. The central elements underlying this approach are as follows: Firstly, using atoms that are highly excited to metastable states, so called Rydberg atoms. These exhibit exaggerated sizes, polarizabilities, and lifetimes [6], resulting in long-range, van-der-Waals dipole-dipole interactions between individual Rydberg atoms. That gives rise to a blockade mechanism: A single Rydberg excitation suppresses further excitations to Rydberg states within a given Rydberg blockade radius [7–9]. Secondly, employing the effect of electromagnetically induced transparency (EIT) in a 3-level excitation scheme. EIT is observed as transparency of a resonant two-photon transitions in a medium and is created by destructive interference of the quantum mechanical transition amplitudes [10]. Another characteristic effect related to EIT is a slow group velocity in the medium [11]. These two mechanisms facilitate the propagation of photons through the atomic medium by forming so-called Rydberg dark-state polaritons. These are - due to the Rydberg character - interacting quasi-particles comprised of light and collective atomic excitations [3, 12]. After a first demonstration in [13] this concept was applied in multiple groups and experiments worldwide [5, 14, 15].

Our ytterbium quantum optics (YQO) experiment [16, 17] at the University of Bonn contributes to this field by striving to realize photon-photon interactions in an elongated (one-dimensional) cloud of ultracold Rydberg ytterbium atoms. A comprehensive theoretical framework for such few- and many-body interacting quantum systems has already been established in reference [18, 19]. It is anticipated that the employment of the alkaline-earth-like element ytterbium will yield substantial benefits. In particular, a spin wave, created by a two-photon collective Rydberg excitation, will evolve in the medium with a dephasing dependent on the wave vector mismatch and the temperature dependent atom movement

[20]. Compared to other species, for ytterbium a longer coherence time of the spin wave is expected: The wavelengths involved in excitation (399 nm, 395 nm) are similar, resulting in a reduced wave vector mismatch and a diminished imprinted momentum. Furthermore, the ability to apply efficient cooling schemes by utilizing the atomic transitions of ytterbium allows low temperatures and can reduce motional dephasing. In the YQO experiment, we use the simplest isotope ^{174}Yb . It is bosonic with zero nuclear spin resulting in a ground state with the quantum numbers $J = F = I = S = L = 0$. The atomic closed-shell electronic structure, in conjunction with the absence of hyperfine splitting, facilitates an easy state preparation and the narrow intercombination transitions enable effective laser cooling and trapping [21]. The YQO setup combines a double-MOT system with optical dipole trapping to enable high atom numbers and low temperatures. These are ideal conditions for conducting versatile Rydberg-mediated nonlinear quantum optics experiments. The present experiment is specifically designed to investigate the utilization of ^{174}Yb from the standpoint of Rydberg nonlinear quantum optics.

However, additional research opportunities with our setup exist in the broader domain of atomic and molecular physics pertaining to ^{174}Yb in a dense atomic gas. The physics of the Rydberg states of the atomic element ytterbium has yet to be thoroughly characterized in many aspects. While the lower-lying states of ytterbium have been thoroughly characterized through spectroscopic analysis [22–24], experimental characterizations of the properties of ytterbium Rydberg states, such as the ionization behavior in electric fields [25] or Multi-Channel Quantum Defect (MCQDT) related effects [26, 27], are still open and of fundamental interest [26].

In the course of my thesis work, the YQO apparatus was upgraded with a field ionization system that employed ion detection via a Microchannel plate (MCP). A substantial portion of this thesis will be dedicated to the optimization and characterization of this detection scheme. While the technique is standard, theoretically established [6, 28] and employed in several Rb-based experiments [29–31], the implementation with ^{174}Yb revealed the unexpected ability to ionize low-lying Rydberg states. This enabled state-selective detection of Rydberg excitations over a wide range Rydberg states. This thesis demonstrates the application of the ion detection for high-precision spectroscopy, achieving an excellent signal-to-noise ratio in dense Rydberg ensembles. The following applications are of particular note: the characterization of AC- and DC Stark shifts¹, the polarizability resonance [26] of ^{174}Yb and the investigation of ultralong-range Rydberg molecules. Such exotic molecules are a unique class of ultra-long-range bound states formed when a highly excited Rydberg electron scatters with one or more neutral ground-state atoms. Their formation was not yet observed in an ytterbium gas.

In this thesis, I start by introducing the experimental apparatus and techniques in chapter 2, with a clear focus on the ionization setup and the ion detection system. Then, in chapter 3, I present experimental results on the behavior of ^{174}Yb in electric fields. This chapter provides an overview of the ionization dynamics observed in the experimental setup focusing on the mechanisms of field and photoionization. In addition, the energy level shifts that occur in static and optical electric fields are discussed. In chapter 4, I discuss measurements contributing to the characterization of the scattering processes leading to Rydberg molecules. This chapter also includes the measurement of their permanent electric dipole moment. Finally in chapter 5, I conclude this thesis with an outlook on the future research steps in the lab, with focus on Rydberg nonlinear quantum optics with ^{174}Yb .

¹ The Stark effect is named after Johannes Stark - undoubtedly one of the most famous and infamous „Nazi“ scientists [32]. This footnote is intended to raise awareness of this historical fact.

Ultracold ytterbium Rydberg atoms

As motivated in chapter 1, the aim of the YQO-experiment is spectroscopy of ^{174}Yb Rydberg states and Rydberg nonlinear optics. The key steps towards this goal are discussed in this chapter. The used excitation scheme to Rydberg states is presented in section 2.2, the requisite for this step - the preparation of ultracold ytterbium is explained in detail in section 2.1, and technical details on the detection of Rydberg atoms are highlighted in section 2.3.1 with a focus on the ion detection system. I will start with presenting fundamentals on the Rydberg physics of ^{174}Yb required for the scope of this thesis.

Introduction to Rydberg physics. In this work the properties of highly excited, metastable atomic states, so called Rydberg states, with large principle quantum numbers between $n = 30$ and $n = 100$ are studied. Rydberg atoms can be approximated as a positive charged atomic core and an electron in a distance R . The effect of the internal structure can be approximated by a quantum defect $\mu(n)$ and many species behave similar to Hydrogen [6].

Many properties of the Rydberg atoms scale in first order with the effective principal quantum number $\nu = n - \mu(n)$, e.g. the wavefunction radius $\propto \nu^2$, the energy spacing between $|n\rangle$ and $|n+1\rangle \propto \nu^{-3}$, the lifetime $\propto n^3$ the transition dipole matrix element $\propto \nu^{-3/2}$. Effects emerging through a non-vanishing second-order perturbation in dipole-dipole coupling scale even more extreme: The C_6 coefficients¹ $\propto \nu^{11}$ and the static dipole polarizability² $\propto \nu^7$ [6]. These simple scalings will be reflected in many measurements during the scope of this thesis (cf. chap. 3, 4). Since Rydberg atoms have large n , they exhibit large polarizabilities, lifetimes, and sizes and in contrast small binding energies close to the ionization threshold.

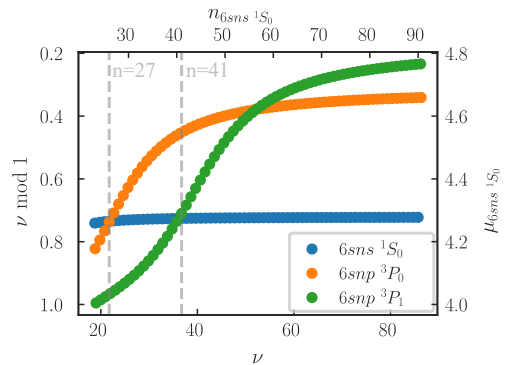


Figure 2.1: Lu-Fano-like plot of selected S and P series of $6snl_{\text{ryd}} \text{ } ^{174}\text{Yb}$. For each series, the fractional part of the quantum defect is plotted versus the effective principal quantum number ν . A second set of axis shows the corresponding principal quantum number n and the quantum defect $\mu = n - \nu$. Calculation was done with *pairinteraction* [27].

¹ The C_6 coefficients determine the blockade radius (cf. eq. 5).

² The static dipole polarizability determines the DC-Stark shift (cf. eq. 3.13).

However, in ^{174}Yb due to the two-valence electron structure, many of these properties feature deviations due to resonances and state mixing [26]. E.g., the Lu-Fano-like plot in figure 2.1 shows a crossing of the quantum defects of the S -series with each of the P -series at $n = 41$ and $n = 27$, resulting in a polarizability resonance at $n = 41$ [26]. A measurement of this effect is presented in cap. 3.3.

2.1 Preparation of ultracold ytterbium atoms

A cold ensemble of ^{174}Yb atoms provides the foundation for performing further Rydberg quantum optics experiments. In this section the two main atom cooling techniques are introduced: Firstly, laser cooling in a magneto-optical trap (MOT), and secondly, evaporative cooling in a dipole trap. In this experiment, a double MOT setup to prepare cold ensembles of ^{174}Yb atoms is utilized: a 2D MOT as atomic source and a 3D two-color MOT for cooling in the science chamber. Additional evaporation and compression in a dipole trap are used to reach the desired densities. The system is described and characterized in [16, 17]. This section provides selected information and details about the atom cloud preparation, that are required for the following chapters of this thesis.

Double-MOT setup for low temperature laser cooling

Laser cooling basics. The fundamental principle of laser cooling of neutral atoms exploits momentum conservation during the absorption and spontaneous emission process of atoms and photons with quantized momenta $p = \hbar k$ (with wave vector $k = \frac{2\pi}{\lambda}$ and wavelength λ), resulting in an atomic recoil in the photon's emission direction [33–36]. In a two-level system, atoms moving with velocity v_z towards the laser beam can be selectively decelerated via Doppler cooling using the scattering force

$$F_{\text{scatt}} = \frac{\hbar k \Gamma}{2} \frac{I/I_{\text{sat}}}{1 + I/I_{\text{sat}} + \frac{4\Delta^2}{\Gamma^2}} \quad [34],$$

where I is the laser intensity, I_{sat} the saturation intensity, Γ the natural linewidth, and Δ the laser detuning. The resulting decelerating force from two counter-propagating beams along the axis z in one dimension is $F_{\text{molasses}} = -\alpha v_z$, where α is a damping coefficient.

Simultaneous to cooling the atoms, trapping the cooled atoms is achieved using a Magneto-Optical Trap (MOT), which employs the magnetic field gradient from a quadrupole field generated by a pair of coils in anti-Helmholtz configuration, that shifts atomic energy levels via the Zeeman effect. The combined velocity- and position-dependent force along each beam propagation axis z is

$$F_{\text{MOT}} = -\alpha v_z - \alpha \beta_z z \quad \text{with} \quad \alpha = 4\hbar k^2 \frac{I}{I_{\text{sat}}} \frac{-2\Delta/\Gamma}{\left(1 + (2\Delta/\Gamma)^2\right)^2} \quad \text{and} \quad \beta_z = \frac{g\mu_B}{\hbar} \frac{dB}{dz} \quad [34].$$

where g is the Landé-factor and μ_B the Bohr magneton. Applying this force with for beams in 2 dimensions results in a transversal cooling along one axis, a 2D MOT. Extending this technique to three dimensions creates "optical molasses" [35], which slows and confines atoms within a volume at the intersection of the three pairs of counter-propagating beams. This is called a 3D MOT.

During the cooling process the competition between laser cooling and diffusion heating through the random nature of spontaneous emission, the lowest temperature that can be achieved for two-level atoms

without using sub-Doppler cooling is the Doppler temperature $T_D = \frac{\hbar\Gamma}{2k_B}$ [36].

Laser cooling of ^{174}Yb . The in this experiment used isotope ^{174}Yb has no hyperfine structure. Therefore, sub-Doppler cooling techniques used for other Yb isotopes, can not be implemented with ^{174}Yb [36]. Cooling ^{174}Yb requires an advanced cooling scheme, using multiple cooling stages.

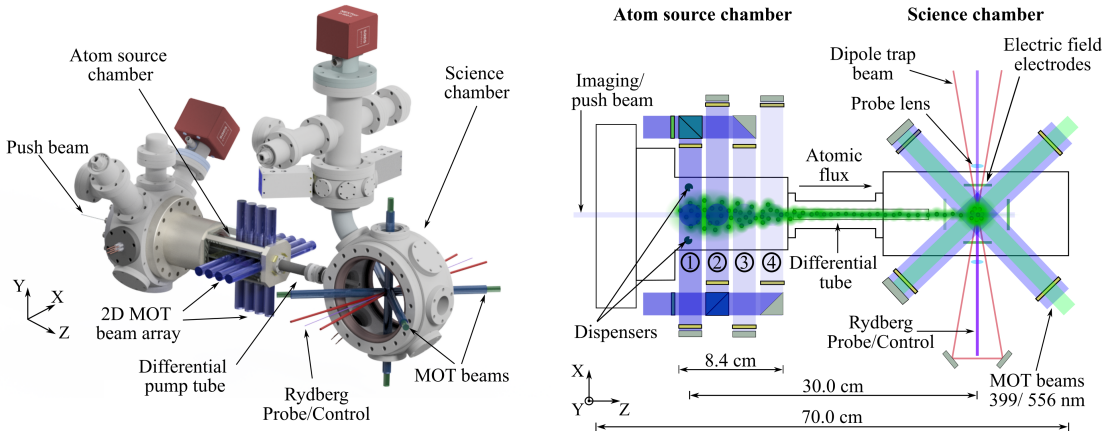


Figure 2.2: Overview over the atom preparation setup. A 3D drawing of the dual-chamber vacuum system and a cut through the xy-plane of the experimental setup is shown. Included are the laser configurations for the 2D MOT, push beam, two-color 3D MOT, dipole trap, and Rydberg excitation. Adapted from [16].

The cooling scheme for the alkaline-earth like atom ^{174}Yb benefits from the existence of intercombination transitions between singlet and triplet states and relies on two transitions (cf. fig. 2.3): A *blue* singlet transition $^1S_0 \rightarrow ^1P_1$ at a wavelength of 399 nm with a broad linewidth, and a *green* intercombination line $^1S_0 \rightarrow ^3P_1$ at 556 nm with a comparably narrow linewidth of $\Gamma_{556} = 2\pi \times 182$ MHz. The velocity capture range Δv of a MOT scales with the linewidth Γ of the atomic excited state [36]. The broad blue transition is used for initial trapping. Precooling the atoms in the blue MOT allows recapturing them in the green MOT. To reach low Doppler temperatures, the green transition allows cooling down to a theoretical limit of $T_{D,556} \approx 4 \mu\text{K}$. In summary: A two-color MOT is an optimal combination.

The experimental setup for the cooling procedure of ^{174}Yb atoms comprises two separate vacuum chambers connected by a differential pumping tube (cf. fig. 2.2): In an *atom source chamber* atoms are dispenser-loaded and transversally cooled using blue 2D MOT. The chamber houses four dispenser-based Yb atom sources continuously emitting atoms. The transverse cooling of the atoms is facilitated using a magnetic field gradient generated by permanent magnets and four pairs of retroreflected, resonant 395 nm beams arranged in a cross. Once cooled transversally, the atoms travel through a narrow differential pumping tube that separates the two chambers, guided by a weak "push" laser beam along the longitudinal axis to enhance the transfer into the science chamber. The *science chamber* hosts the two-color 3D MOT. Large optical

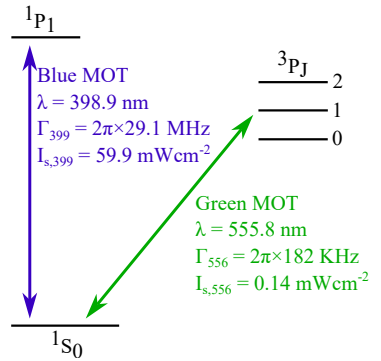


Figure 2.3: Relevant cooling transitions and their properties. Adapted from [16].

windows allow feature good optical access that enable dipole trapping, further excitation to Rydberg states and imaging systems. The differential pumping tube isolates this chamber from background gas of the atom source chamber, maintaining ultra-high vacuum (UHV) conditions necessary for long atom trapping lifetimes. In addition, the science chamber is equipped with an electric field control, electrodes for ion optics, and an ion detector.

Putting all of these concepts together results in a three-stage cooling sequence. Figure 2.4 shows an overview. The process begins with the *Blue 3D MOT Stage*. This phase runs concurrently with the 2D MOT and the push beam. The atoms arriving from the 2D MOT are captured using light resonant blue light. This stage is optimized for the highest atom number and runs for several seconds until the atom number saturates. Shelving in 3P state with green light increases atom number in blue 3D MOT by a factor 1.8. The temperature of atoms is now about 15 mK. After initial loading, in a *Blue-Green Transition Stage*, stage optical and magnetic parameters are gradually adjusted to facilitate a smooth handover to the green MOT. The intensity of the blue laser beams is reduced, while the green 556 nm beams are introduced. During this stage, the green laser frequency is broadened to increase the capture range of atoms, ensuring a maximum transfer efficiency into the next stage. In the final *Green MOT Stage*, the system operates with only the green MOT. This phase is optimized to further cool the atoms reaching a thermal equilibrium at temperatures far below the blue Doppler temperature.

To summarize: Such two-color double MOT cooling scheme enables both high atom numbers and low temperatures. In numbers: The setup produces a cloud of $\approx 1.8 \cdot 10^7$ ^{174}Yb atoms at a temperature below 10 μK in typically 2.5 s.

Evaporative cooling and compression

Even lower temperatures and high densities can be reached by employing an optical dipole trap for evaporative cooling and compression.

Dipole trap basics. An optical dipole trap relies on the optical dipole force [37]. Laser light (with an electric field amplitude $E = E \cdot \exp(-i\omega t)$ and intensity $I = 2\epsilon_0 c |E|^2$) induces an atomic dipole moment $p = \alpha E$ that oscillates with the driving frequency ω . α is the complex polarizability of the atom. The interaction of the induced dipole moment p and the driving field E is given by the potential U_{dip} . U_{dip} is proportional to the field intensity I and the real part of the polarizability $\Re(\alpha)$, which represents the in-phase component of the dipole oscillation and governs the dispersive properties of the interaction [37]. The resulting conservative force, the dipole force, is proportional to the intensity

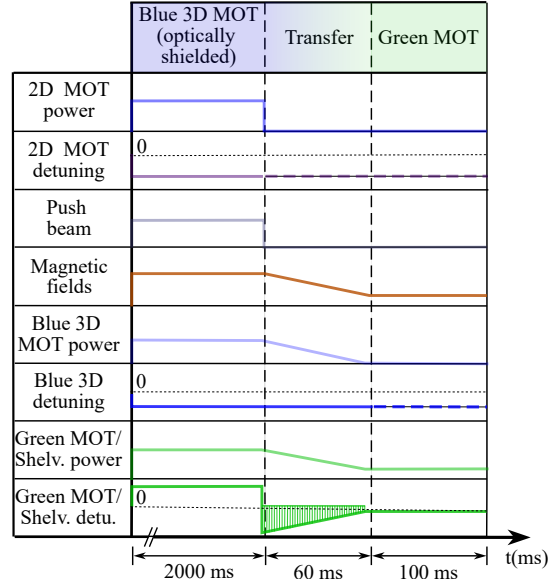


Figure 2.4: Visualization of the loading sequence for the two-color 3D MOT. The sequence includes stages for broad-linewidth blue MOT, atom transfer, and narrow-linewidth green MOT. Adapted from [16].

gradient, attractive towards intensity maxima for red detuning $\Delta < 0$, and given by

$$\mathbf{F}_{\text{dip}}(\mathbf{r}) = -\nabla U_{\text{dip}} = \frac{1}{2} \langle pE \rangle = -\frac{1}{2\epsilon_0 c} \Re(\alpha) \cdot \nabla I(\mathbf{r}) \quad [37].$$

To enable a trapping with minimal loss, so trapping with a low scattering rates and a high potential depth a far red-detuned laser is used, exploiting that the dipole potential scales as I/Δ , whereas the scattering rate scales as I/Δ^2 .

Consecutive evaporation of atoms at high temperatures is employed to achieve colder temperatures, albeit with strong atom loss. This is achieved through the adiabatic reduction of the trap depth by decreasing the power of dipole trap light. Conversely, a subsequent ramp-up of the dipole trap light power can be employed to enhance the confinement of the atoms. This compression of the atom cloud increases density and is accompanied by a rise in temperature.

^{174}Yb in a dipole trap. A 1070 nm laser at a high intensity of $I = 1$ to 14 W can be used to trap ^{174}Yb atoms. After the MOT stages, the atoms are transferred into a crossed beam dipole trap. This transition is accompanied by a further compression of the MOT. By evaporating 90 % of the atoms, temperatures below 1 μK can be reached.

A 10 s evaporation down to followed by a 100 ns compression results in a cloud with the density $\rho = 3.18 \times 10^{14} \text{ cm}^{-3}$, atom number $N = 7.5 \times 10^5$, and temperature $T = 4 \mu\text{K}$.

2.2 Rydberg excitation

Subsequent to the preparation of the cold atomic cloud, a Rydberg excitation of the atoms ensues. Excitation to Rydberg states is challenging due to the small overlap of groundstate $|g\rangle$ and Rydberg state $|r\rangle$ caused by the dipole matrix elements scaling with $\nu^{-3/2}$, and the required deep-uv photons for a single-photon transition. This challenge can be resolved by utilizing an excitation pathway through an intermediate state $|e\rangle$. Specifically, in our scheme, the ^{174}Yb atoms are excited from the ground state $|g\rangle = |6s^2 \ ^1S_0\rangle$ via a two-photon transition over the intermediate state $|e\rangle = |6s6p \ ^1P_1\rangle$ to Rydberg states $|r\rangle = |6sns \ ^1S_0\rangle$. This is illustrated in figure 2.5. A weak *Probe*, at $\lambda_P = 399 \text{ nm}$, field drives the transition $|g\rangle \rightarrow |e\rangle$ and a strong *Control* field, at $\lambda_C = 395$ to 398 nm, the transition $|e\rangle \rightarrow |r\rangle$. Excitation to the Rydberg state is possible, as the big dipole matrix element of $|g\rangle \rightarrow |e\rangle$ allows a weak Probe, and the small dipole matrix element $|e\rangle \rightarrow |r\rangle$ is compensated by a strong Control field with a high Rabi frequency Ω_C . This three level-scheme is shown in fig. 2.5.

In this excitation scheme is $\lambda_P \approx \lambda_C$, $\Omega_C \gg \Omega_P$, and we operate usually at two-photon detuning $\delta \rightarrow 0$, the "EIT"-case, or in the far off-resonant case with $\delta = 1 \text{ GHz}$, the Raman-case. In the latter one, the two-photon excitation via a virtual state is more

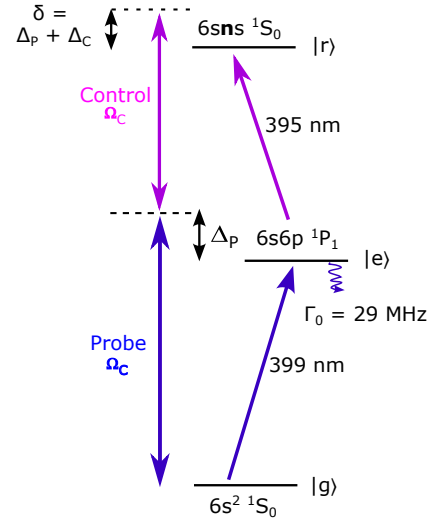


Figure 2.5: Level scheme for Rydberg excitation to a state $6sns \ ^1S_0$ with the Probe and Control wavelengths $\lambda_P \approx \lambda_C$ and their Rabi frequencies $\Omega_C \gg \Omega_P$. The single photon detunings Δ add up to a two photon detuning δ .

probable than the single photon excitation to the intermediate state since $\Delta \gg \Omega_P, \Omega_C$. Additionally, due to the large Control detuning Δ_C changing the Probe detuning Δ_P by small values is equivalent to changing the two-photon-detuning δ . The levels $|g\rangle$ and $|r\rangle$ can be considered as an effective two-level system with Rabi frequency of

$$\Omega_{\text{eff}} = \frac{\Omega_P \Omega_C}{4\Delta} \quad [38].$$

The "EIT"-case will be discussed in chapter 5. In our experimental scheme Probe and Control are counter-propagating with circular polarization resulting in a small absorbed momentum.

2.3 Detection schemes of Rydberg atoms

In the experiment, two complementary detection methods are used to study the Rydberg excitation dynamics in the atomic cloud: The transmission of the Probe beam and the ionizing the Rydberg atoms for selective detection. With the first method, the interaction of the weak probe beam with the atoms can be detected with single photon counters, as I will discuss in section 2.3.1. With the second method, a high-voltage ionization field is applied to ionize the Rydberg atoms, which are then guided to a Micro Channel Plate (MCP) detector. An in-depth discussion of the method of Rydberg state detection by ionization will be given in section 2.3.2.

2.3.1 Rydberg state detection by few-photon probing

The first detection method of Rydberg excitations in our experiment is to measure the transmission of the Probe beam through the atomic cloud. Recalling the two-photon Rydberg excitation scheme presented in section 2.2, the Probe beam drives the lower transition at 399 nm with an intensity of a few photons per pulse. In this detection scheme, one can detect the transmission of those single photons while usually varying the detuning Δ_P , similar to a classical spectroscopy measurement.

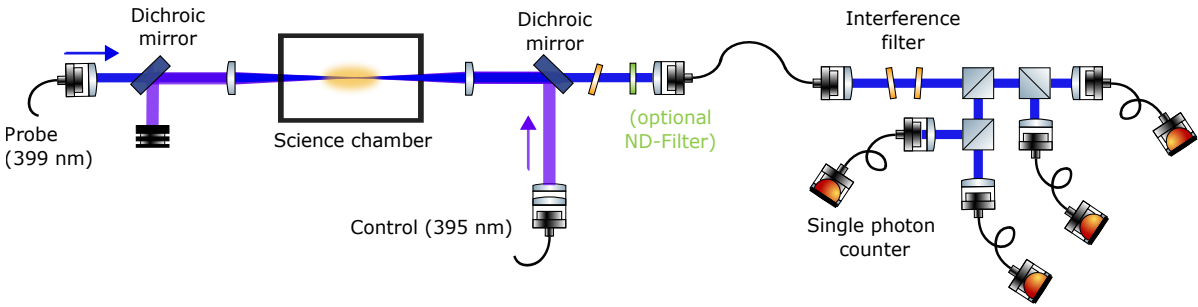


Figure 2.6: Few photon detection setup. Probe and Control beam are counter-propagating through the atomic ensemble. The Probe and Control beams are separated by dichroic mirrors and interference filters to reduce the control photons back-scattering towards the single photon detectors. A Hanbury Brown-Twiss setup is connected via a single-mode fiber. The four single photon detectors are multi-mode fiber coupled. If a measurement with higher Probe power is performed, additional ND-filters can be inserted to not damage the single photon counters.

However, contrary to classical spectroscopy, at the few-photon levels spectroscopy is challenging as it becomes very susceptible to small sources of noise. This is caused by the fact, that in our detection scheme, we utilize the transmission as a tool to indirectly measure absorption of the medium. A fundamental noise limit is given by the inherent quantum nature of light, the photon shot noise. Its impact can only be reduced by averaging over a large number N of independent trials resulting in fluctuations. Here the signal-to-noise ratio (SNR) scales with $N/\sqrt{N} = \sqrt{N}$. In addition to this dominant quantum noise, the detectors show unavoidable technical noise, e.g. due to dark counts or stray light. The full spectroscopy setup may experience shot-to-shot fluctuations, mostly due to laser intensity noise or the instabilities of the atomic ensemble. All of these noise sources contribute to the SNR.

It is fundamental for this detection scheme to be able to reconstruct the number of photons that interact with the atoms per pulse from the transmission measurement. This is achieved by calibrating the detection efficiency of the setup, shown in figure 2.6. Photon loss occurs in the following steps: The Probe photons are collected with a single mode fiber, filtered with loss in frequency via interference

filters that separate 399 nm Probe and 395 nm Control light, and collected by single photon counting modules. The detection efficiency is given by $\eta_{\text{tot}} = \eta_{\text{col}} \cdot \eta_{\text{Q}}$ where η_{Q} is the quantum efficiency of the detectors and η_{col} is the collection efficiency of the photons from the experiment. The former is provided by the manufacturers and cannot be verified by our means. The four used single photon counters ³ have quantum efficiencies of 50.8 to 55.3 %. The latter can be estimated by measuring the transmission of a classical intensity beam. The major photon losses are: 6 % at the glass cell window, 40 % at the first single-mode fiber coupling, 20 % at each of the two interference filters, and 20 % at the last multi-mode fiber coupling. Additionally, with our current configuration ND-filters have to be inserted when operating at high Probe powers. This is required to increase the signal for the ion detection at low Rydberg states and increases the overall loss drastically.

Overall (without the additional optional ND-Filters), this leads to a total detection efficiency of $\eta_{\text{tot}} \approx 10$ %. This efficiency limits the sensitivity of the setup for spectroscopy purposes. Nevertheless, a precise calibration of the single photon counting system is possible and will be of use to calibrate the absolute ion detection efficiency in the next section.

2.3.2 Rydberg state detection by ionization

In contrast to the detection method with single photons, the Rydberg state detection by ionization allows the direct measurement of Rydberg excitations via an ion signal with a high SNR reducing the number of repetitions required. This section gives a detailed overview of the technical aspects of the ion detection system. The two main components are the electric field control (cf. sec. 2.3.2.1) and the ion detector, which consists of a microchannel plate (MCP) (cf. sec. 2.3.2.2).

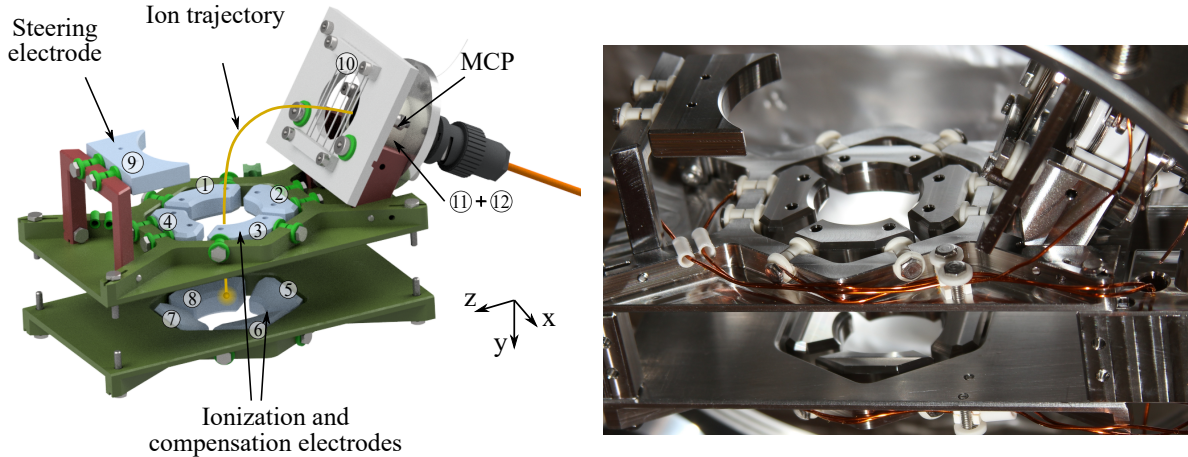
2.3.2.1 Electric field control

The two main objectives of the electric field control system are:

- Shielding the atoms from external electric fields, thereby reducing line broadening and mitigating dephasing mechanisms. Since the static dipole polarizability α of the n^1S_0 Rydberg states scales with the effective principal quantum number ν^7 [9], it is significantly larger than that of lower-lying excited states. Consequently, Rydberg atoms are very sensitive to stray electric fields. In addition, as described in section 3.3.1, the high degree of control on electric fields at the atoms can be used to measure DC Stark shifts.
- Controlling Rydberg excitations in the atomic cloud. Created Rydberg atoms will interact strongly with surrounding atoms (cf. chap. 5) and the number of Rydberg atoms will change the response of the atomic cloud to excitation fields. The lifetime τ scales with n^3 [9]. Applying high electric fields will ionize Rydberg atoms and reset the number of excitations to 0 to avoid Rydberg pollution [39]. The ions produced by ionization can be detected by the MCP (cf. section 2.3.2.2). This detection method provides a direct measure of the presence of Rydberg states and allows the study of their dynamics.

Design and structure. The design of the electric field (E-field) control system is motivated by [40, 41] and was designed by Phillip Lunt [17]. The mechanical parts are illustrated in figure 2.7.

³ COUNT-100B-FC from [Laser Component](#)



(a) Sketch of the electric field related components.

(b) Picture of the inner parts of the science chamber.

Figure 2.7: Vacuum part of the electric field (E-field) control system. Probe and Control beam are parallel to the x-axis. The atom beam from the 2D-MOT is parallel to the z-axis. Electrodes 1-8 are in an octagonal configuration and voltages of up to ± 10 V can be applied. The ionization electrodes (6,8) and the steering electrode (9) can be switched to voltages of up to ± 500 V in less than $50 \mu\text{s}$. The front of the MCP (Electrode 11) is maintained at a constant voltage of -2 kV, while the back of the MCP (Electrode 12) is set to -2.5 kV. A mesh (Electrode 10) can be set to voltages up to ± 10 V. A trajectory of the ions to the MCP is sketched in yellow. The CAD model was created by previous YQOers and the picture was taken before full assembly of the vacuum chamber.

Eight electrodes in an octagonal configuration with a distance to the atom beam of 19.7 mm can compensate stray electric fields in arbitrary directions while allowing the application of homogeneous fields in x,y, and z direction at the center of the electrodes. For this, pairs of electrodes can be set to individual Voltages U_+ and U_- . Conversion factors from the voltage applied to the electrodes to the electric field at the center of the electrodes for all three axes are provided in tab. 2.1. The values were calculated with a Comsol simulation for a position centered between all electrodes. The conversion factors are dependent on the position of the atomic cloud. From scans of the fields of individual electrodes the resulting Stark shift of the atoms allows the estimation of the distance of the atoms to each electrode. The atomic cloud position is estimated to have a maximum (worst-case) displacement of 1 mm. In general, the conversion factor c_y for the configuration of the E-field E_y in y-direction, is best known as aligning the beams (and the position of the atomic trap) in y direction (the vertical axis) is experimentally easier compared to aligning the horizontal axes.

The systematic error on the field conversion factor in y-direction c_y due to atomic displacement can be estimated from figure 2.8 where c_y is plotted against the position y for no displacement of the atomic cloud as well as small displacements in x and z-direction. This error estimation is based on the assumption that the Comsol Simulation agrees well to the reality. The simulation does include only the components of the science chamber that are displayed in figure 2.7. Nor can the simulation capture small, accidental displacements of components during the assembly process that took place several years

ago. From figure 2.8, the uncertainties are

$$\begin{aligned}\Delta c &= \sqrt{(\Delta c_{x\text{-Displacement}})^2 + (\Delta c_{z\text{-Displacement}})^2} \\ &= \sqrt{(0.0038 \text{ (V/cm)/V})^2 + (0.0025 \text{ (V/cm)/V})^2} = 0.0045 \text{ (V/cm)/V} \quad .\end{aligned}$$

Table 2.1: Conversion factors c_i from applied voltage on electrodes to electric field for all three axes x, y, z . The field in axis i can be calculated as $E_{c,i} = c_i \cdot U$ with $U = U_+ = -U_-$ being the voltage applied to the corresponding electrodes. As electrode 1 has a malfunction, only one pair of electrodes is used for E_x . One pair of electrodes is used to create the high ionization field.

E-Field	Conversion Factor c ((V/cm) / V)	Electrodes at U_+	Electrodes at U_-
E_x	0.205	3 & 6	None
E_y	0.305 ± 0.005	2 & 4	5 & 7
E_z	0.35	2 & 5	4 & 7
$E_{\text{Ionization}}$	0.196	6 & 8	/

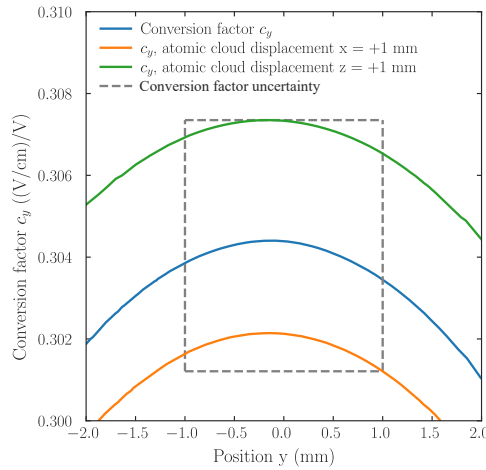


Figure 2.8: Conversion factor for electrodes in configuration for field E_y depending on the positions of the atomic cloud. With this *Comsol* simulation a systematical error on the calibration factor c_y can be estimated, based on the measurement that the cloud position deviates less than 1 mm from the center.

To apply high fields for ionization of atoms, electrodes 6 and 8 can be switched to positive high voltages (up to 500 V) within less than 30 ns and with electrode 9, the steering electrode, generated ions can be directed to the MCP. For this purpose, electrode 9 can be switched from ground to 500 V. Since the MCP is permanently set to a high voltage, it is well shielded and placed far away from the atoms. A mesh placed in front of the MCP can be set to a small negative voltage, e.g. -0.05 V, to provide additional shielding of the highly negative MCP and additional lensing and guidance of the ion beam.

The full connection from the computer control system to the electrodes in the vacuum via a feed-through is illustrated in diagram 2.9. The two main purposes are: Firstly, a high degree of control over the low voltage on each electrode during the Probe pulse, and secondly, the ability to quickly switch the

electrodes to a high electric field with a high repetition rate. To ensure a stability of the low voltage level, two snubber circuits were optimized on the low voltage input of the HV switch. Increasing the stability of the HV is challenging due to the requirement of precision at a high repetition rate. The next paragraph discusses this in detail.

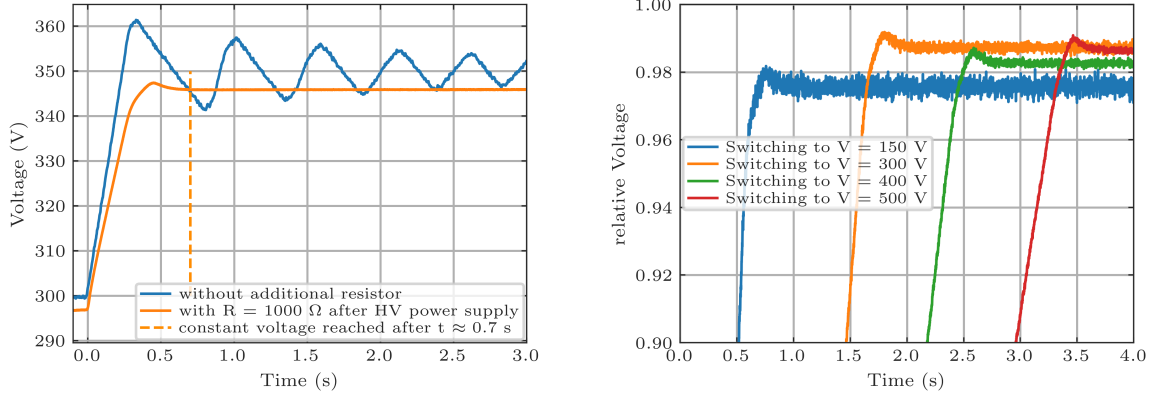
The HV power supplies do not operate properly under pulsed or rapidly changing loads. On short time scales, especially during a cycle, this means that when ionization and control are switched between high and low voltage, the electrodes are charged (current flows from PS to electrodes), and the power supplies must provide a higher power output. To reduce the resulting unstable voltage output, an additional capacitor with $C = 100 \mu\text{F}$ is connected in parallel to the HV PS. The capacitor provides a reservoir of electrons that stabilizes the voltage when a current flows to charge the electrodes. For safety reasons and to allow faster voltage changes, a large discharge resistor with $94 \text{ k}\Omega$ is connected in parallel. The maximum discharge time after switching on the HV power supply is $\tau_{1/e} = RC = 9.4 \text{ s}$. On larger time scales, especially between two cycles, this has implications: When the voltage output of the HV power supply changes, the $100 \mu\text{F}$ stabilization capacitor imposes a large capacitive load on the HV generator module. This large capacitance significantly slows down the response to step-like voltage changes, and additionally causes strong oscillations that cannot be regulated by the internal power supply PID (cf. fig. 2.10(a)). A possible solution is to insert a resistor R between the HV power supply and the capacitor to dampen or eliminate these oscillations. The resistor R should be chosen to achieve critical damping. For the observed oscillation frequency of 3 Hz , theoretically $R = \frac{1}{\omega C} = \frac{1}{2\pi \cdot 3 \text{ Hz} \cdot 100 \mu\text{F}} \approx 530 \Omega$ can be calculated as an optimal value, in the optimization process a resistance of $R_{\text{PS}} = 1000 \Omega$ was found to lead to a critical damping of the oscillations. This discrepancy can be explained by the fact that the HV power supply is part of the RC circuit, which makes the circuit with its internal components more complicated. Due to the constant discharge of the $100 \mu\text{F}$ capacitor, a current of $I_{\text{Discharge}} = 5 \text{ mA}$ must be supplied by the power supply in a steady state. A constant voltage of $U = R_{\text{PS}} I_{\text{Discharge}} = 5 \text{ V}$ will drop across the resistor $R_{\text{PS}} = 1000 \Omega$. Therefore, as shown in figure 2.10(b), 1 to 2 % of the voltage is not available for ionization and control.

The actual two-level switching of the low to high voltage signals is done with a commercial HV analog switch. Achieving optimal high-voltage switching performance for our purpose requires the following characteristics:

- short 10 to 90 % rise time,
- minimized oscillation at high voltage levels,
- stable high voltage across repeated pulses,
- rapid decay of the field after switching to low voltage,
- reduced oscillation at low voltage after switching, and
- functioning over a wide range of voltages.

To optimize the switching a resistor is added in series between the HV switch output and electrodes: For steering $R = 117 \Omega$ and for the two ionization channels $R = 93 \Omega$. The optimized switched signals⁴ are shown in figure 2.11(a). Summary for switching to 500 V :

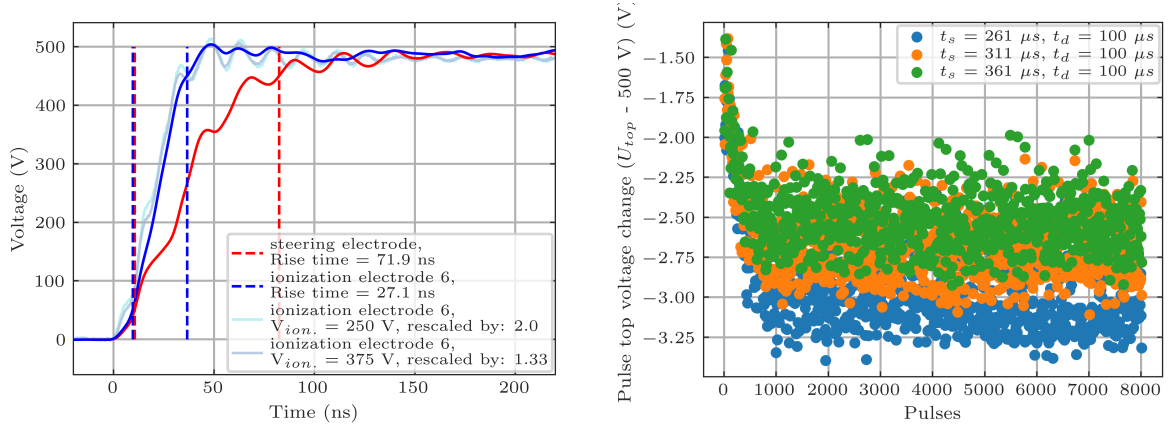
⁴ All high-voltage measurements were conducted using a Lecroy HP120 passive HV probe



(a) Voltage hysteresis. Reaction of the high voltage box output when changing the voltage with and without an additional resistor R_{PS} from 300 to 360 V. This is a (maximally expected) typical step in scans with the voltage (ionization field) as an iterator, cf. fig. 3.2(b).

(b) Settling time for voltage changes when switching from 0 V. The typical voltage scan direction is increasing. Decreasing the voltage leads to longer settling times and additional spare cycles have to be added to exclude false voltages when resetting the voltage to 0.

Figure 2.10: Voltage hysteresis and settling time curves.



(a) Switching to high voltage on ionization and steering electrodes (6) and (9). The 10 to 90% rise time is marked with dashed lines and was calculated. Electrode (8) behaves identical to (6). A comparison to switching other voltages on the electrode (6) is shown. Other voltages rise qualitatively similar to switching 500 V, but relative size of oscillations increases a little bit. A reason could be a change in impedance of the complex circuit. The falling edges of the HV pulse has similar properties.

(b) Stability of HV on (6) over 8000 pulses when switching to 500 V. Each data point is a mean over 10 tops of HV pulses, each of duration $t_d = 100 \mu s$. Varying the separation time between pulses, given by $t_s - t_d$, changes the recharging time of the 100 μF capacitor between pulses and increases the total voltage. A steady state is reached after approximately 800 pulses. The here visible noise of the measurements is probably mostly caused by the coarse sampling of the data acquisition (Oscilloscope: LeCroy WavePro 404 HD).

Figure 2.11: HV switching performance.

- The ionization voltage shows a 10 to 90 % rise time of 27 ns with oscillations of about 10 V at a frequency of about 60 MHz.
- The steering voltage shows a 10 to 90 % rise time of 72 ns with oscillations of about 20 V at a frequency of about 40 MHz.

The difference between the types of electrodes may be due to different electrode capacitances or small differences in wiring and cable length. Due to the fast time scales and the larger distance of the steering to the electrodes this does not affect the ionization process. Significant limits to the quality of high voltage switching are given by (a) the required cable length in our system and (b) the cables used. Even better switching quality could be achieved if the impedances of the commercial parts (*SHV* cables, switches, electrodes) were perfectly matched a priori by the manufacturer.

2.3.2.2 MCP - Working principle and characterization

The science chamber is equipped with a Micro-Channel Plate (**MCP**) detector, which enables the detection of ions that are created in the atomic cloud and guided to the **MCP** with ion-optics (cf. sec. 2.3.2.2)). The Micro-Channel Plate (**MCP**) is a high-gain electron multiplier used for in-vacuum detection of charged particles and electromagnetic radiation, including electrons, ions, ultraviolet rays, X-rays, and gamma rays. It operates as a two-dimensional sensor and is widely used in time-of-flight mass spectrometry, semiconductor inspection, and surface analysis [43].

Working principle. When a voltage V_D is applied between the input and output of an **MCP**, a potential gradient is established along the length of the microchannels. An incident electron entering a channel collides with the inner wall, triggering the emission of secondary electrons. These secondary electrons are accelerated by the potential gradient and continuously strike the channel walls while generating additional secondary electrons in a cascading manner. This process leads to an exponential multiplication of electrons, ultimately resulting in a highly amplified signal at the output. This is illustrated in fig. 2.12. On top of that, the capillary channels of the **MCP** are built-in at an bias angle with respect to the normal of the plate. The bias angles are optimized for maximal detection efficiency and additionally suppress self-amplification of forward and backward propagating signals. In the YQO experiment the **MCP** model F4655-13 from Hamamatsu Photonics K.K. is used. It features a two-stage **MCP**-system with 4 μm channel diameter, a bias angle of 12° , and an effective area of 165 mm^2 [43].

An important quantity for our MCP is the gain, that refers to the amplification of the initial ion signal. The measured gain characteristics of the two stage **MCP** are shown in figure 2.13(a). The x-axis represents the applied

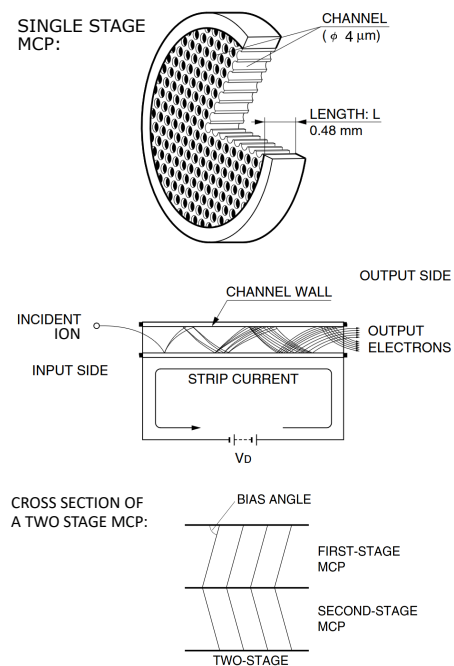


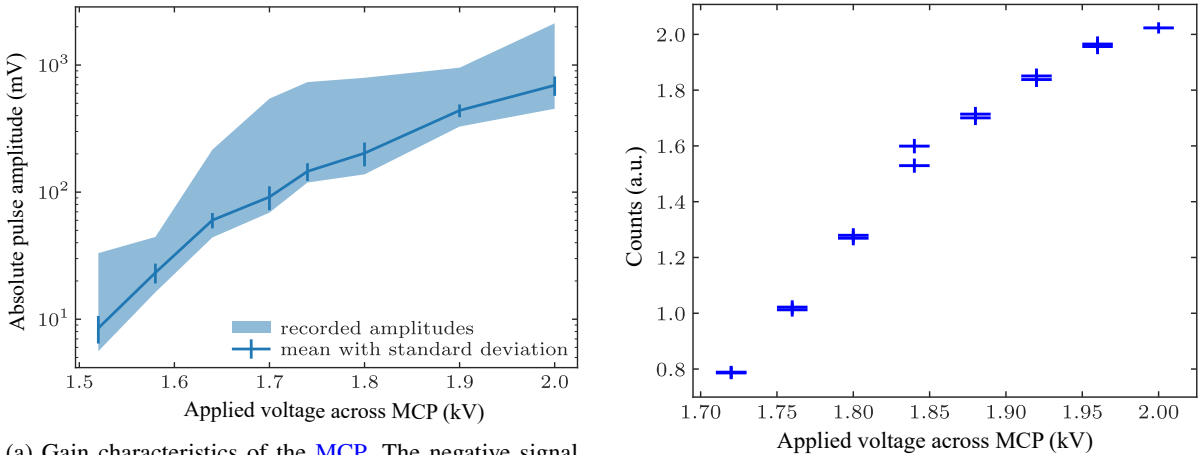
Figure 2.12: Structure and operating principle of a **MCP**. At the top, the effective area with a multitude of microchannels of a single stage **MCP** is shown. Below, the amplification of electrons in a single channel is visualized. At the bottom, a section through a two-stage **MCP** is shown. Adapted from [42].

voltage ranging from approximately 1.5 to 2 kV, with 2 kV rated as the maximum supply voltage. The y-axis represents pulse amplitude in mV, which corresponds to the **MCP** gain. The shaded area represents the range of recorded amplitudes, and a mean amplitude curve is shown. The measurement is based on 1000 pulses per **MCP** supply voltage. The plot indicates that as the applied voltage increases, the pulse amplitude also increases with an exponential saturation at higher voltages.

The gain behavior observed in the plot agrees with the theoretical description of **MCP** gain characteristics in [42]. The single **MCP** gain g follows an exponential relationship with the applied voltage, given by

$$g = \exp(G \cdot \alpha) \quad \text{with} \quad \alpha = L/d \quad (2.1)$$

where G is the gain factor, dependent on the secondary emission characteristics of the channel walls determined by characteristics of the channel wall material and the electric field intensity inside the channel (given by the applied voltage), and α is the length-to-diameter ratio of the micro channels. The gain increase with voltage is expected due to the increased acceleration along the **MCP** channels and the enhanced emission of secondary electrons. The gain initially shows an exponential (linear when plotted with the logarithmic scale) trend for low **MCP** supply voltages. For higher **MCP** supply voltages, the gain begins to saturate due to space charge effects caused by electron cloud interactions that reduce the efficiency of secondary electron multiplication.



(a) Gain characteristics of the **MCP**. The negative signal pulses are measured directly at the **MCP** output. Each data point is a mean of 1000 pulses, that spread in the blue shaded area.

(b) Voltage dependence of detection efficiency. In two independent measurements the countrate was measured directly at the **MCP** output.

Figure 2.13: **MCP** gain and detection efficiency characteristics.

Additionally, the **MCP** supply voltage does not only effect the signal amplification (the gain), but also the signal sensitivity (the detection efficiency). A measurement of this effect was observed by measuring the number of detected ions at different voltages, cf. fig 2.13(b). This effect might have multiple reasons. Firstly, a higher negative voltage on the **MCP** active area causes ions to steer more effectively towards the detector. Secondly, a higher negative voltage causes an additional acceleration of ions, leading to a higher number of primary electrons. Thirdly, the final acceleration might change the angle of incidence of ions. During the course of this thesis it turned out that the detection efficiency of the **MCP** is very sensitive to the incidence angle, with relative detection efficiency of 100 % if the ions arrive at the bias

angle, and dropping to 50 % at normal incidence. However, the MCP holder was designed and mounted without the knowledge of the relevance of this aspect. Fourthly, the probability of primary electrons causing an electron avalanche effect, and thus a detectable signal, increases. For a maximum detection efficiency the maximum MCP supply voltage was chosen for all further experiments.

To summarize, the detection efficiency for ions of the fully assembled isolated MCP is given by the following factors:

- The MCP supply voltage. Demonstrated in figure 2.13(b).
- The energy (velocity) of incoming ions - given by the MCP supply voltage and the ionization voltage.
- The incident angle of ions relative to the MCP bias angle.
- The position on the MCP. This is connected to the incident angle and the energy of ions. Additionally, a slightly dark spot is visible in figure 2.16.

A two stage MCP has the advantage that in pulse counting mode incident weak signals (e.g. single ions) are converted into a pulses with a good pulse height resolution (*PHR*). The *PHR* specifies the dispersion of a pulse height distribution and can be defined as the ratio of the *FWHM* to the mean peak pulse amplitude $|A|$ of the pulse height distribution. The maximum pulse amplitudes are reached at the highest applied MCP supply voltage at 2 kV with an amplitude $|A| = 690$ mV and *FWHM* = 280 mV resulting in a *PHR* = 0.41. By applying a threshold to the MCP output pulses, a binary signal can be created. This last discretization step is performed by a streaming time-to-digital converter⁵.

With an amplifier the negative signal pulses of the MCP are inverted as the used *Time Tagger* requires positive input voltages between 0 to 3 V (recommended), more precisely, the damage threshold input is -0.3 to 5 V. Important to note is, that occasionally MCP pulses with amplitudes below -3 V were observed. It is unclear what mechanism causes these high amplitudes be-

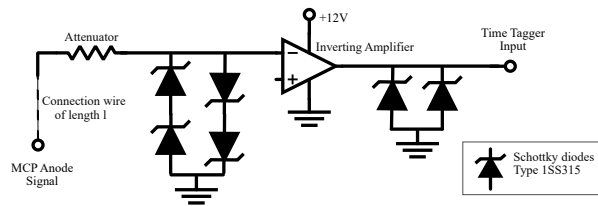


Figure 2.14: Signal processing circuit between MCP anode output and time-to-digital converter (*Time Tagger*) input.

sides the typical statistical fluctuations of the pulse heights. A protection circuit (cf. fig. 2.14) after the MCP will reduce the maximal pulse height of incoming pulses and also cut potential reflections with an inverted pulse amplitude. This is realized by using Schottky diodes [44] that have a low forward voltage drop and a very fast switching action. The forward voltage of the used Schottky diodes is $V_F = 250$ mV at forward current of $I_F = 2$ mA for DC signals. For the fast MCP signals a reliable clipping was observed at 1.2 V. This threshold is influenced by the current of pulses and the behavior of the diode at fast signals due to the diode capacitance which is specified below 1 pF. To reduce possible signal reflections and broadening, the circuit was built as compact as possible and with SMA components.

An attenuator of -8 dB before the broadband amplifier⁶ is chosen to adapt the output signal to the specified optimal input voltages of the *Time Tagger*. Example signals can be seen in figure 2.20(b).

⁵ The Swabian Instruments' *Time Tagger 20* is used.

⁶ Ranging from 0.02 to 6 GHz the amplifier yields a frequency dependent amplification of about 13 dB. That is suited for our signals with a Pulse-FWHM ≈ 1 ns.

Another important characteristic are the counts of the **MCP** induced by non ion events. One can differentiate between dark counts (experiment turned off - no atoms, no light and no fields) and background counts (experiment turned on, but in a state with no production of Yb ions). The dark counts originate from four main sources [42]: Firstly, spontaneous electric field electron emission from the channel walls due to strong electric fields. Secondly, ionization of residual gases inside the **MCP**, generating free electrons. Thirdly, photoelectron emission by electric field scintillation in the **MCP** support parts. In contrast background counts are caused by 395 nm blue control, 1 070 nm dipole trap or room light.

The background counts can be reduced to an almost negligible fraction, when additionally gating the *Time Tagger* to the time frame of ion arrival in the experimental cycle. The active time of the **MCP** is only 20 to 100 μ s. Next to the blue light induced counts the greatest contribution to the **MCP** signal in a standard experimental cycle is the two photon ionization of Yb - also caused by the strong blue light. This process is characterized in section 3.2.

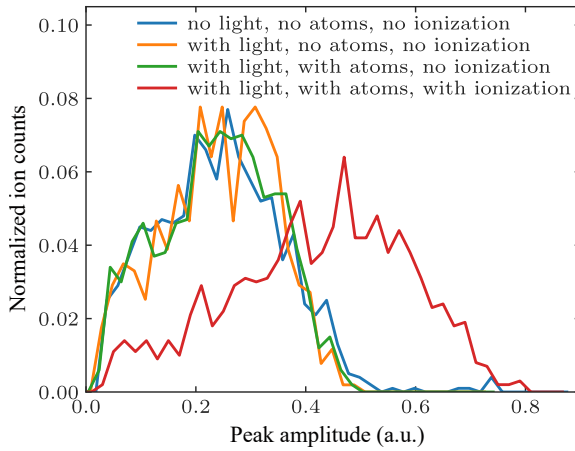


Figure 2.15: Amplitude spectrum under different experimental conditions measured with an oscilloscope. For each condition about 1000 repetitions were performed and the distributions are normalized to an integral of 1.

Additionally, electric ground fluctuations due to fast switching of ionization voltages can interfere with the **MCP** signal. This can be eliminated by gating the **MCP** to be only active if no electric field is switched. Background count fluctuations due to additional neutral atoms present with an active 2D Mot where not observed.

Another interesting effect was observed when measuring the pulse amplitude histogram of dark, background, and ion events, cf. fig. 2.15. The pulse amplitudes of the experimental condition “with light, with atoms, with ionization” represents a superposition of dark, background, and signal ion events. Clearly visible is that the signal ion events are shifted in the the pulse height distribution to higher values.

Ion optics and ionization voltage change. In the sections above, I presented a characterization of the individual parts of the field ionization and ion detection system. In this section the optimization of the interplay between ionization with different electric fields and the detection of ions is described.

Similar to traditional optics that deals with the control of light, ion optics uses electric fields to manipulate the trajectories of ions. The capabilities of the ion optics setup are demonstrated in figure 2.16.

Source	Rate
Dark counts	(0.28 ± 0.07) Hz
5.9 W of 1070 nm dipole trap light on, all other lasers turned off	(0.33 ± 0.07) Hz
All lasers off, room light on	(5.1 ± 0.3) Hz
280 mW of 395 nm control light on, all other lasers turned off	$(1\,382 \pm 5)$ Hz

Table 2.2: **MCP** non-ionic count of different sources. Measured at an **MCP** supply voltage of 1.9 kV. A background due to the room light is visible in the signal, but negligible in comparison to the signal pulse repetition rate of 3 000 repetitions/s. The Control laser is never active during the ion detection period and does not cause background in the signal traces.

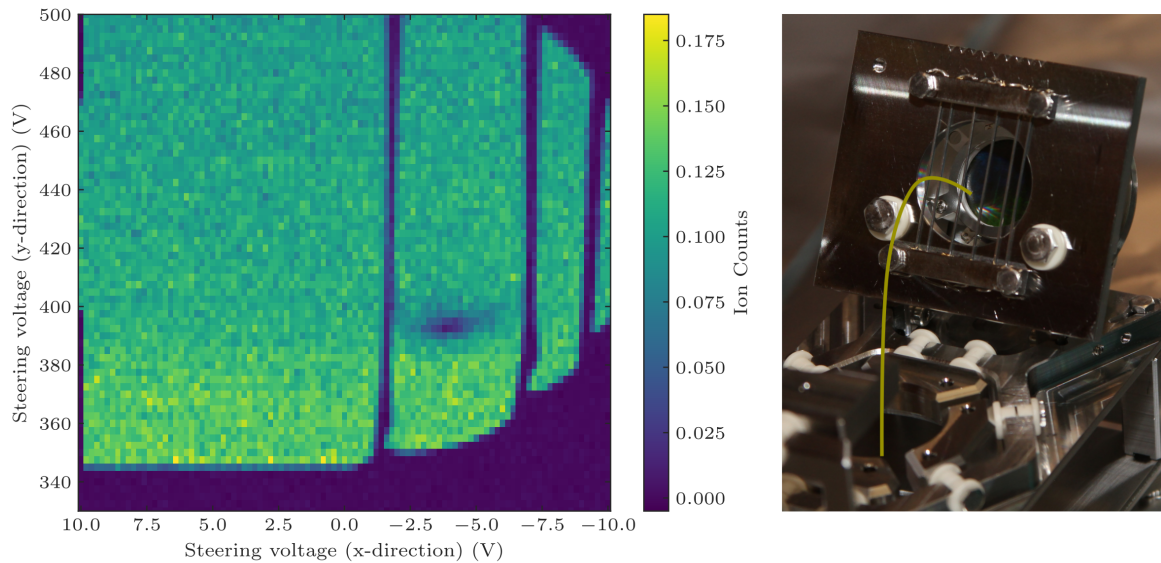


Figure 2.16: Imaging of the **MCP**. The focused ion beam can be deflected in x- and y- direction (referring to the coordinate system in figure 2.7). This can be used to image the shape of the grounded mesh in front of the **MCP** as shown on the left. On the right is a reference image of the full setup taken with a camera. As the deflection field in x-direction is inhomogeneous, a stronger deflection for a negative (attractive) fields is possible. Almost the entire right side of the **MCP** can be scanned. The dark spot at $(-5 \text{ V}, 390 \text{ V})$ is probably an artifact due to permanent damage or particles on the micro channels. Apart from that, the detection efficiency shows little variation along the x-axis. Therefore, no further x-steering is used for the here presented detection of ions.

The field ionization requires ionization with different electric field strengths. The homogeneous E-field is applied in y-direction and accelerates the ions with kinetic energies depending on the applied field strength. To guide the ions to the **MCP** the steering voltage has to be dynamically adapted as a function of ionization voltage. The two criteria for a relation between steering and ionization voltage are: Firstly, finding combinations of optimal parameters to maximize the detection efficiency and secondly, enabling a scanning of the ionization voltage with a constant detection efficiency.

An important tool for the characterization is the two-photon ionization process of the 395 nm control light (details can be found in chapter 3.2). By creating with a constant power of the control laser and the same preparation procedure of the atomic cloud a fixed amount of ions at the position of the atoms, the steering and detection of ions with different ionization fields can be studied decoupled from the applied ionization field. The click rates of the detector are a measure of the relative detection efficiency.

As the detection efficiency is not homogeneous across the active area of the **MCP** (cf. fig. 2.16), I aim to always hit the same position on the **MCP** with the beam of ions. A scan of steering and ionization voltage (cf. fig. 2.17(a)) provides the relative detection efficiencies, similar to a horizontal scan of the **MCP** at x-steering voltage = 0 in figure 2.16. The lower edge of the cone represents the upper **MCP** edge and the upper edge of the cone represents the lower **MCP** edge. In first order these fixed points on the **MCP** are hit with a linear adaption of steering to ionization voltage. This suggests that hitting specific points on the **MCP** can be achieved by a linear relation. However, for low ionization fields, it

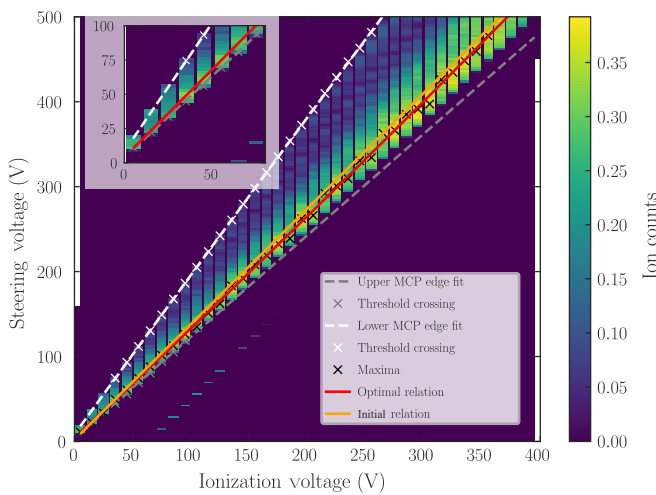
was observed, that hitting the lower MCP is not linear for low ionization fields, while it is for the upper MCP edge.

The best relation was found by using the following fit routine: A linear fit to the lower MCP edge (fit characterized by the white crosses), a quadratic fit to the upper MCP edge by using only the first 10 slices (fit characterized by the gray crosses), fixing the intersection point of lower and upper edge at the minimum ionization voltage, and finally, fitting a quadratic model with a fixed offset to the maxima of each vertical slice of the cone. Fixing the intersection point turned out to be crucial to achieve a relation with constant detection efficiency.

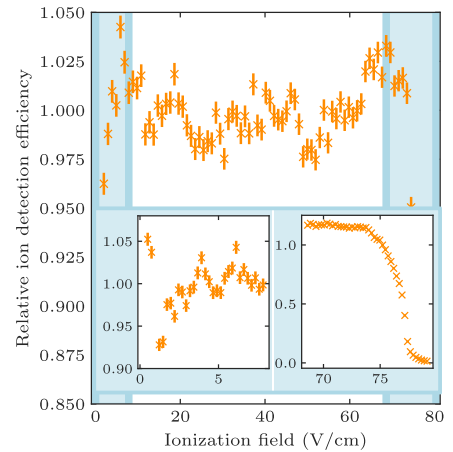
Initially a rough linear relation below was used, with the precise fitting routine, corrections were added. The relation without corrections deviates only slightly from the quadratic relation, but it shows detection efficiency drops of 10 to 20 %. This initial relation used for some threshold scans, and the detection efficiencies were corrected with a measurement of the relative detection efficiency. Nevertheless, with the fit routine presented above, I was able to find an even better relation that can be added as a correction c . The full relation is given by

$$V_{\text{Steering}} = 1.362 \times (V_{\text{Ionization}} + 0.142) - 0.155 + c \quad \text{with} \quad (2.2)$$

$$c = 0.008 \times V_{\text{Ionization}}^2 - 0.089 \times V_{\text{Ionization}} + 0.059 - (0.008 \times (0.135)^2 - 0.089 \times 0.135)$$



(a) 2D Scan of the steering and ionization voltage. A careful fitting was done. The inlet shows the fitting for low voltages. The edges of the MCP and the fits agree very well. The non-zero points below the actual cone are measurement artifacts introduced by a time-efficient scanning scheme.



(b) Relative detection efficiency along the relation 2.2 measured with ions of the TPI-process. The inlets show regions where the detection efficiency displays deviations. For high fields, the steering is limited and for low fields, the delivery time gets extremely long, leading to a high sensitivity.

Figure 2.17: Illustrations of the steering-ionization voltage relation.

As a final characterization step, the relative detection efficiency of ions was measured as a function of ionization field while the steering field was adapted with the new relation. In figure 2.17(b) one can see, that the detection efficiency is for all ionization fields stable to a level of 2.5 %. Due to the limited steering voltage, only ionization fields up to 74 V cm^{-1} can be applied. For low ionization fields the sensitivity of slowly traveling ions to any perturbation is increased and the detection efficiency shows

slightly higher fluctuations. This provides the basis for the threshold measurements in section 3.1.2.

The central limitation of this system is that even small changes in the system, e.g. a simple realignment of the dipole trap that changes the initial position of the atoms and the trajectories, can introduce fluctuations in the detection efficiency of the MCP.

2.3.2.3 Further characterization of the ion detection

To gain a better understanding of technical details, more detailed measurements are presented in this chapter. The detector shows a non-linearity in detection efficiency for high ion counts. The final goal is to assess absolute values for the detection efficiency to the ion detection system.

Multi ion events and correlation of counts. The ions created by ionizing the excitation of one probe-control pulse arrive after the voltage dependent delivery time as a pulse at the MCP. An example of a single ion pulse measured as a time trace can be seen in figure 2.18(a). Each ion event results in a peak with a FWHM of about 2 ns. This FWHM is increased from the FWHM of MCP pulses due to the signal processing circuitry. The trace shown shows multiple ion events. Several aspects I want to mention here: First, multiple ions can arrive at the MCP within the dead time of the time tagger. Second, it is possible to observe events with comparatively low amplitude. All events shown in this time trace are smaller than the typical amplitude of 0.8 V. Especially the first ion (at $t = -2$ ns) shows a very low amplitude. Third, each individual pulse shows delayed peaks due to reflections from electronic components or cable connections, e.g. causing additional peaks at 6 ns after the ion signal peaks. There are also less prominent peaks caused by cable reflections at 2 ns, 15 ns, and 44 ns (the latter corresponds to $2 \times$ the signal delay of the cable used with a length of $l \approx 4$ m).

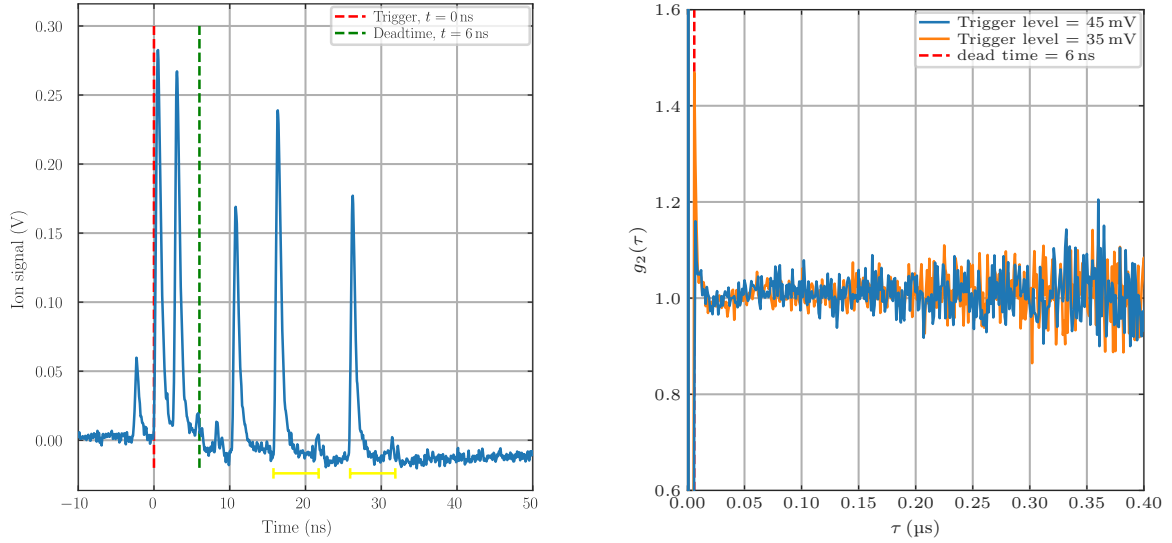
A convenient tool to quantify the difference between signal and noise (e.g. caused by reflections or MCP after pulsed effects) is the analysis of correlations of detected events in form of g_2 functions. $g_2(\tau)$ quantifies the probability of detecting two ions separated by a time delay τ , relative to the probability of detecting them independently and is given for a time signal $y(t)$ by

$$g_{(2)}(\tau) = \frac{\sum_{t_2, t_1 | t_2 - t_1 = \tau} \langle y(t_1) y(t_2) \rangle_{\text{pulses}}}{\sum_{t_2, t_1 | t_2 - t_1 = \tau} \langle y(t_1) \rangle_{\text{pulses}} \langle y(t_2) \rangle_{\text{pulses}}}, \quad (2.3)$$

To acquire good statistics, an additional average over 100000 pulses with each pulse having a time bin resolution of 1 ns is taken. In contrast to the autocorrelation function $C_{yy}(\tau) = \sum_{t_2, t_1 | t_2 - t_1 = \tau} \langle y(t_1) y(t_2) \rangle_{\text{pulses}}$, the g_2 function contains no information on the shape of individual ion pulses. A $g_2(\tau) = 1$ indicates no detection efficiency change at τ due to a click at $\tau = 0$.

As we can see in figure 2.18(b) we have $g_2(\tau) = 0$ for τ smaller than the dead time of the *Time Tagger* (6 ns) and $g_2(\tau) \approx 1$ for τ greater than the dead time. $g_2(\tau \approx 6$ ns) shows a peak. This peak reduces with increasing *Time Tagger* trigger level and is constant for trigger level above 40 mV. This peak can be caused by the signal reflection at 6 ns (cf. fig. 2.18(a)) or have technical causes based on the low trigger threshold (the time tagger has a specified minimum pulse height of 100 mV) [45]. In the sister experiment HQO that has a similar MCP model employed the same correlation at 6 ns was found. Since this correlation is of small size, it will not have a significant influence on the fidelity of the ion detection.

Concluding, the ion detection is not influenced by correlations if the trigger level is chosen above 45 mV. For all measurements of this thesis the trigger level is chosen to be 50 mV. With this trigger level



(a) MCP signal time trace. The signal captures multiple ion events recorded with an oscilloscope behind the MCP protection and amplification circuit. The red line indicates the position of the rising edge of the trigger, the green line the dead time of the Time Tagger that is used in the final setup for data acquisition. The yellow line illustrates signal reflections that are 6 ns delayed to every signal peak.

(b) The normalized second-order coherence (g_2 -function) of ion pulses for two trigger thresholds of the Time Tagger. It was computed with equation 2.3. The g_2 has a 1 ns time resolution. This is limited by the Time Tagger. The Time Tagger deadtime of 6 ns is plotted. For $\tau < 6 \mu\text{s}$, the g_2 -function vanishes. The peak also at 6 ns is minimal for thresholds over 45 mV.

Figure 2.18: Multi-ion events and correlations.

choice, the best balance was found between maximizing the number of detected ions and minimizing false signals.

Absolute detection efficiency measurement. In the previous sections relative detection efficiencies were extracted with the help of the TPI process. The next goal is to determine an absolute detection efficiency. For this, control and probe laser are set to two-photon resonance and excited Rydberg atoms are ionized with the field ionization mechanism (cf. sec. 3.1). The calibrated number of absorbed photons $N_{p,\Delta=0\text{MHz}}$ corresponds to the number of Rydberg excitations. We can also measure the number of registered ions $N_{i,\Delta=0\text{MHz}}$. Background effects, like one-photon absorption of probe light or the TPI by the control light, are known by the photon absorption $N_{p,\Delta \gg 0\text{MHz}}$ and the ion counts $N_{i,\Delta \gg 0\text{MHz}}$ for probe and control far detuned the two-photon transition. Setting $\Delta = 30 \text{ MHz}$ can be assumed as fully off-resonant.

Comparing these numbers yields the Rydberg-excitations-to-detected-ions-ratio EIR:

$$\text{EIR} = \frac{N_{i,\Delta=0\text{MHz}} - N_{i,\Delta=30\text{MHz}}}{N_{p,\Delta=0\text{MHz}} - N_{p,\Delta=30\text{MHz}}} = \text{P}(\text{Successful field ionization}) \times \eta \quad (2.4)$$

This method is illustrated in figure 2.19.

The EIR assess how effectively Rydberg excitations (absorbed photons) are converted into detected ions. It is the product of the probability to ionize a Rydberg state and the pure detection efficiency of the

detector η . For $n = 97$ we can achieve an $EIR = (0.572 \pm 0.002)$. Although the statistical error being small, the total error on this value is dominated by the systematic error on the photon number calibration due to the not precisely known quantum efficiency of the single-photon counters (cf. sec. 2.3.1).

On top of that, the EIR depends strongly on experimental parameters as ionization voltage and laser power (characterized in the previous sections) and the Rydberg state n (characterized in 3.1). For Rydberg states above the ionization threshold $EIR \rightarrow \eta$. From three absolute detection measurements with $n > 50$ we can retrieve $\eta = (0.557 \pm 0.013)$. This result agrees with specifications on the data sheets [43].

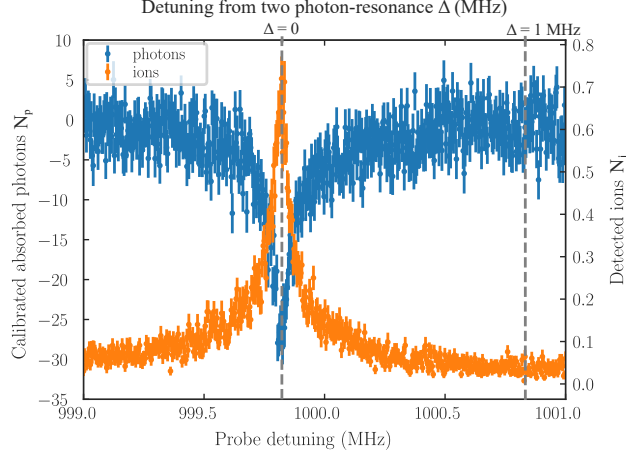


Figure 2.19: Absolute detection efficiency measurement illustration. N_i and N_p are measured at two-photon resonance and $\Delta = 30$ MHz detuned to assess the EIR . In this figure the EIR is the significantly lower than the maximal observed detection efficiency $\eta > 0.5$. The here presented measurement was done on $n = 40$. $n = 40$ is not classically ionizable (cf. fig. 3.3(a)), and can not reach an $EIR = \eta \approx 0.55$.

Detector nonlinearity - Model of a non-paralyzing detector. Our ion detection system is a non-paralyzing detector. This is obvious from figure 2.18(b) where $g_2(\tau < 6 \text{ ns}) = 0$. A nonparalyzable detector system is dead for a fixed time τ_{Dead} after each recorded event and not influenced by events which occur during τ_{Dead} . This results in a nonlinear detection efficiency with increasing ion count rate due to the increased probability to miss events. This is demonstrated in figure 2.20(a).

I did an attempt to compare the nonlinearity of the detector to a simple model [46]. For simplification we assume here a Poisson distribution of events with respect to time. For an observed event counting rate m during a pulse with duration τ_{Pulse} , the fraction of missed events during the dead time is $m \cdot \tau_{\text{Dead}}$. A correction factor of the measured counts m is given by $1 - m \cdot \tau_{\text{Dead}}$. The true count rate n is given by

$$n = \frac{m}{1 - m \cdot \tau_{\text{Dead}}} \Rightarrow N = \frac{M}{1 - M \cdot \frac{\tau_{\text{Dead}}}{\tau_{\text{Pulse}}}} \quad (2.5)$$

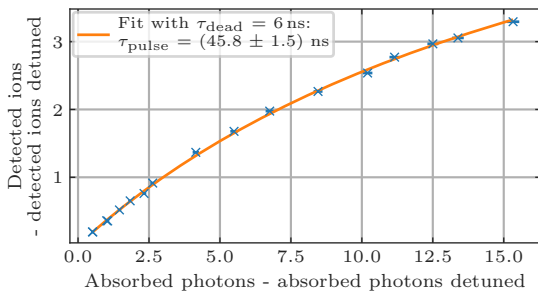
Here N and M are the real and detected events during τ_{Pulse} . Applied to our detector one can set $N = N_{\text{Rydberg excitations}} = N_{p, \Delta=0 \text{ MHz}} - N_{p, \Delta=30 \text{ MHz}}$ and $M = M_{\text{Detected field-ionized excitations}} = N_{i, \Delta=0 \text{ MHz}} - N_{i, \Delta=30 \text{ MHz}}$.

Fitting the inverted form of this model ($M = N / (N \frac{\tau_{\text{Dead}}}{\tau_{\text{Pulse}}} + 1)$) with the known τ_{Dead} to our data results in a (model) pulse duration $\tau_{\text{Pulse}} = (45.8 \pm 1.8) \text{ ns}$. In contrast to the real ion pulse, the model pulse

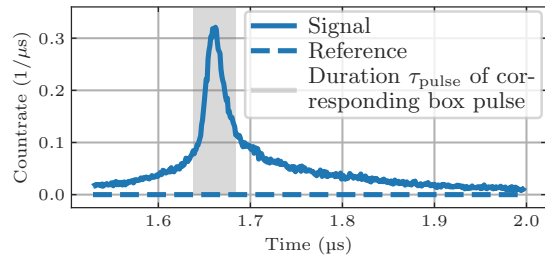
has a box-like shape and a poissonian event distribution. The real ion pulse is shown in figure 2.20(b). Despite the very different pulse shapes, the agreement on pulse duration is visible.

As the concrete nonlinearity does not only depend on the compression of the ion pulse by the applied voltages for ion optics, but also on the contributions of the different ionization mechanisms TPI or RFI⁷, it is not possible to assign a characterization that is always valid for this nonlinearity. In general, we can assume that for count rates $m < 1$, we are not significantly influenced by the nonlinearity.

In general, to correct for higher count rates, the model in eq. 2.5 can be used. This can only be applied if one matches carefully all experimental parameters that might influence the ion pulse time distribution (e.g. high voltage parameters). Additionally, the probabilistic, in time extended character of the field ionization introduces a nontrivial character of the field ionization process (cf. sec. 3.1), also changing the pulse shape.



(a) Dead time nonlinearity of the ion detector. The measurement procedure is illustrated in figure 2.19. The x -axis can be interpreted as created Rydberg excitations and the y -axis as detected field ionized Rydberg atoms.



(b) Mean ion count rate at the MCP. The shape of this pulse depends on the total number of ions and the parameters $V_{\text{Ionization}}$ and V_{Steering} . As a comparison the τ_{pulse} of a corresponding box-shaped poissonian distributed ion pulse with the same nonlinearity is shown in grey.

Figure 2.20: A model for the detector nonlinearity. Both measurements were performed on $n = 57$ with $V_{\text{Ionization}} = 350 \text{ V}$ and $V_{\text{Steering}} = 478.5 \text{ V}$. This combination is not part of the optimal relation 2.2. Therefore the ion detection efficiency is - despite being above the semi-classical ionization threshold - here around 35 % and does not reach the maximum efficiency of $\eta \approx 55 \%$.

This measurement was done at parameters where we can exclude blockade effects in the ensemble and 100s of excitations are possible. The observed nonlinearity can not be associated with Rydberg physics, but is a pure detector effect.

⁷ Additionally the shape of the ion pulse depends for RFI on the Rydberg state.

2.4 Experimental sequence

To conduct the full experiment the three before introduced elements

- preparation of a cold ensemble (cf. sec. 2.1),
- Rydberg excitation (cf. sec. 2.2), and
- detection of Rydberg atoms (cf. sec. 2.3)

are combined to an experimental sequence. The experimental sequence is depicted in figure 2.21 and has two main parts: The atom preparation and two sets of repeated Rydberg excitation and subsequent Rydberg atom detection.

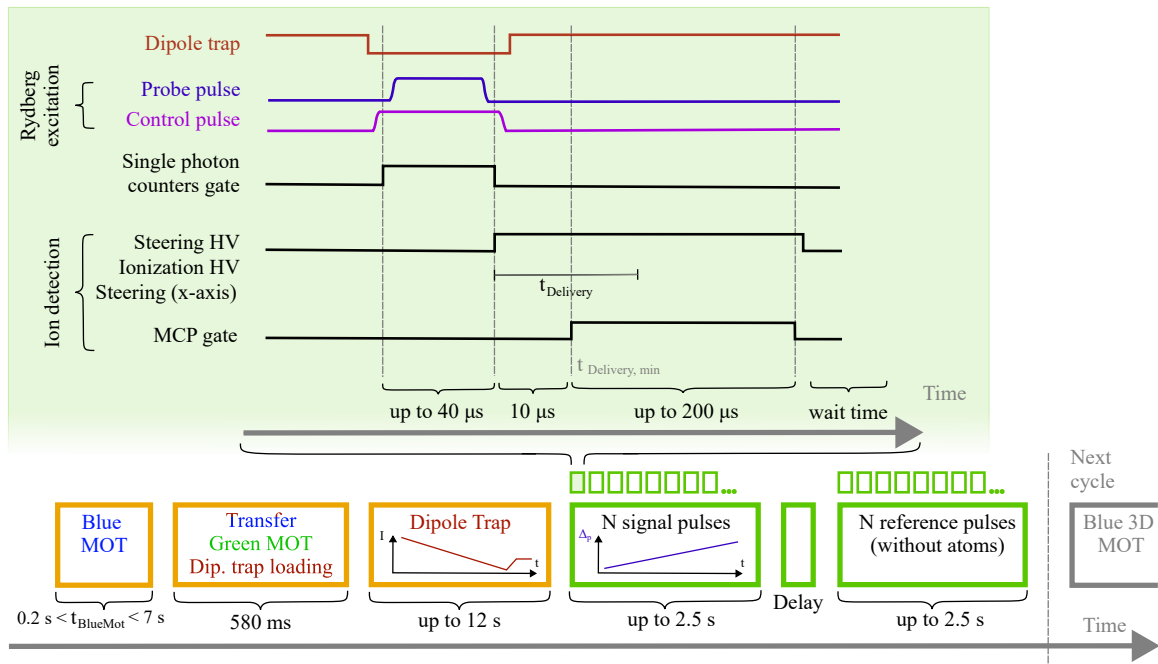


Figure 2.21: The experiment cycle. The bottom row shows the full sequence. The top shows the logic levels of different elements during one repetition: The lasers for trapping and Rydberg excitation, the photon detection, and the Ion detection system consisting of high voltages (HV) for ionization and steering and a microchannel plate detector (MCP).

The *atom preparation phase* is explained in section 2.1 and marked in figure 2.21 with orange boxes. Here I want to stress two details: The total atom number in the final atom cloud can be changed proportional to the parameter $t_{\text{Blue MOT}}$. The final density of atoms is given by the evaporation and compression in the dipole trap. This is determined by the dipole trap Laser intensity I . In the subsequent sections of this thesis, all other parameters are maintained at their optimal levels.

With the prepared atom cloud, two sets of N pulses are applied. These are marked in figure 2.21 with green boxes. The first N pulses are called signal pulses. The major processes occurring during a signal pulse are shown in the red box: The trapping potential is turned off, while Probe and Control pulses are applied to drive the atoms from the $|g\rangle \rightarrow |r\rangle$. Simultaneously, the single photon counters are measuring

the transmission of the single photon Probe beam (cf. sec. 2.3.1). After the excitation the atoms are field ionized and the ions are detected with the MCP after t_{Delivery} . One signal pulse takes 200 to 300 μs (cf. sec. 2.3.2). The second set of N pulses - the reference pulses - are identical to the signal pulses, but during the delay time, the atoms were released. The reference pulses can be used to determine background effects in the Rydberg detection.

To observe and characterize the atomic cloud in atom number, temperature, and cloud size during the experiment, absorption imaging techniques are employed. The shadow of the atom cloud when applying light of a resonant imaging beam is detected by a camera and can be used to determine the optical density and spatial distribution of the atoms [47]. Time-of-flight measurements are used to extract the cloud's temperature by measuring its expansion after release from the trap.

The ability to perform with one atomic cloud up to $N = 8000$ spectroscopy experiments enables the fast acquisition of data and a broad sampling of the probability distribution of the inherently probabilistic Rydberg excitation and detection process. To obtain reliable measurements, each experimental cycle is repeated multiple times, for example 5 times for a Stark map (cf. sec. 3.3.1) and 1000 times for a molecule spectrum (cf. sec. 4). These cycle repetitions average out fluctuations in atom number and temperature.

An important advancement in measurement technique of a spectrum with this setup is the implementation of a scanning measurement mode, where the probe laser frequency is varied along the pulses. Specifically, during N pulses, $M < N$ probe frequency steps are executed. On the one hand, this approach offers two key advantages: Firstly, it significantly reduces measurement time, as the full spectrum can be acquired using a single atomic cloud, unlike traditional methods requiring high sampling for each data point. Secondly, errors related to fluctuations of laboratory conditions that impact atom number and temperature are minimized, as each spectroscopy data point represents an average over the whole measurement time. On the other hand, a disadvantage is introducing systematic errors due to atomic cloud conditions varying over the train of pulses. The N signal pulses are performed over typically 0.1 to 2 s. Atom number and temperature evolve over this time. This is relevant for the spectroscopy of Rydberg molecules and details are discussed in section 4.2.

The methods presented in this chapter offer a solid foundation for versatile use in a variety of applications. It is possible to accomplish this by adapting the parameters of the experimental cycle to align them with the particular requirements of the specific use case. The subsequent chapters will present a demonstration and discussion of the applications of the setup that was the subject of this chapter.

Ytterbium Rydberg atoms in electric fields

All Rydberg atoms respond to static and non-static electric fields with line shifts, state mixing and, for sufficiently large fields, ionization [6]. These effects play a significant role in further conducted experiments due to technical and physical considerations. The field ionization via large electric fields (cf. sec. 3.1) over a wide range of Rydberg states enables the detection of Rydberg excitations. In particular, an effect not predicted (and not foreseen in the experimental design) is the observed far sub-threshold ionization (cf. sec. 3.1.2). That made it possible to explore Rydberg states and molecules below $n = 50$. Photo-ionization through the Rydberg laser light field (cf. sec. 3.2) is a two-faceted phenomenon. On the one hand, it functions as a diagnostic tool, offering a means to characterize the ionization system with a well-controllable source of 'test' ions. On the other hand, it can generate noise in the ion signal and pollutes the atomic cloud with free charges, which has serious consequences for future Rydberg nonlinear quantum optics experiments. Additionally, I present measurements of the AC and DC Stark shifts of the 1S_0 Rydberg series of ^{174}Yb (cf. sec. 3.3). In general, understanding these energy shifts in electric fields allows for better control of atomic transitions in various applications [48]. In particular in the case of ^{174}Yb , results can be used as an independent benchmark of Multi-Channel Quantum Defect Theory (MCQDT) models that describe effects on the wave function by the two valence electrons [26, 27, 49].

3.1 Field ionization of ytterbium Rydberg atoms

The ion detection system (cf. sec. 2.3.2) relies on the field ionization mechanism to convert Rydberg atoms to detectable ions. In a semi-classical approximation of a Rydberg atom, field ionization is only possible above a specific ionization field threshold. This threshold for ionization of Rydberg atoms can be calculated with different stages of complexity [28, 50]. I verified a simple model for field ionization experimentally in the subsequent section 3.1.1. Due to the technical limit on the ionization field, the ionization threshold is only for high Rydberg states below the maximum technically available field. I will name these states *classically ionizable* in the following. In section 3.1.2 I demonstrate that ionization can also be observed far below the threshold and for Rydberg states that should be classically non-ionizable in our setup.

3.1.1 Classical field ionization of ^{174}Yb

The ionization process of a highly excited Rydberg state with the Eigenenergy E_n can be approximated as the interaction of a point-like, independent, classical electron with the electrical potential of the positively charged core, distorted by the applied dc field. The electron is bound to the core with the binding energy

$$E_B = E_n - E_{\text{ionizationlimit}}$$

where $E_{\text{ionizationlimit}} = 1\,512.24$ THz [25].

The core potential, given by

$$V_{\text{Coulomb}} = -\frac{e^2}{4\pi\epsilon_0 r} \quad ,$$

is superposed with the through the dc-electric field \vec{E} arising potential

$$V_E = -e|\vec{E}|y \quad ,$$

where y is the electron-core distance in field direction. The total potential is given by

$$V_{\text{tot}} = V_{\text{Coulomb}} + V_E \quad .$$

The classical field ionization is possible if the binding energy of the Rydberg state E_B is smaller than the local maximum of V_{tot} . This is the case whenever

$$|E| \geq E_B^2 \frac{\pi\epsilon_0}{e^3}$$

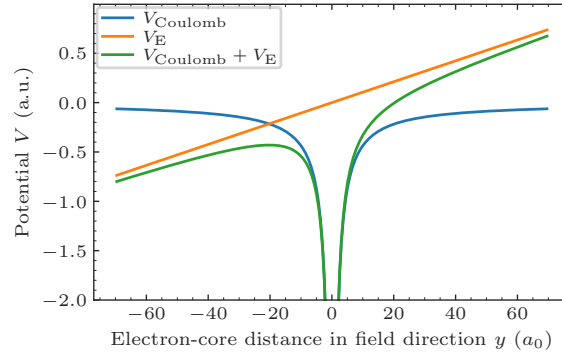
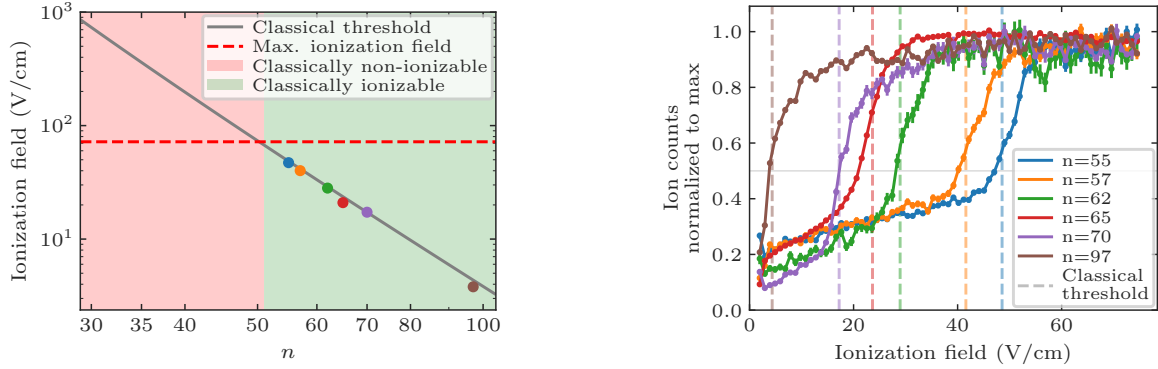


Figure 3.1: The potential of the Rydberg electron V_{tot} is the sum of the potential of the electric field V_E and the coulomb potential V_{Coulomb} of the core.

The classical ionization thresholds, calculated from Rydberg state eigenenergies for different principle quantum numbers $n = \nu + \mu$, are presented in figure 3.2(a). The classical threshold decreases with $\propto \nu^{-4}$ since it scales with the squared binding energy $E_B \propto \nu^{-2}$.

The lowest classically ionizable Rydberg state, $n = 51$, is determined by the technical upper limit of the ionization voltage ($|\vec{E}_{\text{max}}| \approx 74$ V cm $^{-1}$, cf. fig. 2.17(b)). States that exceed this value are regarded

as classically ionizable. The semi-classical description of the ionization mechanism is applicable to these states, as the calculated classical thresholds are in close agreement with the measured field at 50 % ion signal compared to the ion signal at maximum available field, which is far above the threshold. Illustrative measurements are presented in figure 3.2(b). A notable observation is that the ionization of these classically ionizable states with fields below their respective thresholds can also occur with a relatively high rate.



(a) Classically calculated and measured field ionization thresholds for states n . The log-log-visualization represents the power-law scaling v^4 of the threshold linearly. The colored data points correspond to measured 50 percent threshold extracted from the data presented in figure 3.2(b). The red line visualizes the technically maximal available ionization field. States above $n = 50$ have their semi-classically calculated ionization threshold below the ionization field limit and are marked as classically ionizable.

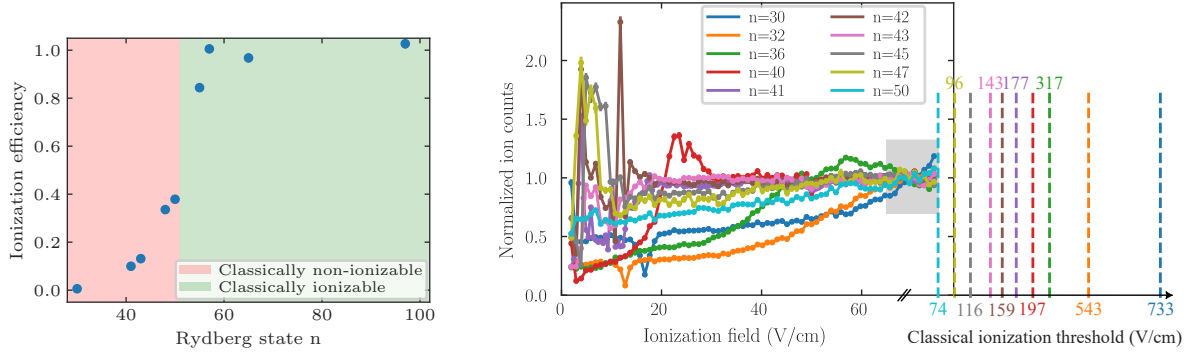
(b) Measured ionization threshold for different Rydberg states. As the field increases, the ionization rate around the ionization threshold suddenly increases. The vertical lines correspond to the calculated classical thresholds. The ion counts are normalized to data points far above the threshold to represent purely threshold-related effects and not general scaling of ion rates due to slightly different Rabi frequencies and atom numbers. The threshold were measured at low density. A horizontal line marks the 50 % threshold.

Figure 3.2: Field ionization above the classical threshold.

For the classically ionizable states that are ionized far above the threshold, it is expected that the ionization probability is 1. Therefore, the Rydberg-excitations-to-detected-ions-ratio (EIR, introduced in sec. 2.3.2.3) should converge to the pure ion detection efficiency, denoted by η . Measurements of the EIR result in an $\eta \approx 55\%$ of the MCP (cf. sec. 2.3.2.3). Subsequent to the extraction of η from ionization far above the threshold, the field ionization efficiency $P(\text{Successful field ionization})$ can be extracted for sub-threshold fields as well, given by $P(\text{Successful field ionization}) = \text{EIR}/\eta$. The ionization efficiency for states below the classical threshold is illustrated in figure 3.3(a) in the subsequent section.

3.1.2 Sub-threshold ionization

It can be observed in our setup, that it is possible to ionize ^{174}Yb Rydberg atoms in our setup far below the semi-classically obtained threshold at a higher rate than expected from related experiments and theory. For example, in reference [28] the ionization of Rydberg atoms in a pulsed electric field is simulated based on classical and quantum calculations for hydrogen like atoms. Their classical ionization threshold is defined as 10 % of the high field ionization rate. For fields far below the threshold, the ionization rate decreases to 0. Experimental results confirm this behavior [29, 30]. I start with presenting the



(a) Measured field ionization efficiency for different Rydberg states n at maximum fields. States with $n > 50$ are classically ionizable in our setup. The ionization efficiency is obtained via the EIR (cf. sec. 2.3.2.3) and by dividing with the detection efficiency η . Statistical errors are very small.

(b) Measured ionization field scans for different states below the classical threshold. Ion counts are normalized to the gray shaded area. All measurements were taken in the linear regime of the MCP (cf. sec. 2.3.2.3). As a reference, the calculated semi-classical thresholds are drawn, similar to the vertical lines in figure 3.2(b). The reference lines are drawn out of scale.

Figure 3.3: Field ionization below the classical threshold. These measurements were done with a sequence similar to the one visualized in figure 2.21, but evaporation and compression were not performed. All measurements were done with the approximately the same density, that is low compared to the molecule scans in the next chapter. For the efficiency measurements the Probe pulse duration was set to $10 \mu\text{s}$ (significantly shorter than the Rydberg atom life time) to minimize a falsification of the EIR through Rydberg population decay. For some of the lower Rydberg states a significantly higher Probe power was used to increase the signal strength and ND-filters were inserted before the single photon counters (cf. fig. 2.6). This was taken into account for the calibration of the absorbed Probe photons.

observation in our experiment:

As demonstrated in figure 3.3(a), an assessment of the total ionization efficiency shows that states below the threshold are less prone to ionization in comparison to states above the threshold of $n = 51$. The ionization efficiency is measured at the technically maximal available fields, ranging from 68.5 and 72 V cm^{-1} . For the non-classically ionizable states with $30 < n < 45$, the ionization efficiency ranges from 0.5 to 40% despite the ionization field being far below the classical ionization threshold. This finding is in clear contradiction to the results presented in the references [28–30].

Furthermore, additional information can be obtained by examining scans of the ionization field for various not-classically ionizable Rydberg states, as illustrated in figure 3.3(b). With regard to the measurement of ionization efficiency (cf. fig. 3.3(a)), the ion counts on the y-axis were normalized to a comparable range to eliminate relative scaling differences between the various thresholds that can be attributed to different Rabi frequencies of the excitation process. The normalized count rate can be understood as the ionization efficiency relative to the efficiency shown in figure 3.3(a). The relative ionization efficiency shows a slightly decreasing trend for some Rydberg states, a constant value for others, and peaks and dips for still others. These irregularly appearing features are ionization-enhancing and prohibiting resonances at specific fields.

In concluding from these observations, the sub-threshold ionization effect is found to be stronger than that observed for single electron species. This phenomenon cannot be explained by the simple semi-classical theory presented in section 3.1.1. The observed resonances imply non-trivial ionization

dynamics.

It has been observed that the resonances are connected to the Dipole trap light. Generally speaking, the Dipole trap is deactivated solely during the Rydberg excitation by the Probe and Control pulse. However, the recapture of the atoms by the Dipole trap occurs in simultaneity with their ionization. When the dipole trap field is additionally deactivated during the full ionization pulse, the sharp resonances disappear. Therefore, under certain resonant conditions - matched by highly shifting the states in the strong electric field - the dipole trap contributes to the ionization process via a photoassisted ionization mechanism. This claim is supported by the observation that the energy difference between the $6sns\ ^1S_0$ Rydberg states matches meta-stable auto-ionizing states in spectra recorded in reference [25]. To be noted, in principle, the Control light can also drive resonant transitions to auto-ionizing states [25]. In addition to causing resonance-like ionization features, the dipole trap light has been shown to modify the overall amplitude of ion rate, thereby contributing substantially to the observed sub-threshold ionization. However, a notable amount of sub-threshold ionization persists when the dipole trap is deactivated during the ionization process.

The pure field sub-threshold ionization can not fully be explained by the following approaches. One approach to explain the sub-threshold ionization could involve quantum-mechanical effects as the tunneling of electrons through the by the applied field reduced potential barrier of the atomic potential $V_E + V_{\text{Coulomb}}$ (cf. fig. 3.1). However, given that the structure of the Rydberg core potential is not fundamentally different for Yb compared to Alkali atoms, this explanation alone is insufficient to support the observations. In addition, the Cascade-effects and Rydberg-facilitation effects, which are contingent on the number of Rydberg excitations, can be disregarded: The ionization efficiency remains constant for different numbers of Rydberg excitations, which can be proved by varying Probe and Control Rabi frequencies. As demonstrated in figure 7.5 of reference [29], experimental findings have indicated that density dependent l -state-changing collisions result in a threshold shift toward higher ionization fields. This assertion stands in direct opposition to the observations that we have made and can be excluded as a possible explanation, too. In general, is the quantification of density-dependent effects below the threshold challenging due to the significant influence of density on the total count rate. On top of that, the ion count rate is convoluted with the ionization-mechanism-dependent ion-pulse shape due to the non-linearity of the detector (cf. sec. 2.3.2.3).

As another option, a potential sub-classical threshold field ionization mechanism could be related to the electronic structure of ^{174}Yb . When the electric field is increased, the Rydberg electron follows a complex Stark map and crosses many avoided crossings. ^{174}Yb is disturbed by avoided crossings at very small field strength (*Pairinteraction*, [27]). Further experimental and theoretical investigation is necessary to better understand this effect. The measurement of a stark map under conditions of high electric fields has the potential to provide insights into these processes.

With regard to the ionization mechanism that has not yet been fully characterized, the sub-threshold field assisted ionization can be used to perform spectroscopy of Rydberg states with $n \leq 50$ utilizing the low-noise ion detection setup. It is essential to ensure that the observed sub-threshold ionization effect does not influence the spectroscopic results of ^{174}Yb . This is given, since the field-enhanced ionization process is separated in time from the excitation process, as the ionization pulse occurs after the excitation process. It is a valid assumption, that the spectroscopy results are not influenced by the ionization dynamics.

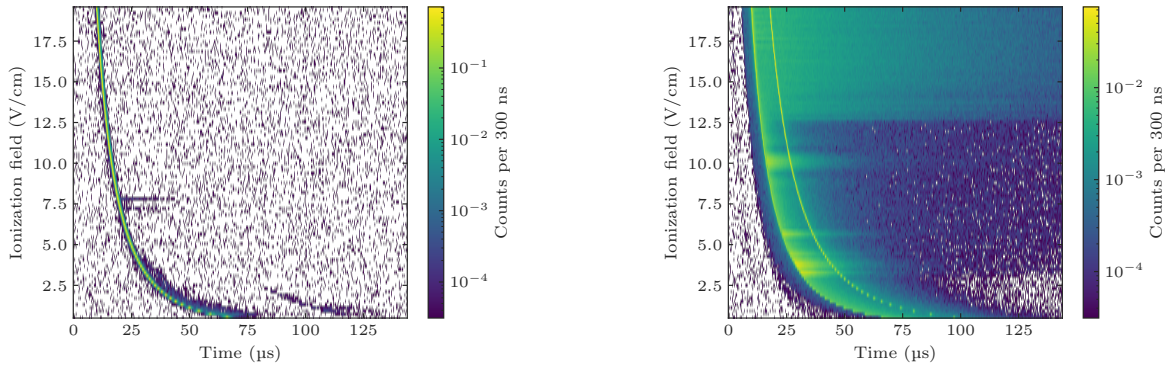
3.1.3 Ionization time dynamics

This tool presented in this section can be used to study the time dynamics of the ionization processes and might be useful for a future characterization and disentangling of these processes. The **MCP** detector is an appropriate instrument for the time-resolved measurement of the arrival of ions. It allows for the measurement of the delivery time from the atomic cloud to the **MCP**. The delivery time is dependent on the acceleration a of ions in a field, which is proportional to the field E_1 and to the inverse mass m^{-1} . Therefore, the delivery time is given by

$$t_D \propto \sqrt{\frac{1}{a}} = \sqrt{\frac{m}{q \cdot E_1}}, \quad (3.1)$$

with q being the charge of the ion. Here, it was assumed that the delivery path is equal for all E_1 and q . Experimentally, for a change of E_1 (or the corresponding voltage of the ionization electrodes), the steering voltage has to be adapted to hit the **MCP** and to maintain an equal detection efficiency. This is achieved by always hitting the same position on the **MCP** by adapting the voltage on the steering electrode (cf. sec. 2.3.2.2). It is possible that the resulting calibration does not correspond to identical trajectories for all E_1 . The ions may exhibit deviations from their ideal trajectories due to factors such as the non-instantaneous ramp-up of the field and the subsequent small field oscillations that occur after the ramp-up, with a timescale of $0.5 \mu\text{s}$. These factors might cause deviations from relation 3.1.

The distribution and arrival time of $^{174}\text{Yb}^+$ ions, which are decoupled from the rydberg atom ionization process, can be measured by guiding ions created by the two-photon ionization (**TPI**, cf. sec. 3.2) process to the **MCP**. In **TPI**, ions can be generated without exciting atoms to Rydberg states. Therefore, the ion detection is purely dependent on detector characteristics. In figure 3.4(a) the arrival time of **TPI**-ions is apparent. The ions arrive in a sharp pulse and at a field-dependent delivery time t_D .



(a) Time trace of the **TPI** process (cf. sec. 3.2). The ionization and the steering field are switched on at $t = -10 \mu\text{s}$. The Control power is high, and Probe is disabled. Only few recorded events are not part of the trace of ion arrival. These can be attributed to noise and artifacts.

(b) Time trace of the Rydberg atom ionization processes for $n = 41$. The atom cloud is prepared at a medium density and Control and Probe have a two-photon detuning of $\delta = 0$. For the chosen Control power, the **TPI** process is negligible in comparison to the Rydberg atom ionization.

Figure 3.4: Time dynamics of ionization processes. Both measurements have similar total mean ion counts.

In contrast, the Rydberg atom ionization process is presented in figure 3.4(b). In this measurement, **TPI** is still present. It is possible to adjust the Control power in such a manner that the probability of

Rydberg atom ionization exceeds that of TPI.

The Rydberg atom ionization process features three main time-dependent effects.

Firstly, the presence of an emphasized line at the same position as the line in the measurement of the TPI process indicates an instant ionization of by the field or might just display already created atoms, e.g. by the Control beam.

Secondly, the distribution of ions is more diffuse in comparison to the TPI process and extends almost over the full recorded time frame. The spread in time is strongest around the resonances and above fields of 12.5 V cm^{-1} . This suggests that the involved ionization processes are not purely instantaneous ionization effects, but rather possess a probabilistic component. The ionization related to this second observation can be attributed to the dipole trap light. The dipole trap light is activated to recapture the atoms directly following the Probe pulse. The activation and deactivation of the dipole trap light can enable the long tail of the ionization signal. The dipole trap light can drive transitions to autoionizing states above the ionization threshold of the $6sns \ ^1S_0$ -series. The energies of these states are measured in reference [25]. The decay of the ion signal over time can probably be attributed to the finite lifetime of Rydberg excitations in the cloud.

Thirdly, a sharp second line is visible for arrival times that correspond to $\sqrt{2}t_D$. According to equation 3.1, this line can be attributed to particles with twice the mass, specifically $^{174}\text{Yb}^{2+}$ ions. This is illustrated with more detail in figure 3.5. In accordance with the results outlined in reference [29], I observe that the formation of $^{174}\text{Yb}^{2+}$ is strongly density dependent. For the ionization of molecular states $^{174}\text{Yb}^{2+}$ formation is much more likely due to a local increase of density as always at least a minimum of two atoms are present to facilitate molecule formation. As described in reference [29], for lower Rydberg states I observe a strong increase in the fraction of $^{174}\text{Yb}^{2+}$ formed due to an energetically more stable chemi-ionization process. The formation of $^{174}\text{Yb}^{2+}$ is another ionization effect that might contribute to the full sub-threshold field-assisted ionization process presented in section 3.1.2.

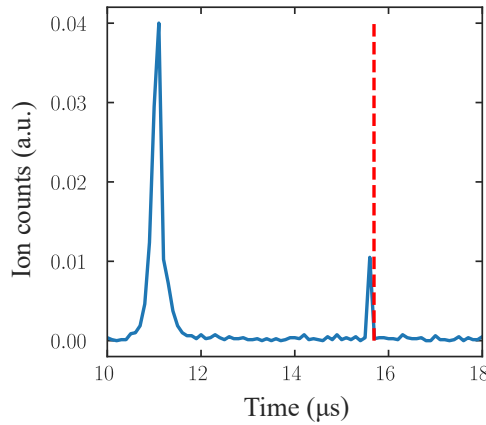


Figure 3.5: Demonstration of the usage of the ion detection system as a mass spectrometer. The time trace of the ion detection signal shows two peaks. The first peak can be attributed to the arriving $^{174}\text{Yb}^+$ ions. The red line depicts the arrival time $\sqrt{2}$ after the first pulse. It agrees well to the second peak, that can be attributed to $^{174}\text{Yb}^{2+}$ molecules. The small deviation between the $\sqrt{2}$ -line and the second pulse might be caused by the finite rise time of the electrodes (cf. fig. 2.11(a)) or electronic delays.

In summary, the time-dynamics of the ionization process are complex. A multitude of factors contribute to the process of ionization. A future, quantitative investigation could focus on separating the different

processes better and contribute to a better understanding of all involved ionization processes.

3.2 Two-photon ionization of ytterbium

The possibility exists to decouple one ionization mechanism, the two-photon ionization (TPI) process, from the field-assisted ionization of ^{174}Yb Rydberg atoms. This chapter highlights characteristics of the observed ionization behavior that allow a clear association with a two-photon Control beam-related process.

Two-photon ionization (TPI) is a nonlinear process in which an atom absorbs two photons simultaneously, resulting in the ejection of an electron. In general, fundamental theoretic foundations of TPI are understood [51, 52]. Nevertheless, quantitative calculations are challenging because the probability of this process occurring is strongly dependent on the detunings to other intermediate states and the strengths and frequencies of these transitions. This is particularly challenging in the case of the two-valence electron species Yb with its rich level scheme.

Brief introduction to TPI: The two-photon ionization process is described by the general reaction:



Due to energy conservation, the sum of the two photon energies must be equal or exceed the ionization potential V_i :

$$2\hbar\omega = V_i + E_a, \quad (3.3)$$

where the TPI excess energy $E_a \geq 0$ is the kinetic energy of the ejected electron. The transition may occur through intermediate virtual and real states, provided that the photon energy fulfills the condition $E_k - E_i \approx \hbar\omega$, with E_k the energy of the intermediate state $|\psi_k\rangle$ and E_i the energy of the initial state $|\psi_i\rangle$. Applying *Fermi's Golden Rule*, the transition probability $W_{i \rightarrow f}$ per unit time yields:

$$W_{i \rightarrow f} \propto \left| \sum_k \frac{\langle \psi_f | H_{\text{int}} | \psi_k \rangle \langle \psi_k | H_{\text{int}} | \psi_i \rangle}{E_k - E_i - \hbar\omega} \right|^2 \rho(E), \quad (3.4)$$

where ψ_i and ψ_f are the initial and final wavefunctions of the electron, $\rho(E)$ is the density of final states, and H_{int} the atom-field interaction Hamiltonian. As we can see from equation 3.4, in contrast to single-photon ionization, which is a first-order process in perturbation theory, TPI is a second-order process [51, 52]. Since H_{int} is proportional to the electric field $|\vec{E}|$, TPI depends according to equation 3.4 quadratically on the intensity of the incident radiation:

$$W_{2\gamma} \propto I^2 \quad (3.5)$$

Another way of characterizing the likelihood of an ionization event is given by the cross section σ . For the two-photon ionization TPI process, σ provides a measure of the effective area of the scattering process. In contrast to the quadratic scaling of the ionization rate, the cross section scales linearly: $\sigma \propto I$.

The in the experiment measurable quantity is the TPI-rate R . R is related to σ via

$$R = \sigma \cdot F \quad \text{with the photon flux density} \quad F = I \frac{\lambda}{hc}. \quad (3.6)$$

In the experiment, R determines the number of present ions, that can be detected with the [MCP](#).

TPI in ^{174}Yb : ^{174}Yb is an alkaline-earth-like element with a complex electronic structure. The two-photon ionization energy of the $6s^2\ ^1S_0$ -state is $V_I = 6.2541\text{ eV}$. This is equivalent to a wavelength $\lambda_{\text{ionization}} = 396.49\text{ nm}$ [25]. In the experiment, the Control laser is operated at a range of 10 to 400 mW at approximately 395 nm, with the energy of two Control photons slightly exceeding the ionization threshold.

The following line of arguments demonstrates that the observed ionization process can be fully connected to [TPI](#):

1. No ions are detected if field ionizing without a Probe and Control are turned off during a sequence. This implicates, that there are no 'residual' ions and it is not a pure field related effect.
2. Ions are created during Probe-Control pulse. This has been measured by applying a weak electric field for a duration of some μs before the ionization through the strong ionization and steering field. The weak field repels the ions and changes their position. According to the strength of the weak field the ion arrival time changes - meaning, that the process occurs during the light pulse - before the field ionization. Therefore, it is possible to detect the two ionization processes (Rydberg field ionization and [TPI](#)) within the same sequence, albeit separated in time.
3. No ions are detected if the atoms are exposed to any other light fields when the control field is turned off. Consequently, the presence of ions cannot be attributed to [MOT](#), Probe or dipole trap light. In principle, it would be feasible to mix photons from disparate sources to facilitate a multi-photon ionization process. For the [TPI](#) process, Control can be off resonant to a transition to a Rydberg state.
4. Ions are detected if Probe is blocked and Control is activated. We can conclude, that the process is purely related to Control light and not related to the typical excitation scheme (cf. fig. 2.5).

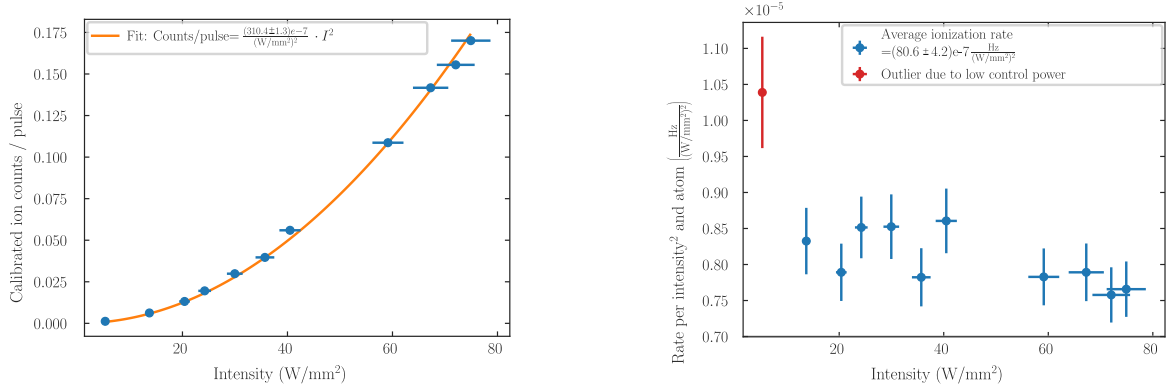
In addition to the qualitative evidence for the [TPI](#) process, two core measurements identify and characterize important [TPI](#)-typical characteristics. Firstly, the quadratic dependence on control power and secondly, the dependence on the control wavelength.

Dependence of 2-photon ionization on power

Relation 3.5 postulates a quadratic scaling of the ionization rate with the applied light intensity. As illustrated in figure 3.6(a), the power dependence of the [TPI](#) process is measured. A quadratic fit shows good agreement to the data. Since the Control beam is not power stabilized, the power exhibits short and long-term fluctuations. Short-term fluctuations are represented in the statistical error of the count rate over the repetitions of the measurement. Conversely, long-term fluctuations between the measurement and the control beam power calibration can be represented in the data as a 5 % error attributed to the intensity data.

As illustrated in chapter 2, the measurements are done in a pulsed fashion. Dividing the mean of all pulses by the pulse duration provides the total ionization rate R_{total} of the atomic ensemble is given by

$$R_{\text{total}} = \alpha_{\text{total}} \cdot I^2 \quad (3.7)$$



(a) Intensity dependence. The measurement was performed with about $N = (467\,000 \pm 85\,000)$ atoms at a temperature of $T = (17.2 \pm 4.4)$ μK with Control pulse duration $\tau = 11.5$ μs . The intensity refers to the peak intensity of the Gaussian control beam. The ion counts were calibrated with the detection efficiency η of the ion detection system. The measurement was performed with the Control frequency that is usually used to drive the transition to $n = 41$.

(b) Calculation of single atom ionization rates per intensity. This plot shows the same data as figure 3.6(a), but represented in a different way. Expected is that this rate is constant for all intensities. Details on calculation and errors can be found in the text. The data point at low intensity can be considered as an outlier. The mean of all blue colored data points gives the average ionization rate per intensity² and atom. It has a value of $(80.6 \pm 4.2) \times 10^{-7} \text{ Hz}/(\text{W}/\text{mm}^2)^2$.

Figure 3.6: Verification of the quadratic intensity dependence of the two-photon process.

with α_{total} the ionization rate in $\text{s}(\text{W}/\text{mm}^2)^2$ of the setup with the measurement settings. α_{total} is specific to the settings and the current sequence of this measurement. It determines the atom cloud shape and the Control beam parameters. More general, α_{total} is the ionization rate of the inhomogeneous atom cloud in the inhomogeneous Control light field.

A more general approach involves calculating the single atom ionization rate per intensity, or the cross section σ of TPI. This is presented in the next paragraph. σ can be used to compare the TPI process to other sequences in our experiment, to other experiments, and to other species.

Ionization rate per atom and intensity: For a single atom in a non-resonant light field with intensity I , the ionization rate R is given similar to the relation 3.7 by $R = a \cdot I^2$. Here, a is the ionization rate per intensity and per atom. This relation 3.7 modifies to

$$R_{\text{total}} = a \cdot \int I^2(r, z) n(r, z) dV \quad (3.8)$$

where $n(r, z)$ is the atomic density and $I(r, z)$ the Control intensity distribution. The atom number N in the volume dV is given by $N = n dV$. The atomic density $n(r, z)$ of the cigar-shaped atomic cloud can be approximated with a Gaussian distribution along the z -axis and a radial Gaussian distribution in the x - y plane and is given by:

$$n(r, z) = \frac{N}{(2\pi)^{3/2} \sigma_z \sigma_{xy}^2} \exp\left(-\frac{z^2}{2\sigma_z^2}\right) \exp\left(-\frac{r^2}{2\sigma_{xy}^2}\right) \quad (3.9)$$

where N is the total number of atoms, $\sigma_z \approx 58 \mu\text{m}$ is the Gaussian standard deviation along the z -axis, $\sigma_{xy} \approx 9.4 \mu\text{m}$ is the Gaussian standard deviation in the radial direction (x - y plane), and $r = \sqrt{x^2 + y^2}$ is the radial distance from the center of the cloud in the x - y plane. The estimation of the extend of the atomic cloud is obtained by simulation of the trapping frequencies of the dipole trap. The prefactor $\frac{N}{(2\pi)^{3/2} \sigma_z \sigma_{xy}^2}$ ensures normalization so that the integral of $n(r, z)$ over all space yields the total number of atoms N . Similar to the atom density $n(r, z)$ distribution, a spatial distribution of the Control light field $I(r, z)$ can be computed with the parameters Power, beam waist ω_0 , and wavelength.

With relation 3.8 the ionization rate a is calculated for each measurement of R_{total} in figure 3.6(a) and plotted in figure 3.6. The first data point is an outlier and thus excluded from the analysis. This can be attributed to the bad statistics at very low control power or systematic errors due to a bad Control power calibration. Finally, the single atom ionization rate a can be computed to

$$a = (8.06 \pm 0.42) 10^{-6} \text{ s} / (\text{W}/\text{mm}^2)^2 \quad (3.10)$$

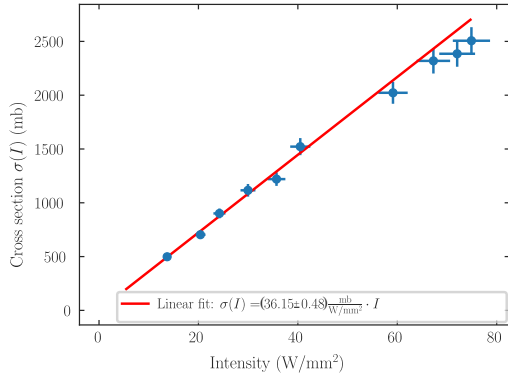
The errors presented in figure 3.6 are based on standard errors of the mean of 70 individual measurements and propagated errors of the intensity fluctuations. The error on a is also estimated as a standard error of the mean of the 10 repetitions. In addition to these statistical errors, significant systematic errors might be relevant. One major uncertainty is the precise modeling of the intensity and density distribution. The estimation for the beam waist $\omega_0 = 45 \mu\text{m}$ is based on calculations of the optical system; however, it cannot be measured directly. An assumed relative error $\Delta\omega_0/\omega_0 = 0.1$ propagates to a relative error $\Delta a_{\omega_0}/a = 0.14$. The atom number measurement via absorption imaging can be attributed with a relative systematic error of $\Delta N/N = \Delta a_N/a = 0.1$. Due to the small atom cloud compared to the control beam, errors on the cloud size have a weak influence on a . Furthermore, uncertainties associated with the ion detection efficiency contribute only marginally to the overall uncertainty. When the two major contributions listed above are considered, a realistic systematic error of at least 20 % must be assumed.

Cross section σ of the TPI-process: As a next step of this analysis, the cross section σ can be calculated with eq. 3.6 from the measured data. This is plotted in figure 3.7(a). The fit reflects the expected linear relation.

The measured cross section σ can be compared to literature values for TPI in similar atomic species. Since no reference value of TPI for ^{174}Yb was found, only a comparison with calculations from three papers (from the 1960ies) is presented in (3.7(b)). The comparison to literature values demonstrates, that the measured effect is in a same order of magnitude. Deviations can be attributed to a not good comparability of the different atomic species that differ in level structure and energy scales. Further investigation and estimation of systematic error was not performed.

Dependence of 2-photon ionization on wavelength

For a TPI process, the ionization rate is expected to depend strongly on the light frequency if the light is almost resonant to the ionization threshold. Around the resonant TPI process a Fano-like resonance curve appears [52–54]. Therefore, the TPI process caused by Control light in ^{174}Yb is expected to have a threshold for $\lambda_c > 396.49 \text{ nm} = 756.11 \text{ THz}$. A measurement for different control wavelength is shown in figure 3.8. The measured threshold corresponds to the predicted theoretical values. The TPI process vanishes for smaller wavelengths, with the exception of a minor resonance at 754.8 nm. This is


 (a) Linear fit of the cross section σ .

Species	Reference	$\sigma^{\text{two-photon}}$ (mb/(W/mm ²))
Hydrogen	[53]	100
Cesium	[52]	0.6
Cesium	[54]	0.2
Ytterbium	measured	36.15 ± 0.48

(b) Literature values for TPI cross sections in similar species and the measured value of ^{174}Yb . The order of magnitude of the literature values was estimated by extracting σ at a wavelength that is 1% blue detuned to the first, major single-photon resonance, similar to 395 nm to 399 nm. The literature values for hydrogen and cesium show a large discrepancy.

 Figure 3.7: Calculation of the TPI cross section σ and comparison to literature.

attributed to the energy of two control photons diminishing below the requisite ionization energy.

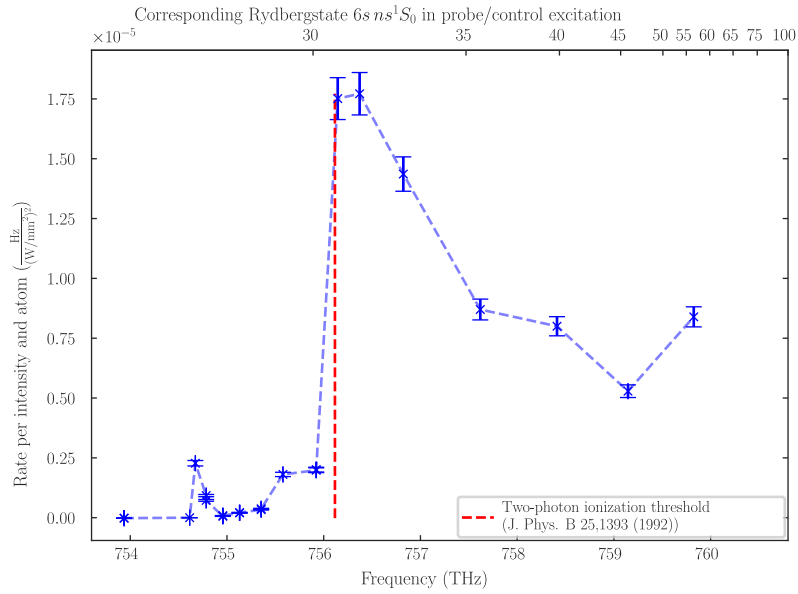


Figure 3.8: Energy dependence of two-photon ionization process. The Control laser is scanned over a large frequency range and adjusted to the same power for each frequency point. The rate per intensity and atom a was obtained by using the data point at $n = 41$ as a calibration with reference to the measurement presented in figure 3.6(b).

Consequences of the TPI process for further experiments

After the TPI the free electrons will leave the atomic cloud in a few ns. The residual Yb^+ ionic cores are quasi stationary and will move only below $1 \mu\text{m} \mu\text{s}^{-1}$ due to the Control frequency dependent residual

energy of the ionization process. These free, quasi-stationary charges affect the high Rydberg states by introducing additional Stark shifts. This might lead to regions in the cloud that appear after the occurrence of a TPI-process off-resonant and can not be excited to Rydberg states. Free charges might also play a role in the ionization dynamics of ytterbium. For high densities, strong local fields might lead to ionization of surrounding excited Rydberg atoms.

3.3 AC and DC Stark shifts of ytterbium

It is particularly challenging to make precise predictions of the Rydberg state polarizabilities for atomic species with complex multilevel structures, such as ^{174}Yb , using only ab initio calculations [55]. For example, as I will show in the following section, the calculation of the polarizability $\alpha^{(0)}(n)$ requires knowledge of dipole matrix elements between target states and numerous other highly excited states (cf. eq. 3.13).

With the ion detection system (cf. sec. 2.3.2) we are able to perform spectroscopy with a high SNR. Therefore, the ion detection system facilitates a quick and precise determination of the positions of atomic lines. In combination with a high degree of control over static electric potentials with the electric field control and the ability to adjust the power of all laser beams, our setup is ideal to measure the static dipole polarizability (cf. sec. 3.3.1) and light shifts (cf. sec. 3.3.2).

3.3.1 Static dipole polarizability

In the presence of an external static electric field, atoms experience a shift of atomic energy levels due to the Stark effect. The Stark effect arises from the interaction between the atomic dipole moment and the external electric field. The energy shift is determined by the perturbative atom-field interaction Hamiltonian:

$$H_{AF} = -\mathbf{d} \cdot \mathbf{E}, \quad (3.11)$$

where \mathbf{d} is the atomic dipole operator, and \mathbf{E} is the applied static electric field. The energy level shift of a particular atomic state $|\alpha\rangle$ can be computed using second-order perturbation theory [48]:

$$\Delta E_\alpha = \langle \alpha | H_{AF} | \alpha \rangle + \sum_j \frac{|\langle \alpha | H_{AF} | \beta_j \rangle|^2}{E_\alpha - E_{\beta_j}}, \quad (3.12)$$

where $|\beta_j\rangle \neq |\alpha\rangle$ and E_α, E_{β_j} are the respective energy levels. Since the dipole operator \mathbf{d} only couples states of opposite parity, the linear first-order energy shift vanishes unless states of opposite parity are degenerate. Therefore, the Stark effect is generally a second-order phenomenon, leading to a quadratic dependence of the energy shift on the applied electric field: $\Delta E \propto |\mathbf{E}|^2$.

^{174}Yb $6sns\ ^1S_0$ states $|n\rangle$ have $J = 0$. Consequently, the field dependent shift can be expressed with a scalar polarizability $\alpha^{(0)}(n)$ for a fine-structure level n with energy E_n as [48]:

$$\alpha^{(0)}(n) = -\frac{2}{3} \sum_{J'} \frac{|\langle n || d || J' \rangle|^2}{E_n - E_{J'}}, \quad (3.13)$$

where the sum includes the reduced matrix elements between $|n\rangle$ and all other states $|J'\rangle$. The resulting

quadratic scalar Stark shift is given by:

$$\Delta E_n^{(0)} = -\frac{1}{2}\alpha^{(0)}(n)E^2. \quad (3.14)$$

To measure the electric field dependent energy shift in the experiment the Probe and the Control laser are tuned to a two-photon resonance. The two-photon detuning δ is set to $\delta = \Delta_{\text{Probe}} - \Delta_{\text{Control}} = 0$ and the single-photon detuning is given by $\Delta_{\text{Probe}} = 1$ GHz. In this measurement, we are interested in analyzing a signal of a pure atomic transition, not of Rydberg molecules that are observed in section 4. In order to exclude molecule contributions, the atom cloud is prepared with a short $t_{\text{BlueMot}} = 1$ to 2 s and without evaporation and compression to have an order of magnitude lower densities compared to molecular spectra. Other preparation steps are similar to section 2.1. By varying the Probe detuning and thus the two-photon detuning, I take spectra at different electric fields and obtain Stark maps. For the states $n = 41$ and $n = 42$ the Stark maps are shown in figure 3.9.

As a next step, the polarizability is obtained from the spectra by applying the following fit routine: Fitting a Lorentzian curve to the individual spectra provides the center frequencies of the transitions at different fields. These can be fitted with a quadratic model. The resulting $\chi_r^2 = \frac{\chi^2}{\text{N.D.o.F.}}$ are displayed in the figure 3.9 and quantify a very good agreement of the center frequency shift with field to the quadratic model. If the scan range of static electric field is extended to larger fields, the observed data quickly goes to a non-quadratic regime and thus the quadratic fits yielding a $\chi_r^2 > 0$. This effect stems from the mixing with other states and hybridization. From the quadratic fit $\alpha^{(0)}(n)$ is calculated and displayed in the figure 3.9.

The errors in the polarizability are obtained from the fit, where each data point is associated with a statistical error. In addition to these statistical errors, systematic errors emerge. The most significant source of systematic errors originates from uncertainties associated with the electric field. Firstly, the error at the analog voltage power supply output contributes to the systematic error. The uncertainty on the output is estimated by independent measurements of the power supply to be 1%. Resistance in the wiring between the voltage supply and electrodes are not contributing to a voltage deviation on the electrodes as we consider static fields without currents. Therefore, the uncertainty on the voltage at the electrodes, respectively on the field, propagates on alpha as

$$\frac{\Delta\alpha_U}{\alpha} = \frac{\Delta U}{U} = 0.01.$$

Secondly, another dominant source of systematic error is attributed to the position of the atomic cloud. As illustrated in figure 2.8 this affects the conversion factor c_y from applied voltage to electric field at the position of the atomic cloud. This error can be connected to

$$\frac{\Delta\alpha_C}{\alpha} = \frac{\Delta c_y}{c_y} = 0.0081.$$

Thirdly, the conversion factor itself relies on a Comsol simulation. The error of the simulation cannot be estimated. Without taking the latter into account, the total estimated systematic error on α is less than 2%.

Another information that is provided by the Stark map are the strength of residual fields orthogonal to the intentionally applied field vector. The quadratic Stark effect reflects only the absolute field magnitude

— not the direction of a single field. As mentioned in the introduction to the electric field control in section 2.3.2.1, the electrodes can be used to compensate for residual electric fields that are caused by stray fields of free charges or the field control system. Constant residual fields perpendicular to the scanned electric field to measure the Stark map will result in an offset of the parabola and residual parallel fields result in an horizontal shift. The field was scanned in all three orthogonal directions, and constant field offsets on the electrodes were adjusted. This process compensated for any residual fields. In figure 3.9(a) the horizontal shift is (0.0006 ± 0.0003) V/cm. This is at the edge of the precision of the voltage supplies. Along the other axis similar results were achieved. Important for the polarizability measurement is, that residual fields are small enough to not influence the quadratic behavior of the shift.

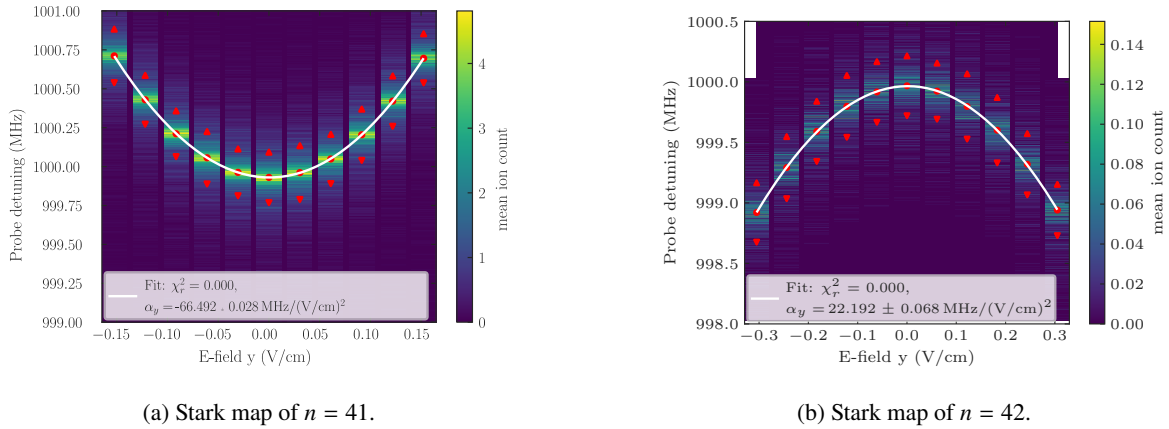
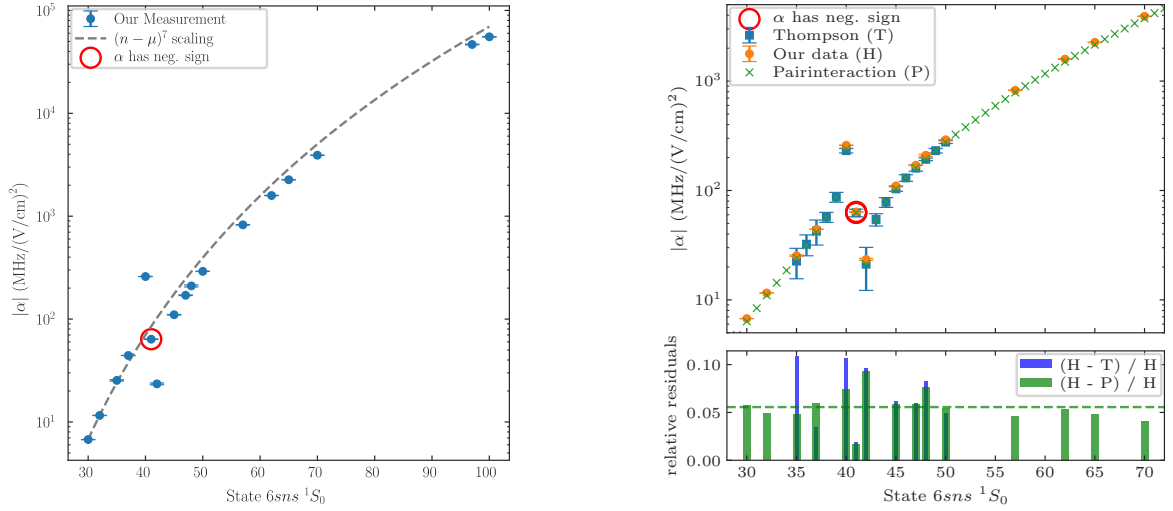


Figure 3.9: Stark maps. For different fields a spectrum with varying the Probe detuning is taken. The results of Lorentzian fits are marked in red. The two neighboring states feature polarizabilities with opposite sign. χ_r^2 was calculated for the quadratic fit and is rounded to three digits.

The measurement of Stark maps was repeated for a multitude of states, and the resulting polarizabilities, denoted by $\alpha^{(0)}(n)$, are comprehensively presented in figure 3.10(a). The expressions in equation 3.13 can be associated with a rough scaling with the principal quantum number ν : The matrix elements $|\langle n||d||J'\rangle| \propto \nu^2$ and the energy levels $E_n - E_{J'} \propto \nu^{-3}$. Therefore, the polarizability of the 1S_0 -Series scales with ν^7 . For the two-valence electron species ^{174}Yb not only $6sn's^1S_0$ states contribute to $\alpha^{(0)}$, but also other states with same electron configuration can contribute through a mixing of wave functions. In particular, the singlet and triplet states 1P_1 and 3P_1 have a mixing angle due to the inner core perturber electron described by the MCQDT model. The triplet character of the 1P_1 Rydberg states varies between $(6.30 \pm 0.03)\%$ for $n = 40$ and $(2.96 \pm 0.16)\%$ for $n = 100$ [26]. Electric fields can mix the Rydberg 1S_0 with other states that are connected via a dipole-allowed transition, e.g. the 1P_1 state. Therefore, the 1S_0 state can mix effectively with the triplet 3P_1 state. Since the 3P_1 quantum defects show a crossing with the 1S_0 defects in a Lu-Fano-like plot (cf. fig. 2.1) resulting in almost degeneracy of S- and P-orbitals of the wave function. As a result the polarizability $\alpha^{(0)}$ features a resonance around $n = 41$ [26]. Apart from the resonance, the $\alpha^{(0)}$ follows roughly the ν^7 scaling.

A comparison of the measured polarizabilities with the measurement of Peper et al. [26] and the corresponding MCQDT-model provided by *Pairinteraction* of S. Weber, F. Hummel, et al. [27] is shown in figure 3.10(b). *Pairinteraction* is based on the measurements of Peper et al.. Therefore these two traces agree well. Our data shows a systematic, in average $+(5.5 \pm 1.7)\%$ deviation to Peper et al., and a



(a) Summary of all performed measurements. Additionally an ν^7 scaling is plotted. The polarizability is negative at $n = 41$.

(b) Comparison to Peper et al. [26] and *Pairinteraction* of S. Weber, F. Hummel, et al. [27]. The residuals show a systematic $(5.5 \pm 1.7)\%$ deviation.

Figure 3.10: Static dipole polarizability of $6sns \ ^1S_0$ states.

similar deviation to MCQDT-model *Pairinteraction*. The resonance at $n = 41$ agrees best in all three data sources. The systematic deviation between the two measurements can not be explained by known systematic errors in our HV-system (cf. sec. 2.3.2.1), as these were discussed above to be smaller than 2%. A repetition measurement of $n = 30$ after several month demonstrated a reproducibility of our data up to 0.07%.

To summarize, the agreement of the our measurement to Peper et al. verifies trends and orders of magnitudes in the polarizability well. The employment of a third independent measurement has the potential to clarify the deviation attributed to systematic effects.

3.3.2 Light shift of the Control laser

Analog to eq. 3.13 the AC Stark shift of a particular non-degenerate ^{174}Yb $6sns \ ^1S_0$ state $|n\rangle$ in a light field with frequency ω and intensity $I = c\epsilon_0/2|E|^2$ is given by second-order time-independent perturbation theory [48] as

$$\Delta E_{AC} = -\frac{2}{3} \sum_{J'} \frac{\omega_{J'n}}{\omega_{J'n}^2 - \omega^2} |\langle n|d||J'\rangle|^2 |E_0|^2/4, \quad (3.15)$$

where the sum includes the reduced matrix elements between $|n\rangle$ and all other states $|J'\rangle$. $\omega_{J'n} = \omega_{J'} - \omega_n$ is the transition frequency. Only states that are very far detuned, and/or have small transition matrix elements can be neglected.

The level scheme in figure 3.11 shows the two-photon excitation from

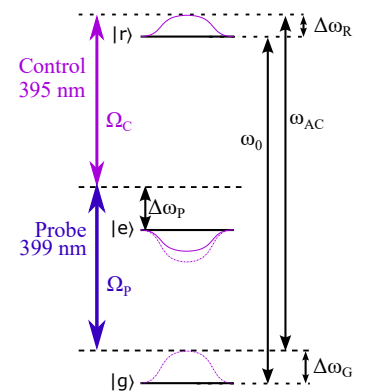
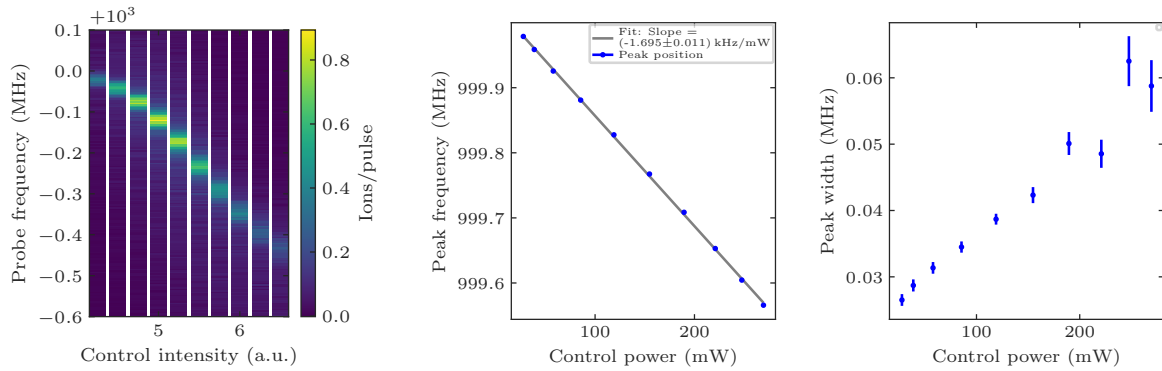


Figure 3.11: Schematic of light shifts of involved states.

$|g\rangle$ to $|r\rangle$. For the following measurement of the AC Stark shift, the single-photon detuning was set to 1 GHz. It is denoted in figure 3.11 as $\Delta\omega_p$. The colored lines around the states sketch the expected light shift. As the single Probe photons create only a very weak light field, the Control light is the sole contributor to energy shifts. The direction of shifts can be estimated from the effect of the closest contributing line. The to the $|e\rangle \rightarrow |r\rangle$ -transition red-detuned Control causes a positive shift of $|r\rangle$, and since Control is blue-detuned to the $|g\rangle \rightarrow |e\rangle$ -transition $|g\rangle$ is shifted upwards too. The unperturbed transition frequency $\omega_0 = E_R - E_G$ gets shifted by $\Delta\omega = \omega_{AC} - \omega_0 = \Delta\omega_R - \Delta\omega_G$.

To summarize the previous paragraph, within the used two-photon excitation scheme from $6s^2\ ^1S_0$ to $6sns\ ^1S_0$ it is only possible to measure differential light shifts $\Delta\omega$ between $|g\rangle$ and $|r\rangle$. A measurement of the light shift as a function of Control power is presented in figure 3.12(c) for $n = 50$. The measurement is performed similar to the measurement of Stark maps in figure 3.9 in the previous chapter, but instead of scanning the electric field, the spectra for multiple Control powers are performed (cf. fig. 3.12(a)). Assuming a perfectly aligned Control beam, the beam waist can be estimated¹ to $\omega_0 = 28.46\ \mu\text{m}$ and the control intensity can be calculated. A fit to each line provides the center frequencies. They are presented as function of the a Control intensity in figure 3.12(b). The line shifts linear with power and therefore quadratic with electric field. A linear fit to the center frequencies shows very good agreement.

Additional to the peak frequency drift, a higher Control intensity also causes a higher Rabi frequency $\Omega_{\text{eff}} \propto \sqrt{I_C}$. This leads to more Rydberg excitations, line broadening and increased heating and loss due to the anti-trapping of the Control beam. The effect of a linear line broadening is presented in figure 3.12(c). Referring back to the atomic spectra in figure 3.12(a), the three aforementioned effects initially result in an increase in peak ion counts due to an elevated Rabi frequency. This is followed by a subsequent decrease, which is attributed to the processes of heating and line broadening. The alteration in line shape does not exert an influence on the center frequency estimation in figure 3.12(b).



(a) Spectra with varied Control power.

(b) Line shift.

(c) Line broadening.

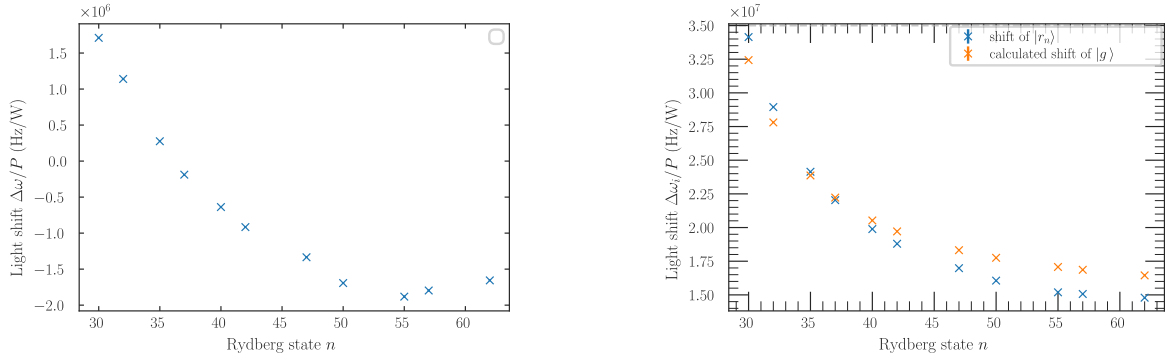
Figure 3.12: Example of light shift and broadening for $n = 50$. To measure the atomic spectrum in (a) different Control intensities were employed. Each line is fitted with a Lorentzian fit. The resulting peak center frequency is shown as a function of calibrated Control intensity in (b). An observed line broadening is shown in (c). The peak width is given here by the fit parameter Γ of the Lorentzian fit.

The differential light shift was measured for many Rydberg states. The results are presented in figure

¹ We can not measure the beam in the vacuum. Therefore it was calculated from all other beam parameters. For this analysis no further investigation of systematic errors related to the beam waist was done.

3.13(a).

As a final step, the light shift on the Rydberg state is estimated. As the major contributing transitions to the light shift of $|g\rangle$ are known from other experiments a ground state light shift can be calculated. The code for this was provided by Tangi Legrand. With the computed ground state energy shift, the pure Rydberg state light shift can be calculated. The shifts on $|g\rangle$ and $|r\rangle$ are shown in figure 3.13(b). As one can see, the light shifts of $|r\rangle$ and $|g\rangle$ have the same sign and compensate each other partly. An almost magic condition is realized around state $n = 36$.


 (a) Differential light shift $\Delta\omega = \Delta\omega_R - \Delta\omega_G$.

 (b) Rydberg and ground state light shifts $\Delta\omega_R$ and $\Delta\omega_G$.

Figure 3.13: Light shifts (AC-Stark shifts) of $6sns \ ^1S_0$ states. All data points have negligible small errors. The Control frequency is 1 GHz red-detuned to the transition to the Rydberg state (cf. fig. 3.11). The x-axis shows the Control light frequency displayed as the Control frequency corresponding Rydberg state in the two-photon Probe-Control excitation scheme.

The knowledge on the AC-Stark shifts is valuable for further experiments. For example the investigation of the Control power dependence of a polariton-physics related experiments might require a compensation of the frequency drift.

Ultralong-range ytterbium Rydberg molecules

Ultralong-range Rydberg molecules (ULRM)s can be observed under high density as a scattering phenomenon between ground state atoms and the excited electron of comparably large Rydberg atoms. The resulting interaction potential perturbatively disturbs the Rydberg electron wavefunction and allows for an effective trapping of ground-state atom(s) in distances of $10^3 a_0$ to the Rydberg core. These exotic molecules exhibit extreme spatial extent — up to micrometers in size —, long lifetimes and giant range of permanent electric dipole moments (PEDMs), arising from strong admixtures of different angular-momentum states [56, 57]. PEDMs of Rydberg molecules range from ≈ 1 Debye for S-type Rb molecules [60] to $\approx 1\,000$ Debye for trilobite Cs molecules [61]. Since their theoretical prediction [62], these ultralong-range Rydberg molecules (ULRM) have been observed [63] and extensively studied [64–67] in alkali atoms, particularly rubidium. More recently, interest has expanded to alkaline-earth-like atoms, such as strontium (Sr), which exhibit additional complexity due to their two valence electrons and associated electronic structure [68–70]. Rydberg molecules of ytterbium had been so far unexplored. One objective is the determination of the fundamental low energy scattering properties of ^{174}Yb , as the electron-neutral scattering length. As I will demonstrate in this chapter, ^{174}Yb is an exceptionally interesting playground for Rydberg molecular physics, e.g. due to the formation of a p-wave shape resonance, a rich structure of rovibrational molecular states, the observation blue-detuned molecular states, and the influence multi-channel state-mixing on the PEDM with a potential resonance at $n = 41$.

A concise overview of the formation mechanisms of Rydberg molecules is provided in section 4.1, while a comprehensive summary of research in this field is presented in the review papers [56, 57]. Section 4.2 deals with considerations for measuring Rydberg molecule spectra, while section 4.3 presents the key findings concerning Rydberg molecules. This section highlights phenomena that can be directly inferred from observations, including the formation of N -mers and the scaling of individual Rydberg states with a power law. Finally, section 4.4 demonstrates measurements of the permanent electric dipole moment of Rydberg molecules.

4.1 Introduction to Rydberg molecules

A Rydberg molecular dimer involves a positively charged Rydberg core, a highly excited Rydberg electron with an unperturbed one-electron wave function $\psi_{n_s}(\mathbf{r})$ and a perturbing ground-state atom in distance \mathbf{R} to the Rydberg core. This concept is shown in figure 4.1 (a). Analogous to a position \mathbf{r} of the

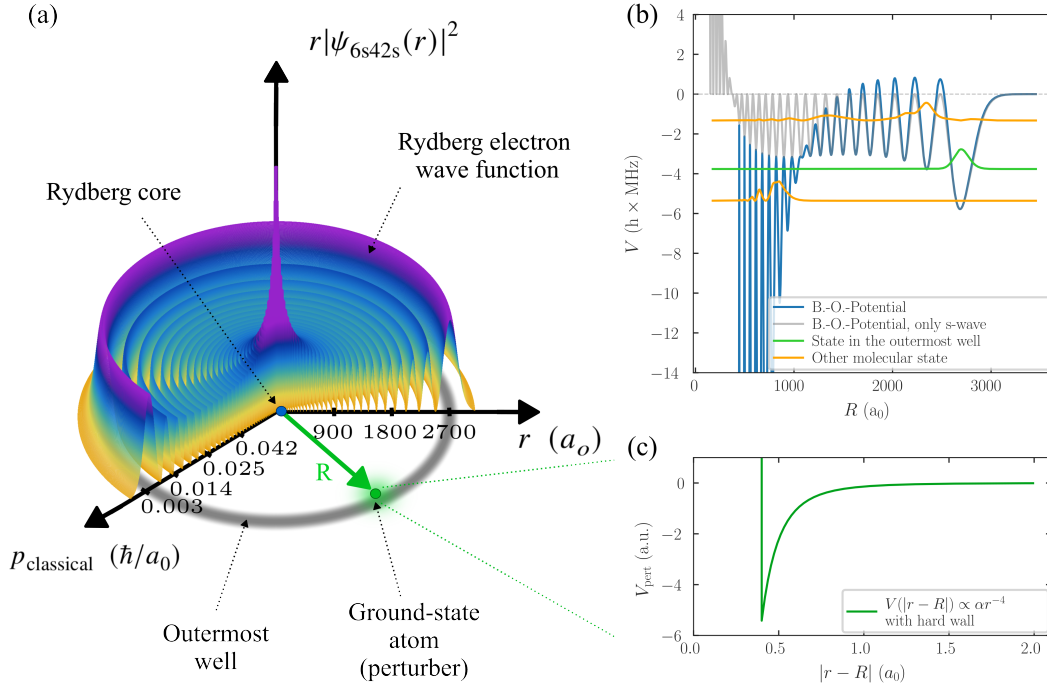


Figure 4.1: Rydberg molecule formation scheme. In (a) the unperturbed $6s42s \ ^1S_0$ Rydberg electron wave function is shown in an r - ϕ -plane. Analogous to the distance \mathbf{r} of the Rydberg electron to the core, a classical momentum $p_{\text{classical}}$ can be assigned. This is indicated by a second axis. A ground state atom at the distance \mathbf{R} to the Rydberg atom perturbs the Rydberg electron with a polarization potential (c). The molecule binding potential is given by the Fermi pseudopotential in Born-Oppenheimer approximation (b). Next to the full potential, only the s-wave contributions are plotted. Especially the outer most potential well is not affected strongly by the p-wave scattering contributions. Solving the molecular potential provides bound states, e.g. the bound state in the outermost potential well (illustrated in green), and many more rovibrational states (examples illustrated in orange). The molecular potential was calculated and solved by Milena Simić. The p-wave scattering phase shifts are not fully adjusted yet. This will influence the solutions of the non-outermost potential well states significantly. For this reason, the illustration is to be understood in qualitative terms.

Rydberg electron, a classical momentum $p_{\text{classical}} = \hbar k(|\mathbf{r}|) = \sqrt{2m_e(e^2/(4\pi\epsilon_0|\mathbf{r}|) - E_b)}$, where E_b is the binding energy, can be attributed to the Rydberg electron [62, 63]. While the complex multi-electron shell structure in ^{174}Yb significantly affects the Rydberg electron wave function resulting e.g. in a quantum defect, it is valid to assume, that the electron-neutral scattering process is a single electron effect [68].

The interaction between a Rydberg electron and a ground-state atom can be understood with the following crude model: The interaction is in first order a result of the polarization $\alpha_{|g\rangle} \approx 138.9$ a.u. of the neutral ground-state atom within the Coulomb field $\mathbf{F}(\mathbf{r}, \mathbf{R})$ of the Rydberg electron. The perturbative interaction potential resulting from this model is illustrated in figure 4.1 (c) and has the form

$$V_{\text{int}}(\mathbf{r}, \mathbf{R}) = -\frac{1}{2}\alpha\mathbf{F}^2 = -\frac{1}{4\pi\epsilon_0} \cdot \frac{e^2\alpha}{2|\mathbf{r} - \mathbf{R}|^4} \quad \text{with} \quad \mathbf{F}(\mathbf{r}, \mathbf{R}) = -\frac{-e}{4\pi\epsilon_0} \cdot \frac{\mathbf{r} - \mathbf{R}}{|\mathbf{r} - \mathbf{R}|^3} \quad [57, 71] \quad (4.1)$$

for large $|\mathbf{r} - \mathbf{R}|$, while it can be approximated with a hard wall for small $|\mathbf{r} - \mathbf{R}|$.

In summary, the formation of Rydberg molecules is a low-energy scattering problem caused by the perturbation of the Rydberg electron by a neutral, polarizable ground state atom. A common approach to solving this problem is applying the Born-Oppenheimer approximation, using a partial-wave expansion and rewriting the molecular potential as the Fermi pseudopotential [57]. This approach provides a molecular potential as a function of the atom-core distance \mathbf{R} , as illustrated in figure 4.1 (b). In the following this modeling approach is discussed in more detail:

The total molecular wave function is given in the Born-Oppenheimer approximation [72] as a product of decoupled electronic wave function $\psi(\mathbf{r}, \mathbf{R})$ and Rydberg core - ground state atom wave function $\phi(\mathbf{R})$ that only depends on the relative coordinate \mathbf{R} :

$$\Psi_{\text{mol}}(\mathbf{r}, \mathbf{R}) = \psi(\mathbf{r}, \mathbf{R})\phi(\mathbf{R}) \quad . \quad (4.2)$$

$[H_{\text{r.c.-g.a.}} + H_{e^-} + V_{\text{int}}(\mathbf{r}, \mathbf{R})]\Psi_{\text{mol}}(\mathbf{r}, \mathbf{R}) = E(\mathbf{R})\Psi_{\text{mol}}(\mathbf{r}, \mathbf{R})$ is the corresponding time-independent Schrödinger equation with the free particle Hamiltonians of Rydberg core and ground state atom summed in $H_{\text{r.c.-g.a.}}$ and the Rydberg electron Hamiltonian given by H_{e^-} . It can be solved by first computing the solution for $\psi(\mathbf{r}, \mathbf{R})$ and treating \mathbf{R} as a free parameter. This results in the molecular potential energy curves (PECs), similar to plotted in figure 4.1 (b). In a second step, one can solve for $\phi(\mathbf{R})$ to obtain rovibrational wave functions and the Eigenenergies of the molecular states.

For a spherically symmetrical scattering problem like this a partial wave expansion can be applied [71]. For low-energy scattering of a spin 1/2-electron with ^{174}Yb , the relevant scattering channels are s -, $p_{1/2}$ - and $p_{3/2}$ -wave scattering. The scattering interaction can be parameterized by the scattering length $a_i(k)$ of channel i while including a k -dependence of a_i for a more accurate description (cf. eq. 4.3). Corresponding scattering phase shifts for ^{174}Yb were calculated in [73] for higher energies. Experimental data of ultralong-range Rydberg molecules in combination with correct modeling can provide precise estimates of the scattering phase shifts for the low energy limit.

To solve this scattering problem, it is essential to rewrite $V_{\text{int}}(\mathbf{r}, \mathbf{R})$ as the Fermi pseudopotential [74]. The exploitation of the short-range character of $V_{\text{int}}(\mathbf{r}, \mathbf{R})$ in equation 4.1 enables the replacement of the distance $|\mathbf{r} - \mathbf{R}|$ with the Dirac delta-distribution δ . The approximated scattering potential is thus

derived as follows:

$$V_{\text{int}}(\mathbf{r}, \mathbf{R}) = \frac{2\pi\hbar}{m_e} a_s(k) \cdot \delta(|\mathbf{r} - \mathbf{R}|) + \frac{6\pi\hbar^2}{m_e} (a_{p_{1/2}}^3(k) + a_{p_{3/2}}^3(k)) \cdot \overleftarrow{\nabla} \delta(|\mathbf{r} - \mathbf{R}|) \overrightarrow{\nabla} \quad ,$$

respectively

$$V_{\text{int}}(\mathbf{R}) = \frac{2\pi\hbar}{m_e} a_s(k) \cdot \psi_{ns}^2(\mathbf{R}) + \frac{6\pi\hbar^2}{m_e} (a_{p_{1/2}}^3(k) + a_{p_{3/2}}^3(k)) \cdot |\overrightarrow{\nabla} \psi_{ns}(\mathbf{R})|^2 \quad [68, 75]. \quad (4.3)$$

The solution to problem 4.3 will provide the molecular binding energies and states $\phi(\mathbf{R})$. This is illustrated in figure 4.1 (b). One state stands out, that is the molecular state that forms in the outermost potential well. This state is mostly affected by scattering processes in the outermost lobe of the Rydberg electron wave function. In general, other molecular states can exhibit greater delocalization over multiple potential wells.

It should be noted, that the molecular state in the outermost potential depends mostly on the s-wave scattering. For the potential shown in figure 4.1 (b), the *s*-wave scattering length is already adjusted by our theory collaborators Matt Eiles and Milena Simić to the data provided in section 4.3. The scattering length contributions a_{p_i} of the *p*-wave scattering channels also contribute to the potential, but affect it stronger at smaller values of \mathbf{R} (larger values of the electron momentum k). Incorporating *p*-wave contributions into the scattering length results in a substantial alteration of the potential's shape for other, non-outermost potential well, molecular states. The *s*-wave scattering length is invariably negative, resulting in a purely attractive contribution to the potential. In contrast, *p*-wave contributions can also exhibit even higher negative and positive values. This can lead to a distortion of the molecular potential, with values that can exceed 0 and fall well below the outermost potential. These effects indicate a *p*-wave shape resonance caused by the admixture of steep PECs related to other Rydberg states of the manifold [75].

In the aforementioned calculations, the effect of a single ground-state atom was considered. The resulting molecule is a dimer. Next to the dimer, the formation of other poly-atomic Rydberg molecules (trimers, tetramers, pentamers, and so forth (or, in general, *N*-mers)) is also possible. For an *N*-mer, $N - 1$ perturber ground state atoms are involved, forming bound states within the Fermi pseudopotential. The individual bound states between the Rydberg atom and a ground state atom can be considered as small perturbations and to be independent. The total binding energy is the sum of the binding energies of all contributing bound ground-state atoms.

4.2 Measurement considerations

An experimental demonstration of the before presented molecule formation in form of spectra of Rydberg molecules is challenging. The following considerations will be discussed in regard to the measurements.

Density. The necessary condition for the formation of Rydberg molecules is that a ground state atom is located within the wave function of the Rydberg electron, where the electron can scatter off it. This process is statistically more probable at higher densities. Since the Rydberg wave function volume increases with ν^6 , higher Rydberg states require less density. Next to that, the atomic density can also be too high to observe the formation of single Rydberg molecules: When the Rydberg wave function extend is large compared to the atomic spacing, a mean field regime is approached. This is observed e.g. in

BEC densities. Relatively high densities are reached at high atom numbers and low temperatures. This connects to the next aspect.

Temperature. Rydberg molecules are bound by extremely weak forces, in general just a few MHz, compared to the atomic binding energies with scales of THz. This disparity in binding energies leads to the observation that even a modest thermal motion can reach kinetic energy sufficient to disrupt these fragile molecular states. Therefore, the ensemble temperature must be significantly lower than

$$T \ll \frac{E_{\text{mol. bind.}}}{k_B} \approx \frac{h \times 1 \text{ MHz}}{k_B} \approx 50 \mu\text{K}$$

Additionally, low temperatures result in a reduction of the collision rate, thereby prolonging lifetimes and reducing line widths in the spectra.

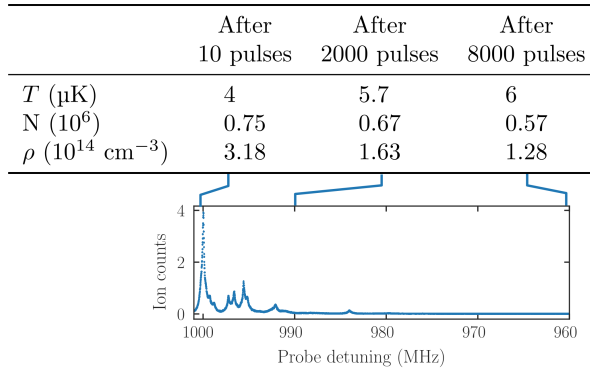


Figure 4.2: Atomic conditions (Temperature T , atom number N , Peak density ρ) along atomic spectrum for $n = 41$. The frequency is scanned in 8000 steps along 40 MHz to obtain a molecular spectrum. Given that the decay is unique to each Rydberg state, contingent on the frequency range that is scanned and dependent on the initial density (controlled by $t_{\text{Blue MOT}}$), this illustration of the density decrease during pulses and is to be understood as an example and no errors are stated.

Heating effects due to exposure to Probe and Control. Density and temperature are not constant over the molecular spectra due to the applied measurement technique (cf. fig. 4.2). Each molecular spectrum presented here is a mean of several identical experimental cycles (cf. sec. 2.2). Since the Probe frequency is scanned along the pulses, each prepared atomic cloud results in a full spectrum. While scanning frequency, also the density and temperature of the ensemble evolve in time. Two main effects were observed: Due to the blue-detuned Control beam, an anti-trapping effect occurred, resulting in a collective motion and heating of the cloud. The trap depth of the dipole trap is typically about $-200 \mu\text{K}$. The Control beam forms a repelling trap in the center of the atomic cloud. Control beam and Dipole Trap activated alternating in time 2.21. But this is not the only effect leading to heating and loss, as an additional dependence of the atomic cloud parameter time evolution on the Probe intensity was observed. This implicates a heating process through recoil of absorbed photons. The transmission at the beginning of a molecular scan is typically 20 %, while the number of probe photons per pulse is approximately 500. The photons can either be absorbed by far-detuned (1 GHz) single photon absorption, or via a two-photon process by absorption to a Rydberg state. After 8000 pulses, only a 25 % atom number

decrease and 50 % increase in temperature is observed, but the density decreases by a factor of ≈ 3 . This is dominated by the expansion of the cloud through heating.

Resolution limit of our spectroscopy. The first main objective of measuring Rydberg molecule spectra is to extract molecular binding energies, given by the distance of the atomic transition to peaks of molecular states. The binding energies can be used to extract the different scattering length contributions. The identification of peaks in molecule spectra is limited by the resolution of our spectroscopy setup. The resolution limit is the natural linewidth of molecular lines, which is determined by their lifetime until a decay. In addition, the molecular lines are intrinsically broadened due to a further reduction in lifetime in the finite temperature atomic ensemble.

A major contribution to the line broadening constitutes the band width of the Probe pulse. The waveform of the Probe pulse can be disassembled into its spectral components by Fourier transformation (cf. fig. 4.3 (a), (b)). The bandwidth of a pulse is determined by its length. The presence of small pedestals and sidelobes in the frequency space can be mitigated by employing pulse shapes such as the used Tukey pulse. The consequence for spectral lines is a broadening given by the convolution of the pure lineshape with the spectrum of the Tukey pulse (cf. fig. 4.3 (b)). Sidelobes and the peak width are strongly dependent on the duration of rising and falling edges of the Tukey pulse and the length of the pulse. As illustrated in Figure 4.3 (c), the data demonstrate a consistent trend between the limit of the

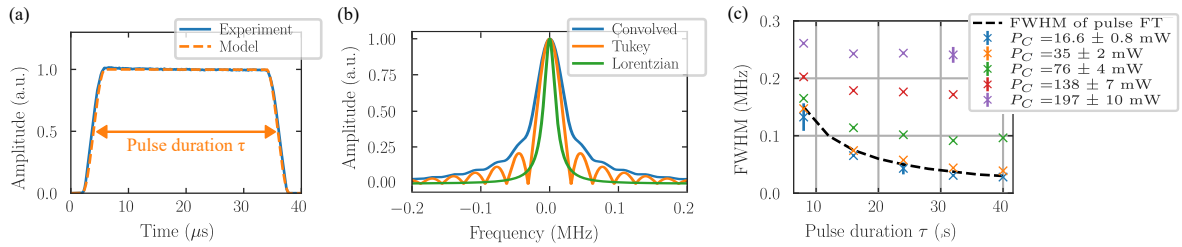


Figure 4.3: Fourier broadening of spectral lines. Figure (a) shows a Tukey shaped model pulse and a measured pulse of duration $\tau = 32 \mu\text{s}$. Exactly this pulse was used for all Molecule spectra measurements. Figure (b) shows the Fourier transformation of the model Tukey pulse convoluted with a Lorentzian of line width $\Gamma = 20 \text{ kHz}$. Figure (c) shows the measured FWHM of atomic transitions at different control powers P_C in comparison to the FWHM of the Fourier transformed pulse.

FWHM of the Tukey spectrum and the linewidth of the atomic transition when varying the pulse length. In this measurement, the spectral line FWHM are below the Fourier limit due to measuring the lines in the non-linear regime of the detector (ion count rates are between 1.5 and 2.5 ions/pulse). To find an optimal pulse duration τ , a trade-off between Fourier broadening and atom heating and loss due to non-trapping during probing (cf. fig. 2.21) is considered. An optimum was found at $\tau = 32 \mu\text{s}$. This results in a probe pulse bandwidth limited contribution to the linewidth of $\Delta_{\text{Fourier}} = 37.5 \text{ kHz}$.

A secondary, substantial broadening mechanism of the spectral peaks is power broadening [48]. As illustrated in figure 4.3 (c), a quadratically with P_C increasing broadening effect is measured while the Probe power was maintained at a constant level. To mitigate the power broadening effect, it is necessary to operate at the lowest possible Control and Probe power while still acquiring sufficient statistics. This is especially challenging for lower Rydberg states as their ion detection efficiency decreases (cf. sec. 3.1.2).

Additionally, other inhomogeneous broadening mechanisms, the extent of which remains unknown,

might contribute to the spectrum in an not quantitatively determined fashion. The probed atomic cloud that is trapped in an harmonic potential of the dipole trap can be modeled as having a Gaussian distribution of atomic density and temperature. This distribution is overlapped with a Gaussian Control intensity distribution. Variations in light shifts, effects due to collisions, and similar phenomena across the probed medium will cause broadened and skewed lines.

The line width of the exciting lasers is a negligible contribution [17]. Typical dimer state of the outermost well line width range from 80 to 300 kHz.

4.3 Spectroscopy of Rydberg molecules

The formation of Rydberg molecules is achieved through a process known as photoassociation (PA) [76], which is addressed over a two-photon transition with 1 GHz detuning (cf. sec. 2.2). PA allows a resonant transition from free atomic states to bound rovibrational states within the molecular potential. The transition probability Γ_{im} , also called Franck-Condon factor, corresponds to the peak height in a perfect molecular spectrum. It is governed according to the Franck-Condon principle by the overlap of the final molecular and initial atomic wave function χ_m and χ_i : $\Gamma_{im} = P \propto |\langle \chi_m | \chi_i \rangle|^2$ [76]. The molecular binding energies are obtained by comparing the two-photon detuning of molecular states to the atomic transition as a reference.

As illustrated in figure 4.4, molecular spectra for $n = 42$ and $n = 45$ are shown for varying densities. At low densities, the spectrum predominantly exhibits prominent dimer peaks. For the shown spectra, the highest peak can be attributed to the dimer state of the outermost well, as this state possesses typically the highest Franck-Condon factor. Another way to identify the dimer peak in the outermost potential well will be presented in figure 4.5. In addition to the dimer state of the outermost well, there are molecular states with slightly higher binding energy, corresponding mostly to higher excitations in the outermost potential well and very shallow bound states that correspond to states that are stretched over many wiggles of the potential, as sketched in figure 4.1 (b). These are highly sensitive to the p-wave scattering phases. Additionally, there are states with lower binding energies than the state of the outermost well. One of these type of states is also sketched in figure 4.1 (b)). It is important to note that, although not illustrated in this thesis, blue to the atomic line detuned molecular states were observed. The latter two effects are indicators for a p-wave shape resonance. In addition to the peaks that can be attributed to dimers, I will present the identification of peaks that correspond to poly-atomic molecular states.

Poly-atomic Rydberg molecules (N -mers). At higher densities the probability of perturbation of the Rydberg electron by several ground state atoms increases. Poly-atomic Rydberg molecules involving N atoms can be called N -mers. Assuming small perturbations, the binding energy of the N -mers is the sum of all involved dimer states. In case of n_2 dimer states, the number of states n_N of an N -mer molecule is given by

$$n_N = \binom{n_2 + N - 2}{n_2 - 1} .$$

The resulting molecular spectrum contains numerous individual peaks that are coupled in position. The total spectrum $S(\delta)$ with an atomic transition $S_{\text{atomic}}(\delta)$, n_2 dimer states $S_{\text{dimer}}(\delta)$, and all N -mer

contributions $S_{N\text{-mer}}(\delta)$ is given by:

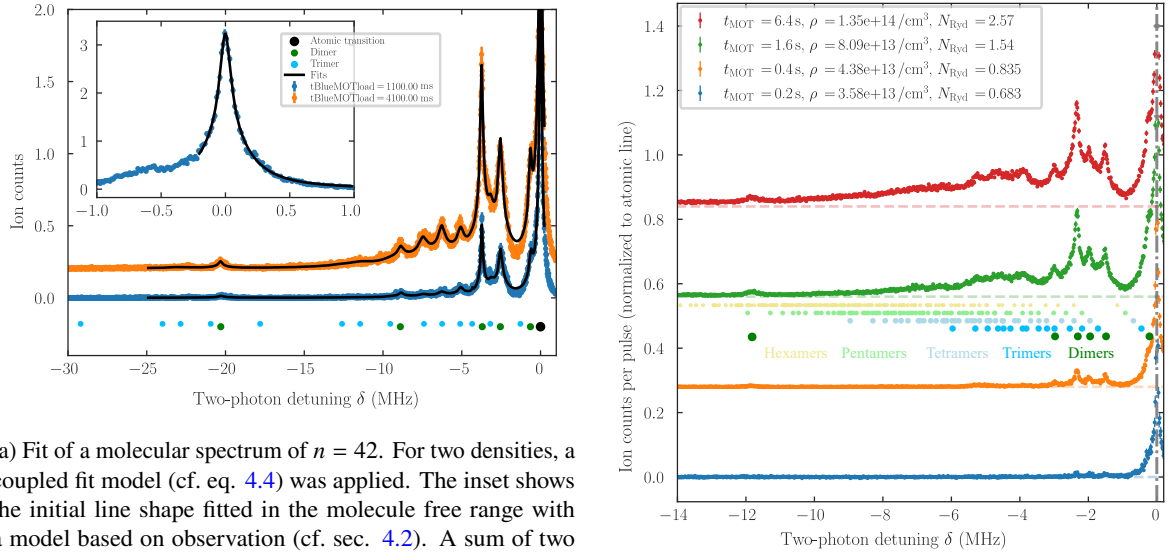
$$\begin{aligned}
 S(\delta) &= S_{\text{atomic}}(\delta) + S_{\text{dimer}}(\delta) + S_{N\text{-mer}}(\delta) \\
 &= L(\delta, A_a, \Gamma_a, 0) + \sum_{i=1}^{n_2} L(\delta, A_i, \Gamma_i, \nu_i) + \sum_{k=3}^N \sum_{\substack{\{i_1, \dots, i_{k-1}\} \\ i_j \in \{1, \dots, n_2\}}} L\left(\delta, A_{i_1, \dots, i_{k-1}}, \Gamma_{i_1, \dots, i_{k-1}}, \sum_{j=1}^k \nu_{i_j}\right),
 \end{aligned} \tag{4.4}$$

with the Lorentzian base function $L(\delta, A, \Gamma, \nu) = A \cdot \left(1 + \left(\frac{\delta - \nu}{0.5\Gamma}\right)^2\right)^{-1}$ or a similar base function.

In the model, the atomic transition is defined by the line shape parameters amplitude A_a and peak width Γ_a . The dimer states have an independent frequency offset to the atomic transition ν_i . The N -mer states, consisting of $N \geq 2$ ground state atoms, have peak positions at sums of the frequencies $\delta\nu_i$ of the involved dimer states i . For each molecular peak, two free, independent parameters for amplitude and width are pertinent. As illustrated in Figure 4.4(a), the model is applied to dimer and trimer states. A dimer can be immediately identified as a dimer, if it is not a harmonic of other dimer states. The height of a trimer state's peak can be attributed to the argument that dimer states with a high Franck-Condon factor are more likely to form trimers, resulting in higher trimer amplitudes. This effect is overlapped with the decreasing probability due to density decay along the scan direction during the measurement.

Another method of differentiating the different classes of N -mers is given by their different amplitude scaling behavior with density. As illustrated in Figure 4.4(a), trimers are nearly absent at low densities. For higher Rydberg states, the wave function extend increases, and therefore also the probability to find perturber atoms in the wave function volume. For $n = 45$, N -mers up to pentamers can be clearly identified. In this state, the most effective method for identifying the different classes of N -mers is through their scaling with density. In the case of low densities, the dimers exhibit the highest relative amplitude; however, as the density increases, the trimers gain faster amplitude than the dimer. Similar, at high densities, the tetramers exhibit faster growth compared to the trimers. For $n = 45$, the number of contributing perturber atoms per Rydberg atom is so high, that a mean field regime is almost reached. The application of the aforementioned model yields too many free parameters with respect to resolution and data sampling to fit all peaks of all N -mer classes without overfitting peaks with a low binding energy. Due to the strong dimer lines and the coupling of positions, it is still possible to extract binding energies (a fit is shown in the appendix A.7).

A subsequent stage of complexity could involve the coupling of amplitudes according to the corresponding Franck-Condon factors and peak width, for example, according to the lifetimes of the molecular states. Achieving this objective requires a more sophisticated theoretical model of the Rydberg molecule binding mechanism than is currently available, a better understanding of the sub-threshold field ionization process and a perfect characterization of the density decay across the spectrum.



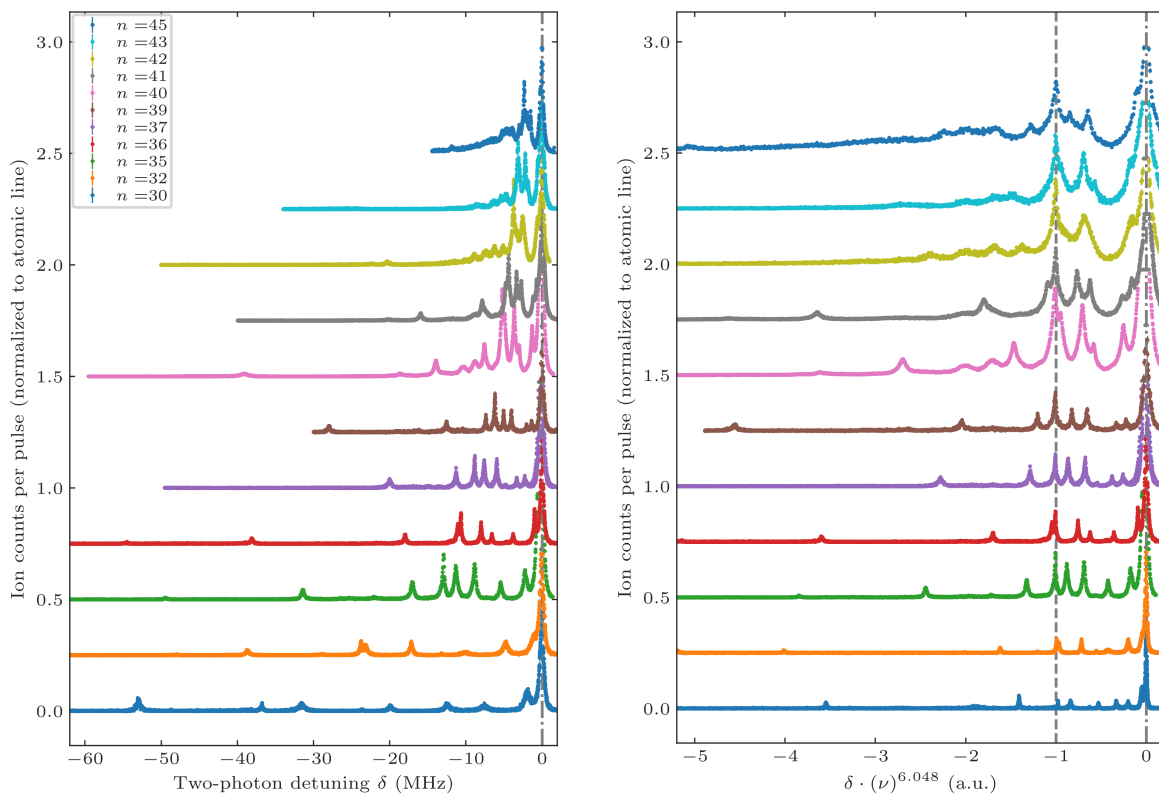
(a) Fit of a molecular spectrum of $n = 42$. For two densities, a coupled fit model (cf. eq. 4.4) was applied. The inset shows the initial line shape fitted in the molecule free range with a model based on observation (cf. sec. 4.2). A sum of two coupled lorentzians, with the same position, and optimal ratios $\Gamma_1/\Gamma_2 = (0.245 \pm 0.008)$ and $A_1/A_2 = (2.0 \pm 0.2)$ fits best. By setting the global amplitude and global width of this line shape as free parameters, it is used for all fitted peaks in the coupled model. The counts were corrected according to eq. 2.5 to linearize the detector. The fit agrees well, justifying the approach of applying the atomic line shape to all peaks. The overestimation between first and second dimer peak arises since the model does not capture the decay of density along the spectrum.

(b) Density scaling of spectrum of $n = 45$. The grey line indicates the atomic transition at 0 MHz. Marked are the positions of 5(+1) dimers, 15 trimers, 35 tetramers, 70 pentamers, 126 hexamers. The dimer positions can be extracted with a coupled fit model. The N -mers of the lowest bound dimer are not marked. Varying the MOT loading time t_{MOT} allows to access different densities, that can be stated in ground state atoms per Rydberg wave function volume N_{Ryd} . All four spectra are normalized to their atomic transition.

Figure 4.4: Spectra of polyatomic Rydberg molecules.

Scaling of molecular binding energies with Rydberg state. The next challenge is the identification of the corresponding dimer states in molecular spectra across different Rydberg states. As comprehensive overview of Rydberg molecule spectra is illustrated in figure 4.5(a), ranging from $n = 30$ to 45. Within this range, the resolution is sufficiently high to resolve features and the binding energies are sufficiently small to capture the spectrum with high sampling in a single cycle of the experiment using up to 8000 pulses. The number of pulses, resolution, and scan range were adapted for each n . Each spectrum displays a dimer state of the outermost well (typically with the highest amplitude), several with reference to this outermost well state red and blue detuned vibrational dimer states, and states with high n show additional N -mer contributions. The $\delta = 0$ position corresponds to the pure atomic transition and is obtained by fitting the atomic transition at low densities. A density-dependent red shift due to mean-field effects as in reference [64] was not observed for the investigated, comparably low Rydberg states.

The dominating trend observed among the spectra is an with $(n - \mu)^{-6} = \nu^{-6}$ scaling decrease of the binding energy. This trend is particularly evident for peaks with binding energies ranging from the dimer state in the outermost potential well to 0. Notably, the outermost potential well states exhibit a precise alignment with this trend, as illustrated by the rescaling of the x-axis with the inverted power law (see paragraph below for a detailed explanation). The following observations are obtained: The outermost potential well states deviate slightly from this trend for low n . Molecular states blue-detuned to the dimer state of the outermost well appear to oscillate irregularly around the ν^{-6} trend. The number of



(a) Molecule spectra according to the two-photon detuning δ . (b) Molecule spectra with the x -axis rescaled by the power law δ is equivalent to the binding energy of the molecular states. (cf. fig. 4.6) and normalized to the dimer peak in the outer most potential well of the states with $n > 35$. All spectra are normalized.

Figure 4.5: Overview over molecular spectra of several Rydberg states at highest density.

molecular states blue-detuned to the dimer state of the outermost well varies for different n . Molecular states red-detuned to the dimer state of the outermost well can be assigned to specific classes with each class following a hyperbolic trend. The existence of these peaks can be plausibly attributed to a p-wave shape resonance and the admixture of Butterfly states [75].

Additionally, to the peaks in the shown spectra, even more molecular states with large binding energies blue- and red-detuned to the atomic transition were observed. Similar to the peaks with a very low binding energy, these scale not with the power law. A more thorough examination of these phenomena is beyond the scope of this thesis.

Power law and identification of the state in the outermost potential well. In the following discussion, the binding energy scaling of the Rydberg spectrum will be discussed in more detail. To this end, the extraction of all peak positions in the spectra is conducted by means of fits¹, and a power law is subsequently matched with the states. This approach is illustrated in figure 4.6.

¹ More details on the fitting procedure and all fits can be found in the appendix, cf. A. Here, also a realistic review on the quality of the fits is stated.

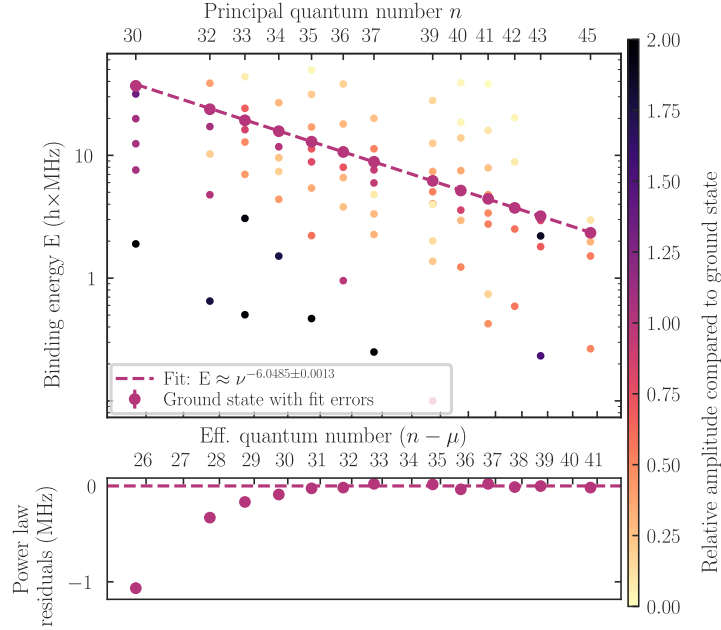


Figure 4.6: Extracted positions of peaks. This is based on the fits in the appendix A. Details on each spectrum can be seen here. The color code corresponds to the peak amplitude normed to the pure dimer peak height from the fit. In contrast to figure 4.5(a), the peak height is corrected for effects of overlapping peaks, e.g for $n = 43$ two states overlap strongly. But in general, the dimer peak is most prominent.

The binding energy of the lowest molecular dimer state that forms in the outermost potential well can be reliably predicted through a Rydberg atom size scaling argument [64]. The relation is given by a power law of $E_B \propto \nu^{-b}$. As the Rydberg electron wave function scales with ν^2 , the wave function volume scales with ν^6 . The scattering potential scales analogously, and its mean depth $\bar{V} = (\int dr^3 V(r)) / (\int dr^3)$ will decrease anti-proportional to the volume. Therefore, $b \approx 6$. A fit of the dimer state in the outermost potential well of the states with $n > 35$ results in $b = (6.0485 \pm 0.0013)$ (cf. fig. 4.6). Deviations from the exact power law can be attributed to slight alterations in the configuration of the outermost potential well for low Rydberg states. These deviations may be attributed to effects related to the second valence electron or to the momentum dependence of the scattering process and consecutive mixing of different scattering channels at low Rydberg states. In [64] an exponent of (6.26 ± 0.12) was found for Rb. The value for ^{174}Yb shows less deviation from the theoretically predicted value of 6.

Since no other peaks align in the log-log plot in figure 4.6 no other peaks scale exactly with a power law. The dimer states in the outermost potential well can be identified well. Further analysis was not pursued. Subsequently, a comparison of these data with a theoretical model could provide a basis for a full model of the states. Matt Eiles and Milena Simić were able to demonstrate a good agreement between theory and experiment regarding the dimer state in the outermost potential well by adjusting the s-wave scattering length to the presented data. Based on this they extracted an s-wave scattering length $a_s(k = 0) = -8.5 a_0$ for the low-energy electron-neutral scattering of ^{174}Yb . Adjusting the p-wave phase shifts might yield a model for all other observed states.

4.4 Permanent electric dipole moment of Rydberg molecules

The parameter that describes the behavior of a Rydberg molecular state in an electric field \vec{E} is the electric dipole moment [77]. In general, an electric dipole moment \vec{d} , arises from a separation of charges and is calculated with the displacement vector \vec{r} of the charge q classically as

$$\vec{d} = q \cdot \vec{r} \quad . \quad (4.5)$$

Every dipole moment causes a Stark effect, resulting in an energy shift given by

$$\Delta E_{\text{Stark}} = \vec{d} \cdot \vec{E} \quad . \quad (4.6)$$

Typically, dipole moments are given in Debye, where $1 \text{ Debye} = 0.5 \text{ MHz}/(\text{V}/\text{cm}) = 3.34 \times 10^{-30} \text{ Cm} = 0.39 \text{ ea}_0$.

One differentiates between permanent or induced dipole moments. Rydberg atoms and molecules possess induced dipole moments. An induced dipole moment is the result of the polarization of an atom or molecule by an electric field. In general, that can be characterized by the polarizability α for small fields. This results in $\vec{d} = \alpha \vec{E}$. Substituting this expression into eq. 4.6 yields a second-order quadratic energy shift [77]. This effect was studied in section 3.3.1. The following demonstrations will already account for an energy shifts due to an induced dipole moment according to the measured polarizabilities of the different atomic Rydberg states, n .

Formation of a permanent electric dipole moment in Rydberg molecules. In contrast to the induced dipole moment, a classical permanent electric dipole moment (PEDM) exists even without an applied electric field and is caused by a permanent separation of charges. In general, permanent dipole moments are not observed in homonuclear, "chemically bound", diatomic molecules such as diytterbium Yb_2 , or Cs_2 , since these molecules have a symmetric structure with a symmetrical electron distribution around the identical atoms. An exception to this are ultralong-range Rydberg molecules [62]. In ultralong-range Rydberg molecules the symmetry is broken because the two atoms are in electronically very different states and thus they can form PEDMs [77]. In Rydberg molecules, the attractive electron-ground state polarization interaction results in the binding of the ground state atom to the Rydberg atom (cf. sec. 4.1). This causes a disturbance of the Rydberg electron wave function and an attraction of the Rydberg electron slightly to the position of the ground state perturber compared to the rotationally symmetric Rydberg atom wave function [77]. The calculation of this effect can be performed through diagonalization of the slightly perturbed electron eigenfunctions [59, 77]. Due to the large extent of the Rydberg wave function even a slight pull to the region of the ground state atom and can lead to a significant charge separation and thus from this semi-classical point of view to a PEDM.

From a quantum mechanical point of view, any molecule has to be described with a wave function. In general, unperturbed eigenstates have definite parity, determined by the angular part of the wave function. A pure state with definite parity cannot exhibit a permanent dipole moment, since the dipole operator is odd and its expectation value vanishes². However, the disturbance of the Rydberg electron wave

² A quantum state $\psi(\vec{r})$ has definite parity (even or odd) if $\psi(-\vec{r}) = +\psi(\vec{r})$ or $\psi(-\vec{r}) = -\psi(\vec{r})$. The electric dipole operator \vec{d} is proportional to position (\vec{r}), so has odd parity, since $\vec{r} \rightarrow -\vec{r}$ under spatial inversion. For an electric dipole transition between states ψ_i and ψ_f , $\langle \psi_f | \vec{r} | \psi_i \rangle \neq 0$ only if the initial and final states have opposite parity. Therefore, for a state $\psi(\vec{r})$ with definite parity: $\langle \psi | \vec{r} | \psi \rangle = 0$.

function by the ground state atom can admix states of opposite parity, breaking symmetry and allowing the molecule to display a net dipole moment [60, 78]. A theoretical description and an experimental observation of this effect in Rb by reference [60] proves the observation that homonuclear molecules can possess a **PEDM**. The **PEDM** of Rb S-type Rydberg molecules decreases with $1/\nu^2$ [60].

In ^{174}Yb Rydberg atoms, the situation is due to the multi-electron character even more complex: Firstly, the different channels converging to the same threshold show state mixing, i.e. the singlet-triplet mixing between 1P_1 and 3P_1 series given by a state dependent **MCQDT**-mixing angle [26]. Secondly, some states of different series are near degeneracy due to crossing quantum defects, i.e. the 1S_0 and 3P_1 states around $n = 41$ (cf. Lu-Fano plot in figure 2.1). That could lead to facilitated state-mixing. Taking this into account a deviation from the $1/\nu^2$ scaling is expected with a maximum **PEDM** probably around $n = 41$.

Effect of a **PEDM on molecular spectra in electric fields.** As I will show with experimental data, ^{174}Yb Rydberg molecular states exhibit **PEDMs** of approximately 1 Debye. According to equation 4.6 a **PEDM** manifests as a linear energy shift [77]. However, due to the random orientation of molecules, a spectrum of molecules that possess a **PEDM** displays a linear splitting of a large number of (nearly) degenerate molecular rotational states leading to an effective linear broadening. Therefore, the main experimental observation of the **PEDM** \vec{d} is via the broadening of molecular peaks in dc-electric fields. As illustrated in figure 4.7, this broadening is characterized by a flattening of the peak top and a decrease in amplitude. Above $|\vec{E}| \approx 1 \text{ V cm}^{-1}$ the broadening is larger than the peak separation resulting in mixing and overlapping peaks. The broadening trend of the dimer state of the outermost well peak (marker *) is approximately linear with electric field. In general, the molecular states blue-detuned to the dimer state of the outermost well, so less strongly bound molecular states, broaden similar fast as the state in the outermost well. The red-detuned states to this molecular state broaden significantly faster (as the left peak in the picture for $n = 39$). To summarize: All observed molecular states exhibit **PEDMs** that result in a linear broadening of peaks.

In contrast, the atomic transition shows almost no comparable broadening trend, but a decrease in amplitude. This could indicate that, due to the perturbation by electric fields, the coupling, respectively the transition matrix element between the new perturbed states is modified compared to the initially involved states. A quantitative comparison of the model and experiment was not performed and deeper investigation of this observation needs to be assessed in the future.

Modeling of line broadening through a **PEDM.** This paragraph provides a more detailed quantitative description of the broadening. Due to \vec{d} the molecule states experience in an applied electric field \vec{E} an additional energy shift $\Delta E = -\vec{d}\vec{E}$ that depends on the spatial arrangement of \vec{d} and \vec{E} .

Intuitively, each molecules binding energy can deviate now maximally by additional $\Delta E_{\text{max}} = \pm|\vec{d}||\vec{E}|$. The resulting line shape at $|\vec{E}| > 0$ can be simulated by summing over high number of single unperturbed line shapes (e.g. observed at $|\vec{E}| = 0$) that each have a randomly sampled spherically homogeneous distributed **PEDM** \vec{d} . This is equivalent to a randomly sampled center frequency of the lines shifted by $\Delta E = |\vec{d}||\vec{E}| \cos(\theta)$ according to a uniform distribution of $\cos(\theta) \in [-1, 1]$. This takes the spherically homogeneous character into account. The resulting line shape is illustrated in figure 4.8.

An analytical model for the line broadening is given by the following arguments: The broadening of the line is determined by the probability distribution $P(\Delta E)$. $P(\Delta E)$ can be calculated by the argument

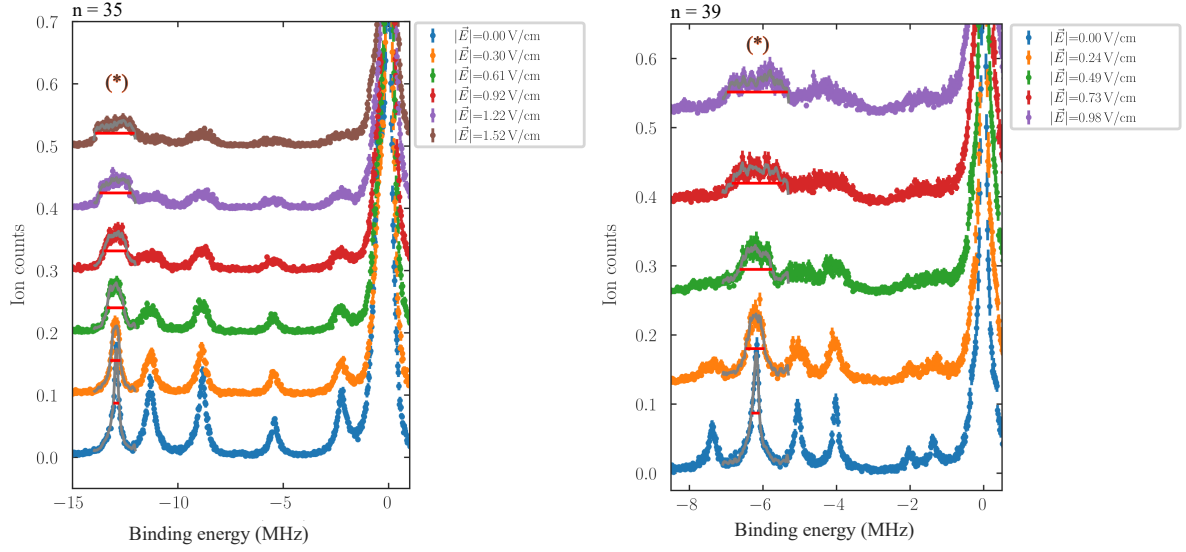


Figure 4.7: Broadening of molecular peaks in an electric field along Y-axis for two Rydberg states. The x-axis states the binding energy relative to the center the atomic transition estimated by a Lorentzian fit of the atomic peak. This way, the quadratic stark shift of the two-photon transition is compensated. The FWHM of the dimer groundstate peaks (red line) is a visualization of the broadening and is obtained after applying a running average of 4 data points (grey line). The electric field was applied along the y-axis.

that the cumulative distribution $\text{CDF}(\Delta E)$ and $\text{CDF}(\cos \theta)$ must be equivalent for all ΔE and $\cos \theta$:

$$\text{CDF}(\Delta E) = \int_{-\vec{d}\vec{E}}^{\Delta E} P(\Delta E) d\Delta E = \int_{-1}^{-\cos(\theta)} P(\cos \theta) d \cos \theta = \frac{1}{2} [1 - \cos \theta] = \text{CDF}(\cos \theta).$$

Here $\cos \theta \in [-1, 1]$ and $P(\cos \theta) = 0.5$. After substituting $\cos \theta = -\Delta E / (|\vec{d}||\vec{E}|)$ and its derivation follows

$$P(\Delta E) = \frac{d}{d\Delta E} \frac{1}{2} \left[1 + \frac{\Delta E}{|\vec{d}||\vec{E}|} \right] = \begin{cases} \frac{1}{2|\vec{d}||\vec{E}|} & \text{if } |\Delta E| < |\vec{d}||\vec{E}| \\ 0 & \text{else} \end{cases} = \frac{1}{2|\vec{d}||\vec{E}|} \Theta(|\vec{d}||\vec{E}| - |\Delta E|)$$

with the Heavyside function Θ . The final line shape $f(E)$ for a molecule state with binding energy E_0 is given by the convolution

$$f(E) \propto L(E, \dots) * \left(\frac{1}{2|\vec{d}||\vec{E}|} \cdot \Theta(|\vec{d}||\vec{E}| - E) \right) \quad (4.7)$$

with $L(E, \dots)$ being the line shape of the molecular peak without an applied field.

As a consequence of equation 4.7, the broadening of an initial known peak shape is determined solely by a single parameter, the broadening $B = |\vec{d}||\vec{E}|$. This parameter is coupled to the width and height of the new peak. Therefore, the absolute dipole moment $|\vec{d}|$ can be obtained directly from a single spectrum if the field $|\vec{E}|$ and broadening B are known.

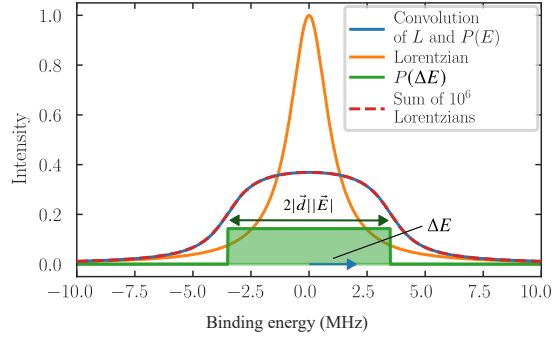


Figure 4.8: Illustration of the broadening mechanism of a molecular state with a PEDM. The initial line shape is assumed to be Lorentzian with a width $\Gamma = 2$ MHz, for the probability distribution $P(\Delta E)$, I assumed $|\vec{d}||\vec{E}| = 3.5$ MHz. The convolution (cf. eq 4.7) is processed with `np.convolve()`. The sum of Lorentzians with randomly sampled center-frequency is in perfect agreement with the calculated convolution.

Extracting PEDMs. In figure 4.9(a), a fit of equation 4.7 to the data set with $n = 37$ is presented. Fits of $n = 35$ and $n = 39$ are presented in the appendix A. The following is a concise overview of the fitting procedure: Prior to the fitting process, each individual spectrum is normalized to the atomic transition after correcting for the deadtime nonlinearity (cf. sec. 2.3.2.3) to compensate the general decrease of overall signal amplitude³ at higher fields. All spectra are aligned to a Lorentzian fit of the atomic peak frequency to compensate the quadratic Stark shift. Subsequently, a fitting range is selected based on the separation of peaks. As a first step, a precise modeling of the initial, unperturbed molecular line is crucial for the precise fitting of the broadening. Motivated by observation the shape of the field-unbroadened (but Fourier-broadened) peak at $|\vec{E}| = 0$ is approximated with a model consisting of a sum of two Lorentzians, each with the same center frequency and coupled width and amplitude. For $n = 37$, the following parameters are determined: $\Gamma_1 = (0.160 \pm 0.011)$ MHz, $\Gamma_{\text{rel}} = (0.183 \pm 0.012)$, and $\text{Ampl}_{\text{rel}} = (2.68 \pm 0.43)$. As a second step, the broadening is fitted to the data with the only free parameter being $B = |\vec{d}||\vec{E}|$ and an x-shift x_0 . The later can compensate small differences of the quadratic Stark shift between molecular and atomic states. The fit function interpolates the data points to upscale the sampling of the step function Θ by a factor 5. To avoid numerical artifacts at the edges of the convolution, the data is zero-padded, while $L(E, \dots)$ is calculated for the zero-padded data points. The convolution is performed using `scipy.signal.convolve(..., method='direct')`. After the calculation, the result $L(E, \dots)$ is mapped back onto the data resolution.

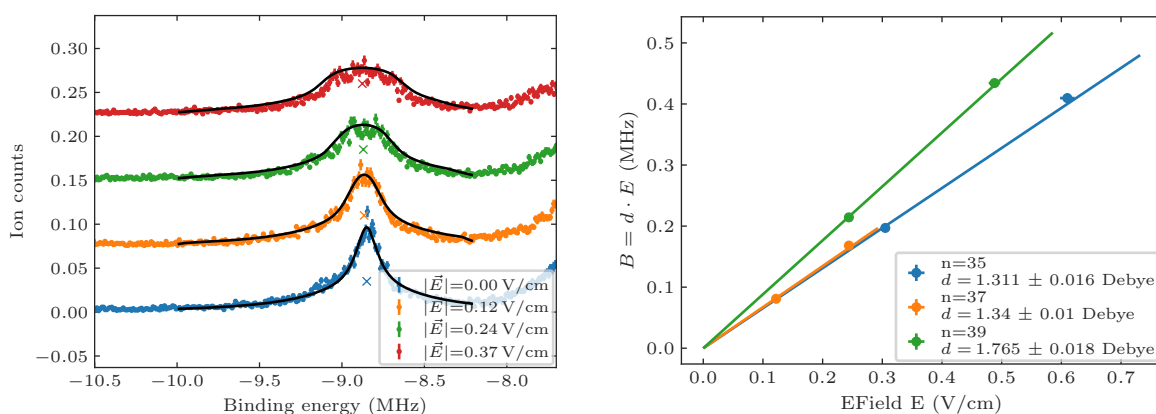
Overall, the fit shows a good agreement to the data both in width and in amplitude for low fields. This verifies a peak shape change dominated by the effects described above related to the PEDM. For higher fields a small descriptancy of the model to the data is given at the edges of the peaks, where the fit systematically overestimates the broadening. This effect increases at higher fields. Possible explanations are: Firstly, the broadened neighboring peaks create an offset. A further optimization of the fitting could be to include also neighboring peaks in a more complex model. Secondly, the amplitude estimation may be flawed due to the convolved situation of detector nonlinearity and a diminution⁴ of the overall

³ A decrease of the amplitude of atomic and molecular peaks increasing with applied field was observed but not deeper investigated. Possible explanation could be a reduction of Rabi-frequency in electric fields.

⁴ See footnote on the last page.

amplitude of the full signal in electric fields. Further analysis could include a decoupling of amplitude and width in the broadening model. Therefore, only the two lower fields were included in further analysis. The parameters obtained for the lowest electric field have the smallest fit error. Utilizing a linear fit with a fixed origin, the dipole moment can be extracted, as demonstrated in figure 4.9(b). For all three investigated Rydberg states, the first two fields align very well to a linear relation.

In addition, a slight red shift of the peak center is visible. This effect is attributed to the disparity between the quadratic stark shift in the molecular state and that in the atomic state. Given that the atomic state was employed to compensate for the quadratic stark shift, a minor relative frequency drift of the molecular levels can be discerned.



(a) Fit for the in an electric field broadened molecule spectrum for $n = 37$. The field was applied along the y-axis. Each spectrum is normalized after the detector nonlinearity was corrected and aligned to the atomic transition. A very detailed description on the fitting routine can be found in the text. For higher fields the fit overestimates the broadening.

(b) Extraction of dipole moment from the broadening. A linear fit with fixed origin provides the dipole moment. Fits for $n = 35, 39$ can be found in the app. A. Only the spectra of the first two applied fields resulted in good fits. The error on B stems from the fit and the error on \vec{E} is an assumed uncertainty on the field.

Figure 4.9: Extraction of the dipole moments for $n = 35, 37, 39$

Scaling of the PEDM with Rydberg states n . As illustrated in Figure 4.9(b), the PEDM varies between different Rydberg states. In particular, it increases at $n = 39$ compared to the two lower Rydberg states. A graphical analysis shows, that for different Rydberg states n an increasing trend of the PEDM in the range of $n = 27$ to 39 towards $n = 41$ can be found. As discussed above, there is little literature examining the scaling of the PEDM of S-type Rydberg molecules with ν . Our experimental results are contradicting the analysis of [60], where a $1/\nu^2$ decreasing trend was observed for Rb.

The increasing trend of the PEDM towards $n = 41$ is probably a hint towards the mechanism of dipole moment formation that was described in the introduction to PEDMs of Rydberg molecules. The enhanced mixing of states with different parities increasing towards the state $n = 41$ is probably mapped on the PEDM formation. Therefore, it can be concluded that the PEDM has the potential to serve as an effective tool for demonstrating MCQDT-related effects in a novel manner.

Towards Rydberg nonlinear quantum optics

This chapter establishes a connection to the introduction, offers insight into field of Rydberg polaritons physics and illustrates associated phenomena. The two fundamental concepts under consideration are electromagnetically induced transparency and the Rydberg blockade. In the ensuing two sections, both phenomena will be discussed in brief, with the discussion supported by measurements obtained with single-photon counters and a simulation.

Electromagnetically induced transparency (EIT). The first building block leading to the concept of nonlinear quantum optics is EIT. The two-photon excitation and the in previous chapters used Raman-excitation path is introduced in figure 2.5. In contrast to the Raman-excitation, the "EIT"-case refers to an excitation with Control and Probe detunings $\Delta_P = \Delta_C = \delta \rightarrow 0$. EIT arises due to the destructive interference of absorption pathways of two dressed-state resonances [10]. This leads to a reduction of population in the intermediate state $|e\rangle$. The effect of an EIT-medium on a weak Probe light field, assuming a strong Control light field, is given by the susceptibility

$$\begin{aligned} \chi_{\text{EIT}} = \chi_0 & \left(\frac{4\delta(|\Omega_C|^2 - 4\delta\Delta_P) - 4\Delta_P\gamma_{13}^2}{||\Omega_C|^2 + (\gamma_{12} + i2\Delta_P)(\gamma_{13} + i2\delta)|^2} \right. \\ & \left. + i \frac{8\delta^2\gamma_{12} + 2\gamma_{13}(|\Omega_C|^2 + \gamma_{13}\gamma_{12})}{||\Omega_C|^2 + (\gamma_{12} + i2\Delta_P)(\gamma_{13} + i2\delta)|^2} \right) \quad [10, 79], \end{aligned} \quad (5.1)$$

where $\chi_0 = (|\mu_{eg}|^2 N)/(\epsilon_0 \hbar V)$, N is the amount of atoms contained in the volume V , μ_{eg} the transition dipole matrix element, Δ_P is the Probe detuning, and γ_{12} and γ_{13} the dephasing between $|g\rangle$ and $|e\rangle$ and $|g\rangle$ and $|r\rangle$.

In the experiment, EIT can be observed in the transmission T of photons. The transmission of light in a medium can be expressed by using the imaginary part of χ and can be modeled by

$$T = \exp\left(-\frac{\text{OD}\gamma_{21}}{2} \cdot \text{Im}(\chi/\chi_0)\right) \quad [10, 39]. \quad (5.2)$$

Here, OD denotes optical density. For $\Delta_C = 0$ the equation 5.2 has a local maximum at $\delta = 0$. This means that in this case, despite being fully resonant to the strong single-photon absorption (which without a control beam leads to a complete absorption of the Probe photons), one can observe a transmission of

the Probe photons. The level of transmission depends on the OD, γ_{21} and γ_{13} . In the experiment, one can increase the transmission of the Probe photons by increasing the control power while keeping the single-photon absorption constant.

The experimental data in figure 5.1 is fitted to the theoretical model, as outlined in equation 5.1, demonstrating a high degree of agreement. The EIT's features are revealed at two distinct control powers (cf. 5.1(a) and 5.1(b))

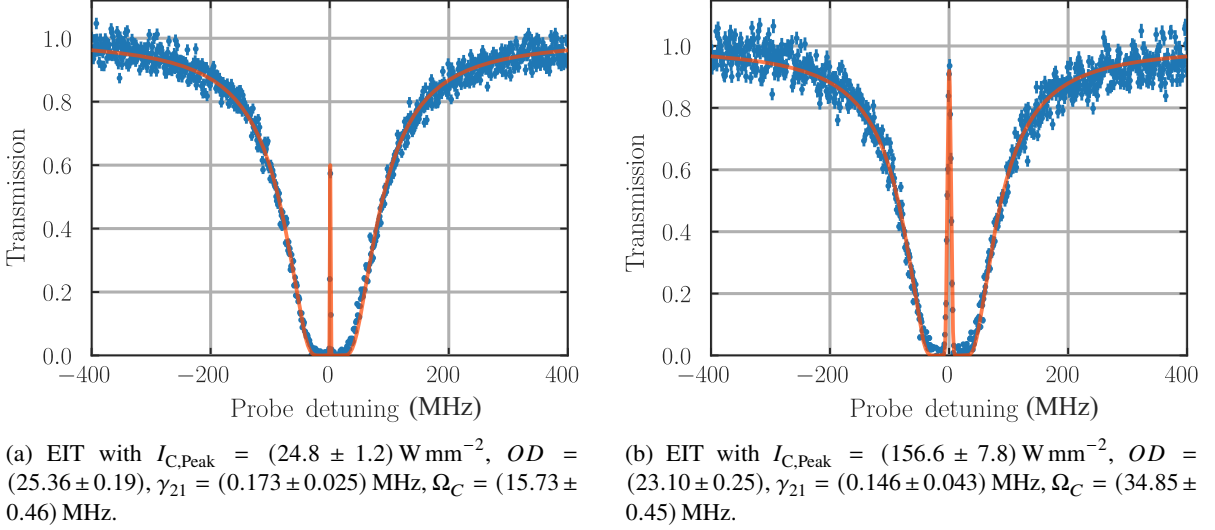


Figure 5.1: Measured electromagnetically induced transparency (EIT) in the weak Probe limit. The probe detuning Δ_P is varied and the Control detuning is set to $\Delta_C = 0$. The intensity is calculated from a Control power measurement and a beam waist of $\omega_0 = 16 \mu\text{m}$. The measurement was done at a low density, the OD reduces in the second picture due to Control beam induced heating. A higher control Intensity increases the transparency around the Probe detuning $\Delta_P = 0$. Eq. 5.1 was fitted to the data. The Rabi frequency Ω_C obtained from the fit scales approximately with $\sqrt{I_{C,Peak}}$ as for the in this figure shown measurements follows: $\sqrt{I_{C,Peak,low}} / \sqrt{I_{C,Peak,high}} = (0.391 \pm 0.014) \approx \Omega_{C,low} / \Omega_{C,high} = (0.451 \pm 0.015)$. Deviations are probably to too little sampling of the EIT-peak, or a not perfect fit.

In contrast to the imaginary part of χ , that determines the transmission $T(x)$, the real part can be connected to the refractive index n [5], and via the dispersion relation to the group velocity v_{gr} of the Probe photons in the medium according to

$$v_{group} = \left. \frac{d\omega_p}{dk_p} \right|_{\delta=0} = \frac{c}{n + \omega_p \frac{dn}{d\omega_p}} \quad \text{with} \quad n = \sqrt{1 + \text{Re}[\chi]} \quad [10]. \quad (5.3)$$

Here, ω_p and k_p are quantities of the Probe light. In EIT conditions, so when $\delta = 0$ and $\Delta_p = 0$, the $\text{Re}[\chi]$ shows a steep slope resulting in a small v_{gr} . The slope $\frac{dn}{d\omega_p}$ increases with decreasing Ω_C [10]. It can be deduced that a significant decrease in group velocities is to be expected on the EIT resonance at lower Control powers. Therefore, demonstrating a delay of light in the atomic medium is another visualization of EIT. A qualitatively measured slow light effect is presented in figure 5.2(a). A Control power dependent delay of the Probe pulse up to $0.4 \mu\text{s}$ was measured. Due to the fact that this was not the primary focus of this thesis, a more in-depth investigation was not pursued. Future exploration

could include more suitable pulse shapes, e.g. a Gaussian instead of the used Tukey-shape, to make the delay effect better distinguishable from noise and effects that lead to pulse distortion. In order to achieve even lower group velocities v_{gr} , a more substantial reduction in control Power in combination with a high atomic density could be implemented. Reference [11] demonstrates a reduction of v_{gr} down to 17 m s^{-1} in a Na Bose condensate. The low group velocity leads to an effective compression of the Probe photon pulse in the medium by the factor $v_{\text{gr}}/c_{\text{vac}}$ and the energy of the photons is temporarily stored in the medium as dark-state polaritons [10, 39]. The slow light effect contributes to storage and retrieval experiments of photons [39].

Rydberg blockade. The second building block of nonlinear quantum optics is the Rydberg blockade and its implications in the interaction between individual Rydberg polaritons.

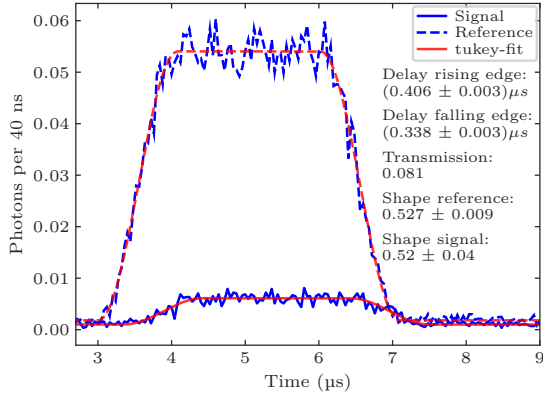
The high polarizability (scaling with v^7 [6], as demonstrated in figure 3.10(a)) makes Rydberg atoms very sensitive to external fields [9]. For Rydberg S-states follows: Even though single Rydberg atoms have no dipole moment without an applied field, two atoms may interact via a second-order effect of dipole-dipole interaction resulting in a van-der-Waals interaction potential $V(R) \propto \frac{C_6}{R^6}$ with a coefficient $C_6 \propto n^{11}$ [9]. If the corresponding required additional energy for a Rydberg excitation succeeds the line width of the involved transitions and lasers, effectively the atomic ensemble around a Rydberg excitation is tuned out of resonance in a blockaded sphere with radius r_b [7, 8]. In the Raman-case (assuming $|\Delta_P| \gg 0$ and classical Probe field Ω_P) follows

$$r_b = \left(\frac{C_6}{\hbar\Omega_{\text{eff}}} \right)^{\frac{1}{6}} \quad [9].$$

If a prepared atom cloud with N atoms is fully in the blockaded volume of any single Rydberg excitation in this cloud, this many particle state can be reduced to a simpler model - a Rydberg Superatom [9]. The model of a ideal Superatom is effectively a two-level system, consisting of a state with all atoms in $|g\rangle$, and a superposition state of all possible single excitations $|r\rangle$ while all other atoms being in $|g\rangle$. Preparing a dense atom cloud, and not only a single atom, yields the big advantage of a collectively enhanced the coupling of a photon and the cloud. Superatoms are already studied extensively [9, 80].

The model of a single Superatom can not be applied to the YQO experiment. Our atomic cloud can contain in axial direction multiple Rydberg excitations as the cloud is an order of magnitude longer than the blockade radius r_b . An estimation of the order of magnitude on how many Rydberg excitations could fit into the atomic cloud prepared in the YQO-setup is illustrated for one specific set of experimental conditions with a classical Monte-Carlo simulation in figure 5.2(b). The blockade radius strongly depends on the C_6 -coefficient and the Rabi-frequency Ω_{eff} . The C_6 -coefficient shows resonances around $n = 55$ and $n = 97$, visible as vertical stripes in figure 5.2(b). The Rabi-frequency Ω_{eff} for a detuning Δ_P and a Rydberg state n is determined by the choice of power (photon number) of Probe and Control, but also depends on the atom position in the atomic cloud relative to the Gaussian beam. For state with the highest C_6 -coefficient, that can form $n = 97$ approximately a maximal number of 10 Rydberg excitations can form a fully blockaded ensemble under the specific conditions of the simulation.

If a few-photon Probe pulse is sent under EIT conditions into such an ensemble, an interaction of the polaritons in the cloud can occur and will be mapped onto the transmitted photons. This paves the way to Rydberg nonlinear quantum optics with our YQO setup.



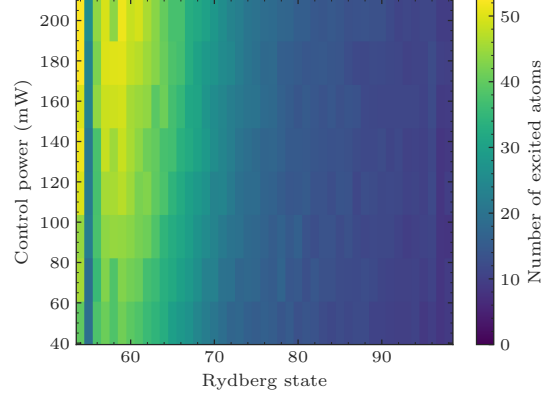
(a) Slow light demonstration. The reference pulse was taken without atoms, the signal pulse with atoms. The signal pulse experiences EIT and is delayed. A Tukey pulse^a was fitted to the data. The shape does not change significantly, but both edges of the pulse pick up a significant delay, that increases with decreasing Control power (or transmission of EIT). Only one measurement is presented here. The discrepancy of rising and falling edge might arise through pulse distortion effects related to Rabi oscillations or blockade physics. A simple estimation yields the following result: A photon delay of $0.4 \mu\text{s}$ in a $50 \mu\text{m}$ long, homogeneous medium would correspond to a light group velocity of 125 m s^{-1} in the medium.

^a The here used Tukey pulse $T(t)$ function is defined as

$$T(t, a, b, r, t_0, t_1) = \begin{cases} b, & t < t_0 \\ a \cdot L_{\text{Tukey}}\left(\frac{t-t_0}{t_1-t_0}, r\right) + b, & t_0 \leq t < t_1 \\ b, & t \geq t_1 \end{cases}$$

where a is the amplitude, b is the background level, r is the taper ratio (or shape parameter), t_0, t_1 are the start and end times of the pulse, $L_{\text{Tukey}}(x, r)$ is the Tukey window function. $L_{\text{Tukey}}(x, r)$ is defined as:

$$L_{\text{Tukey}}(x, r) = \begin{cases} \frac{1}{2} \left[1 + \cos\left(\frac{2\pi}{r} \left(x - \frac{r}{2}\right)\right) \right], & 0 \leq x < \frac{r}{2} \\ 1, & \frac{r}{2} \leq x < 1 - \frac{r}{2} \\ \frac{1}{2} \left[1 + \cos\left(\frac{2\pi}{r} \left(x - 1 + \frac{r}{2}\right)\right) \right], & 1 - \frac{r}{2} \leq x \leq 1 \\ 0, & \text{otherwise} \end{cases}$$



(b) Monte Carlo simulation of Rydberg excitations in the atomic cloud. The simulation gives answer to the question: If a weak Probe pulse is sent into the atomic cloud with fixed experimental conditions, what is the maximum number of Rydberg excitations that would fit into the atomic cloud with the densest packing possible assuming a classical blocked sphere with radius r_b around each Rydberg atom. The atomic cloud is assumed to be a cigar-shaped, gaussian distribution of $N = 10^4$ atoms with $\sigma_z = 60 \mu\text{m}$ and $\sigma_r = 10 \mu\text{m}$. The beam waists are $\omega_{0,p} = 8 \mu\text{m}$ and $\omega_{0,C} = 45 \mu\text{m}$. The Control power is varied and the Probe photon number is set to $N_{\text{Probe Photons}} = 5$ in a 10 micro/second long pulse. The simulation operates at a Raman-transition with $\Delta_P = -\Delta_C = 1 \text{ GHz}$ and $\delta = 0$. The simulation does many repetitions of a simulated Probe pulses. In each step, each atom tries a transition to a Rydberg state with a probability proportional to the Rabi-frequency Ω_{eff} at the atoms position. Ω_{eff} is calculated in 3-dimensions with eq. 2.2. The excitation of an atom is only permitted under the following conditions: The atom in question is not within the blocked sphere of another existing Rydberg atom. Another Rydberg atom is not within the blocked sphere of the Rydberg atom in question. The size of the blocked sphere is given by the blockade radius r_b from equation 5. Next to an excitation, in each step also a deexcitation is possible with a probability proportional to the Rabi-frequency Ω_{eff} . This allows a rearrangement of excitations towards the most efficient packing. After 10 to 20 repetitions, the simulation reaches a steady state with the maximum number of Rydberg excitations. In total 40 repetitions are performed. The maximal number of excitations is calculated by a mean of the last repetitions. More details can be found in appendix B.

Figure 5.2: Demonstration towards Rydberg nonlinear quantum optics.

Conclusions

During my thesis work, I worked on the Ytterbium-Quantum-Optics (YQO) experiment. To recapitulate: The main objective of the YQO experiment is to explore Rydberg nonlinear quantum optics by using ultra-cold atoms of the earth-alkaline-like species ytterbium (^{174}Yb).

Summary of this work. A core part of this thesis covers the upgrade of the YQO experiment by means of an ion detection system. The system has been utilized for the investigation of atomic and molecular Rydberg physics with ytterbium (^{174}Yb).

In section 2.3.2, I introduced a system to detect Rydberg atoms, consisting of two components: The electric field control, which provides after the optimization process pulsed electric fields up to 75 V cm^{-1} with a high stability and short rise time of 30 ns to ionize the Rydberg atoms and the Microchannel Plate that offers a high detection efficiency ($\eta > 50 \%$). The high signal-to-noise ratio of this detection scheme paired with the ability to do pulsed experiments with a repetition rate of up to 10 kHz facilitates rapid data acquisition and versatile usage in spectroscopy applications. This is demonstrated in chapters 3 and 4.

My contributions to the exploration of the atomic properties of ytterbium (^{174}Yb) are presented in chapter 3. On the one hand, ionization mechanisms were explored: For the ionization of high Rydberg excitations ($n > 51$) - as will be used in the context of future nonlinear quantum optics experiments - ionization via field ionization has been identified as the predominant mechanism. However, ionization for Rydberg states far below the semi-classically calculated field ionization threshold has been observed, with a measured ionization efficiency of 0.5 % at states around $n = 30$. The detection scheme for Rydberg atoms presented in this thesis can be utilized to study Rydberg states down to this limit. On the other hand, building upon the later observation, high precision spectroscopy was performed to characterize AC- and DC-Stark shifts. The resulting polarizabilities of different Rydberg states demonstrate a similar trend with a reference (cf. fig. 3.10(b)).

I also contributed to the first major application of the ion detection system: The sensitive, state-selective detection of the Rydberg atom population enabled the acquisition of a large data set of Rydberg molecule spectra at different densities (cf. fig. 4.5). A comparison to theory will allow the extraction of fundamental properties of the ^{174}Yb electron-neutral scattering in the low energy regime. In section 4.3, I present the formation of different classes of polyatomic Rydberg molecules (dimers, trimers, etc.). The dimer state in the outermost potential well was identified across different Rydberg states. In section 4.4, the permanent dipole moment of ^{174}Yb Rydberg molecules is modeled and estimated to approximately 1 Debye.

All in all, my main contribution to the **YQO** experiment was the successful development of a highly sensitive, state-selective detection system based on ionization and its application in several measurements to explore Rydberg physics of ytterbium.

Future use of the ion detection system. In the future, the ion detection system will support many experimental tasks towards the main goal of the **YQO** experiment to demonstrate nonlinear quantum optics based on ytterbium. Chapter 5 contains the first steps towards the demonstration of Rydberg nonlinear quantum optics, such as **EIT**.

The detection of probe photons is a fundamental tool in the investigation of **EIT**, the study of photon correlations, and the execution of storage and retrieval experiments [5, 9]. Next to that, the ion detection system provides a novel perspective on the Rydberg dynamics in the medium.

The ion detection system can quantify the Rydberg population present within the atomic cloud. This can be used, for example, to characterize how close an atomic cloud is to being completely blockaded, similar to reference [81], where the blockade of atomic Rb ensembles was demonstrated. For this purpose, a methodology analogous to the one outlined in section 2.3.2.3 could be employed to align the ion counts and the actual Rydberg excitations. One challenge that remains here is the nonlinearity of the detector (cf. fig. 2.20). A potential method of circumventing this limitation involves tuning the **MCP** to a lower detection efficiency, characterizing the detector at a state with a low C_6 -coefficient, and subsequently transitioning to a higher Rydberg state to demonstrate the blockade.

Another possible application could be the position-resolved detection of Rydberg excitations in atomic clouds, similar to reference [82]. Here, a most probable separation between two adjacent Rydberg Superatoms was found for a chain of Superatoms. In the neighboring experiment **RQO**, which has a similar experimental setup, a spatially resolved ion spectroscopy was already performed to detect Rydberg population position-resolved in dimple traps [83]. In the **YQO** experiment this can be also implemented: A separate, highly focused 369 nm laser is planned to be used to drive transitions from Rydberg states to auto-ionizing states. This can be used to ionize Rydberg polaritons in the cloud position dependent. The ion detection system presented in this thesis has the capacity to detect the aforementioned ions, thereby facilitating the reconstruction of the polariton density within the atomic cloud. The additional application of weak electric fields before the ionization could be used to modify the initial positions of photoionized ions, thereby introducing a position-dependent delay on the ions. This could facilitate the mapping of the position of a Rydberg atom to the arrival time on the **MCP**.

Additionally, the ion detection system can assist the further characterization of the consequences of the deposition of free charges by the two-photon ionization via the Control light (cf. fig. 3.8). Similar to Rydberg excitations, free ions will also cause a blockade effect in the cloud [84]. This affects all experiments that are based on the concept of Rydberg polaritons.

Finally, the ion detection system was demonstrated to be a highly effective tool for conducting precise, low-noise spectroscopy with minimal need for a high repetition rate of experimental cycles. This will offer great benefits for quicker characterizations and tuning of the experiments precisely to atomic resonances or to any other state of operation.

Appendix: Details on fitting Rydberg molecule spectra

Fits for the peak position estimation

In fig. 4.6 the positions of peaks in many spectra are presented.

The process of fitting is exemplary discussed in sec. 4.3 for $n = 42$. In these fits a lot of decisions are made by me, e.g.: How to choose the used line shape, how to choose an initial guess, whether it makes sense to correct the deadtime-nonlinearity, and what density to choose. These decisions might introduce systematical errors and a confirmation bias. The well aligned dimer states in the outermost potential well suggest, that we can trust also the positions of all other peaks. In particular, I would like to point out two points, that are challenging.

- For each state, data for many different densities exist. For each fit one has to make a decision whether low or high density will lead to a more precise result. Low densities will induce uncertainty on the peak position determination due to a low signal. High densities will give rise to formation of trimers. In general, I choose intermediate to high densities. At higher densities, a coupled model has to be used to capture all peaks. The amount of free parameters is reduced by using a coupled model. In the range $n = 40$ to 43 , it makes sense to fit dimers and trimers. Additional dimer peaks can even attribute to the position determination, as the dimer and trimer positions are coupled. How to choose which peaks are assigned to be a dimer or trimer, is explained in detail in chap. 4.3. In the following, I did not include some very small and broad peaks, even though they are clearly identifiable as a dimer. In the following fit examples, some of the spectra include two densities to help distinguishing N -mer classes. At $n = 45$, many N -mers have to be included. This leads to overfitting of the ($N > 2$)-mers, but the position determination is given mostly by the more intense dimer peaks, and therefore still possible to a good extent. An even further reduction of free parameters is not possible with the theoretical knowledge we have so far.
- The choice of line-shape is less relevant for peaks with a high binding energy, as these are well distinct and have little overlap to each other. These peaks can be modeled well with a Lorentzian. This was done for all $n < 41$. Peaks close to the atomic transition and with narrowly spaced binding energy gain an additional uncertainty on the peak position. The approach to model peaks with a double Lorentzian sum line shape is demonstrated for $n = 42$ in chap. 4.3. In general, this

approach is done as following: To the blue and about 20 % to the red of the atomic transition a model consisting of two lorentzians with the same position and a coupled amplitude and width is fitted. Once the amplitude and width ratios are fixed, this line shape is used with a global amplitude and width for all lines. This approach clearly has several limitations since it is an optimization of the model based on observation and not on physics. Firstly, fitting all peaks with the same line shape might neglect the changing strength of molecular state dependent and density dependent broadening mechanisms, e.g. broadening by the finite lifetime. The lifetime of molecular states is highly individual for every state and at different densities the lifetime is reduced by inelastic collisions. Secondly, the significant skewedness of the atomic transition can not be compensated, due to the highly nonlinear density decay during the pulses. This affects most significantly very shallow bound states. Thirdly, to enable fitting the same curve to each peak requires a precise knowledge on the ion count height. To compensate for technical effects, the deadtime-nonlinearity calibration can be used (cf. sec. 2.3.2.3). The correction is limited by the fact, that some counts of the atomic transition go even above the valid range of the in this thesis performed deadtime-nonlinearity calibration (only up to ≈ 4 ion counts). This can not be corrected quantitatively correctly! Additionally, the calibration assumes that the shape of the ion pulse is constant for all observed spectra. This is obviously not perfectly given, since the ionization (time) dynamics are quite complex (cf. sec. 3.1.2).

The fit results look still acceptable and well matching. A comparison to a working theory model will make it possible to identify potentially misidentified or not identified peaks.

All fit results

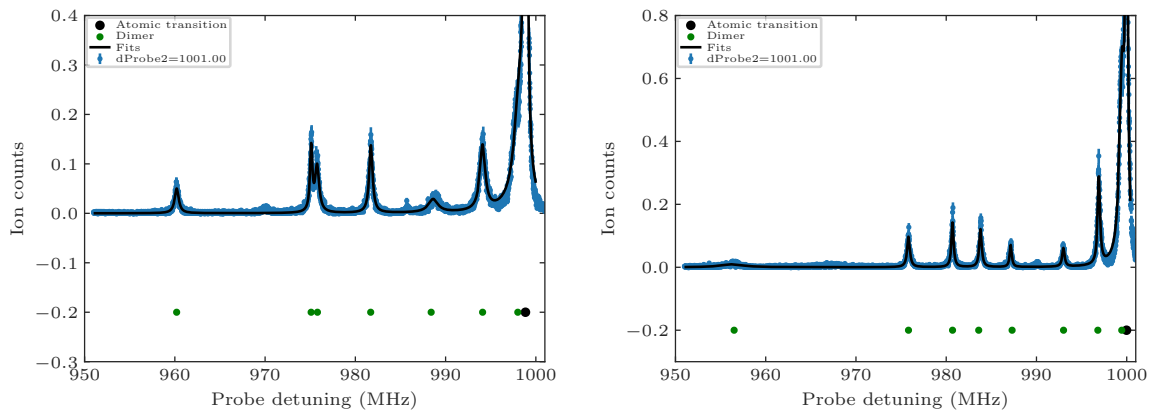


Figure A.1: Spectra for Rydberg states $n = 32$ and 33 .

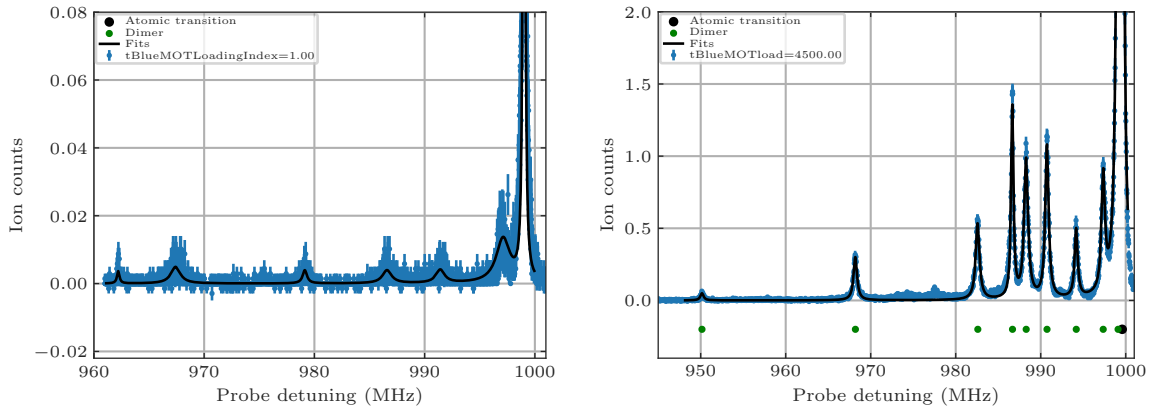


Figure A.2: Spectra for Rydberg states $n = 30$ and 35 . For $n = 30$ only dimers were fitted.

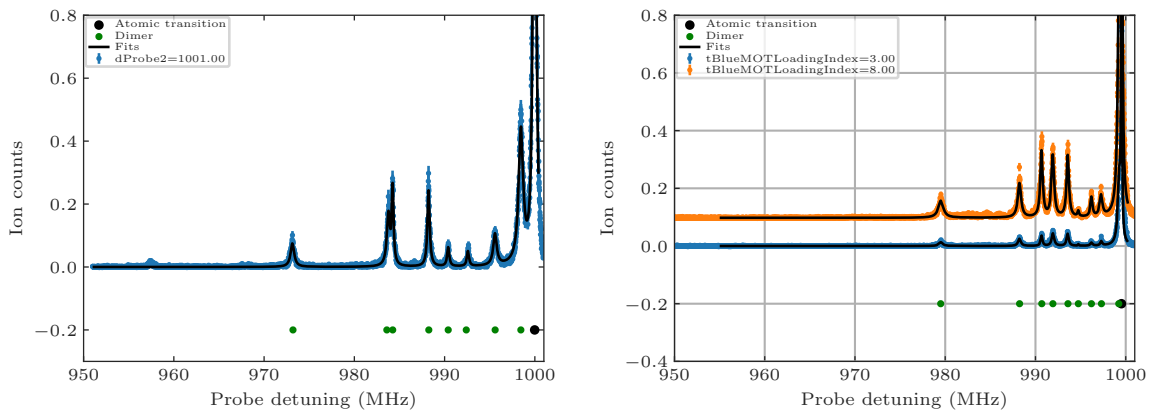


Figure A.3: Spectra for Rydberg states $n = 34$ and 37 . For $n = 34$, the leftmost peak is harmonic to the first and third peak from the right. It was not fitted here as dimer, even if trimer formation is unlikely at this n .

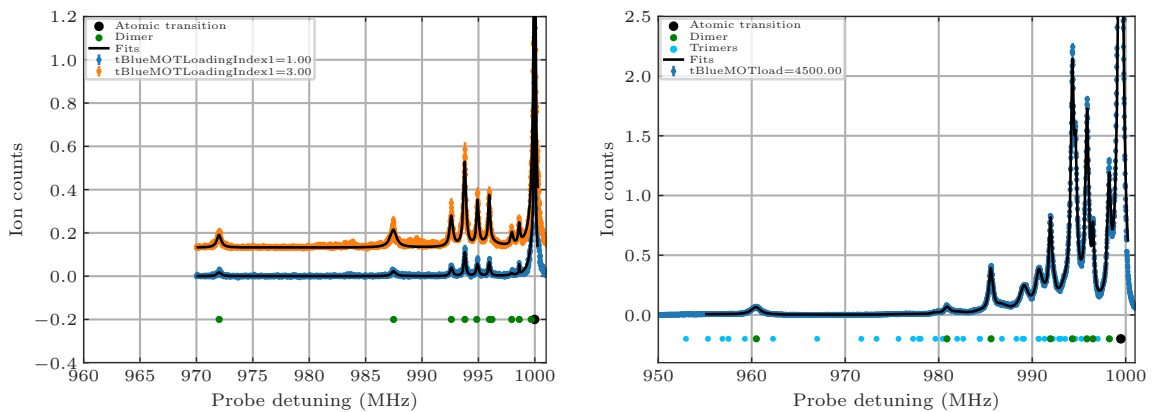


Figure A.4: Spectra for Rydberg states $n = 39$ and 40 .

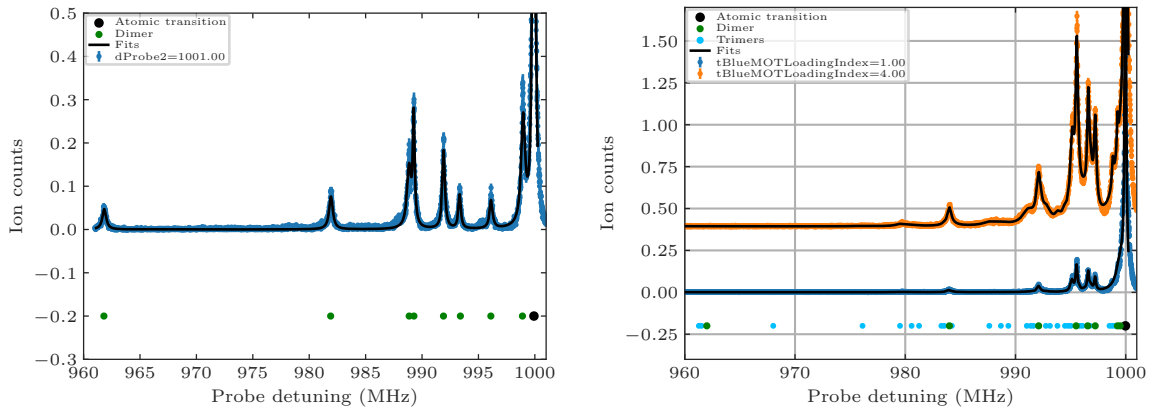


Figure A.5: Spectra for Rydberg states $n = 36$ and 41 .

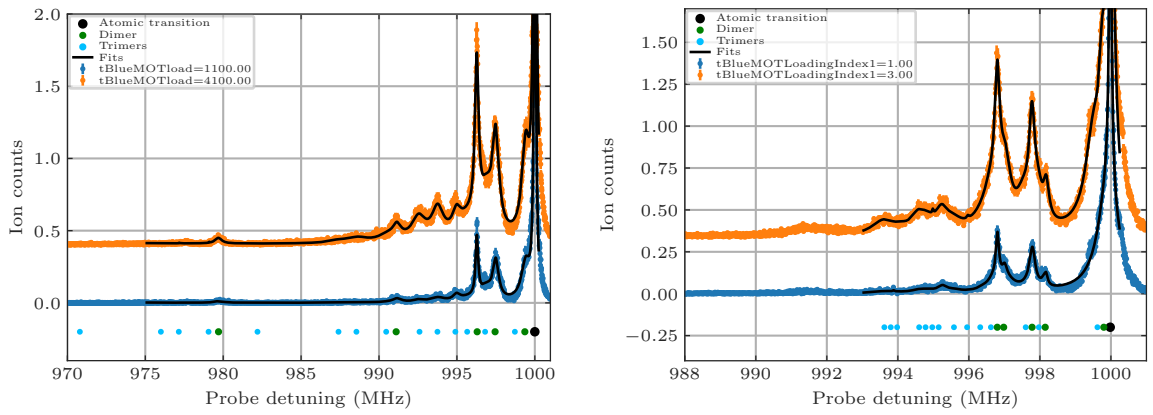


Figure A.6: Spectra for Rydberg states $n = 42$ and 43 .

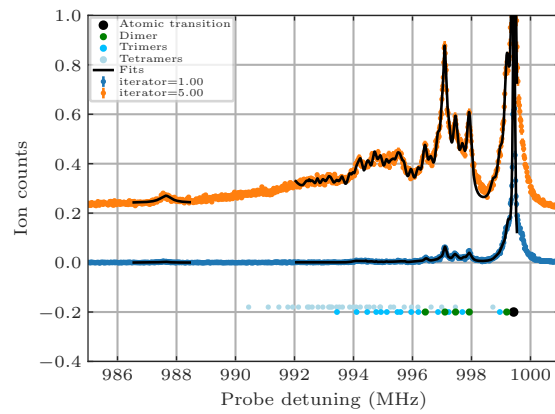


Figure A.7: Spectra for Rydberg states $n = 45$.

Overview of all scan hyper parameters to trace back the raw data

Table A.1: Overview of all density scans, the used iterator is in the legend of the figures.

n	Date	Scannums
35	2025/01/13	1–210
37	2025/01/24	362–805
40	2025/01/10	2862–4018
42	2025/01/21	17–243
45	2025/01/17	237–986
41	2025/02/07	1–646
30	2025/02/21	6–348
43	25/02/26	48-145, 184 - 318
39	25/02/27	193-422
36	2025-03-01	2192-2735
32	2025-03-04	1-393,
33	2025-03-09	1-338
34	2025-03-11	High 536-812

Fits of broadening of peaks in an electric field

Next to $n = 37$, the broadening of molecular spectra in electric fields was measured and fitted for $n = 35$ and $n = 39$. Details on the fitting routine are mentioned in the sec. 4.4. For the two fits below no deadtime-nonlinearity calibration was done, as for these spectra this step did not improve the fit, $n = 39$ has quite high ion counts above the valid range of the deadtime-nonlinearity calibration

For the first two fields, the fit agrees quite well, for high fields, in both states very broadened peaks on the red side lead to a background at the right edge of the fit range (given by the solid line). This leads to a shift of the center frequency of the fit, that is not according to the linear Stark shift. These higher field measurement will not be further used. Steps on the further evaluation of the fits can be found in sec. 4.4, too.

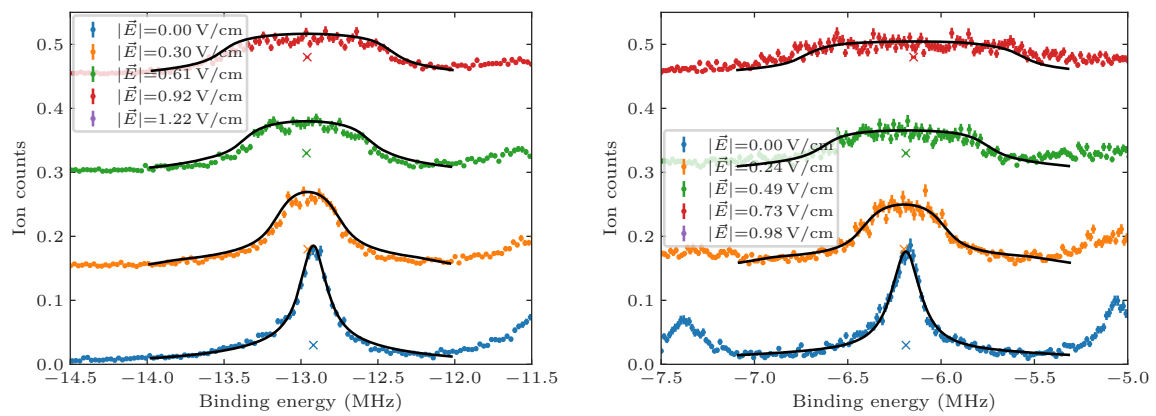


Figure A.8: Fits of the broadened spectra for Rydberg states $n = 35$ and 39 .

Details on the Rydberg excitation in a cloud simulation

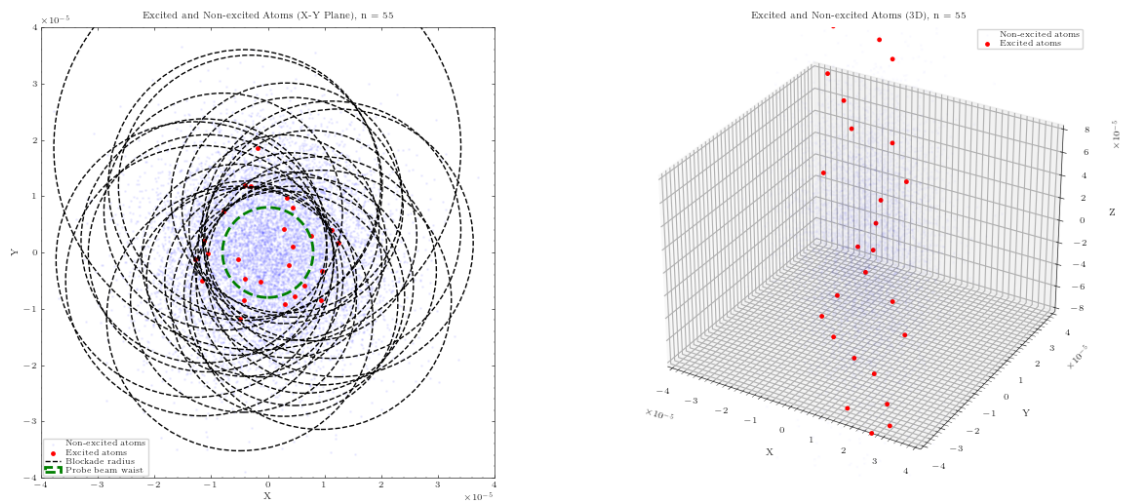


Figure B.1: Visualization of the simulated Rydberg excitation of atoms in 2D and 3D for $n = 55$ and the parameters stated below fig. 5.2(b).

On the right side in figure B.1, the atomic cloud is shown in three dimensions. Here, the Z-axis is the propagation of the Probe and Control beams and the cigar shaped atomic cloud. Here one limit of this classical simulation is visible. Due to the repeated excitations until full saturation of the cloud with excitations, also atoms in the Gaussian tails of the atomic cloud can be excited. In a one pulse experiment, these low density regions would not couple to light strongly and contribute significantly to total number. In a next iteration step of this simulation this could be taken into account.

On the left side in figure B.1, one sees a radial cut through the atomic cloud. The blockade radius is dependent on the position of the atom relative to the probe beam waist due to the changing Rabi frequency.

The total effective Rabi frequency (cf. eq. 2.2) is determined by the individual Rabi frequencies Ω_P and Ω_C . In general, Ω is given by the product of the electric field \vec{E} and the dipole matrix element d . The reduced dipole matrix elements to the Rydberg state were provided by Frederic Hummel, the reduced dipole matrix element of the Probe transition $6s^2\ ^1S_0 \rightarrow 6s6p\ ^1P_1$ is given by the equation, that connects the spontaneous decay rate of a fine-structure transition with the reduced matrix element (cf. eq. 7.305 in ref. [48]). The full matrix elements were obtained by multiplying with the corresponding Clebsch-Gordon-Coefficient $1\sqrt{3}$ of the 1S_0 to 1P_1 state. In the left plot, the size of the probe waist is drawn. The varying Probe power across the cloud causes a change of Rydberg blockade radii.

Additional, an interesting effect is visible: The excitation seem to avoid in this snapshot, that represents the densest packing, the center of the probe beam - despite the highest Rabi frequency in the center. Apparently, this arrangement represents the most efficient packaging. Whether this effect would be observed in the experiment too is unclear.

Bibliography

- [1] A. G. J. MacFarlane, J. P. Dowling, and G. J. Milburn, *Quantum technology: the second quantum revolution*, *Philosophical Transactions of the Royal Society of London. Series A: Mathematical, Physical and Engineering Sciences* **361** (2003), Publisher: Royal Society S. 1655–1674, URL: <https://royalsocietypublishing.org/doi/10.1098/rsta.2003.1227> (visited on 04/23/2025) (cit. on p. 1).
- [2] F. Flamini, N. Spagnolo, and F. Sciarrino, *Photonic quantum information processing: a review*, *Reports on Progress in Physics* **82** (2018), Publisher: IOP Publishing S. 016001, issn: 0034-4885, URL: <https://dx.doi.org/10.1088/1361-6633/aad5b2> (visited on 04/23/2025) (cit. on p. 1).
- [3] C. Murray and T. Pohl, “Chapter Seven - Quantum and Nonlinear Optics in Strongly Interacting Atomic Ensembles”, *Advances In Atomic, Molecular, and Optical Physics*, ed. by E. Arimondo, C. C. Lin, and S. F. Yelin, vol. 65, Academic Press, 2016 S. 321–372, URL: <https://www.sciencedirect.com/science/article/pii/S1049250X1630009X> (visited on 08/25/2024) (cit. on p. 1).
- [4] D. E. Chang, V. Vuletić, and M. D. Lukin, *Quantum nonlinear optics — photon by photon*, *Nature Photonics* **8** (2014), Publisher: Nature Publishing Group S. 685–694, issn: 1749-4893, URL: <https://www.nature.com/articles/nphoton.2014.192> (visited on 04/23/2025) (cit. on p. 1).
- [5] O. Firstenberg, C. S. Adams, and S. Hofferberth, *Nonlinear quantum optics mediated by Rydberg interactions*, *Journal of Physics B: Atomic, Molecular and Optical Physics* **49** (2016), Publisher: IOP Publishing S. 152003, issn: 0953-4075, URL: <https://dx.doi.org/10.1088/0953-4075/49/15/152003> (visited on 08/25/2024) (cit. on pp. 1, 63, 67).
- [6] T. Gallagher, “Rydberg Atoms”, *Springer Handbook of Atomic, Molecular, and Optical Physics*, ed. by G. Drake, New York, NY: Springer, 2006 S. 235–245, isbn: 978-0-387-26308-3, URL: https://doi.org/10.1007/978-0-387-26308-3_14 (visited on 03/08/2025) (cit. on pp. 1–3, 28, 64).
- [7] M. D. Lukin et al., *Dipole Blockade and Quantum Information Processing in Mesoscopic Atomic Ensembles*, *Physical Review Letters* **87** (2001), Publisher: American Physical Society S. 037901, URL: <https://link.aps.org/doi/10.1103/PhysRevLett.87.037901> (visited on 04/10/2025) (cit. on pp. 1, 64).
- [8] E. Urban et al., *Observation of Rydberg blockade between two atoms*, *Nature Physics* **5** (2009) S. 110–114, issn: 1745-2473, 1745-2481, URL: <https://www.nature.com/articles/nphys1178> (visited on 07/25/2024) (cit. on pp. 1, 64).
- [9] J. Kumlin et al., *Quantum optics with Rydberg superatoms*, *Journal of Physics Communications* **7** (2023) S. 052001, issn: 2399-6528, URL: <https://iopscience.iop.org/article/10.1088/2399-6528/acd51d> (visited on 07/25/2024) (cit. on pp. 1, 10, 64, 67).
- [10] M. Fleischhauer, A. Imamoglu, and J. P. Marangos, *Electromagnetically induced transparency: Optics in coherent media*, *Reviews of Modern Physics* **77** (2005) S. 633–673, issn: 0034-6861, 1539-0756, URL: <https://link.aps.org/doi/10.1103/RevModPhys.77.633> (visited on 07/25/2024) (cit. on pp. 1, 62–64).
- [11] L. V. Hau, S. E. Harris, Z. Dutton, and C. H. Behroozi, *Light speed reduction to 17 metres per second in an ultracold atomic gas*, *Nature* **397** (1999) S. 594–598, issn: 0028-0836, 1476-4687, URL: <https://www.nature.com/articles/17561> (visited on 04/09/2025) (cit. on pp. 1, 64).

Bibliography

- [12] M. Fleischhauer and M. D. Lukin, *Dark-State Polaritons in Electromagnetically Induced Transparency*, *Physical Review Letters* **84** (2000), Publisher: American Physical Society S. 5094–5097, URL: <https://link.aps.org/doi/10.1103/PhysRevLett.84.5094> (visited on 04/09/2025) (cit. on p. 1).
- [13] J. D. Pritchard et al., *Cooperative Atom-Light Interaction in a Blockaded Rydberg Ensemble*, *Physical Review Letters* **105** (2010), Publisher: American Physical Society S. 193603, URL: <https://link.aps.org/doi/10.1103/PhysRevLett.105.193603> (visited on 08/25/2024) (cit. on p. 1).
- [14] Y. O. Dudin and A. Kuzmich, *Strongly Interacting Rydberg Excitations of a Cold Atomic Gas*, *Science* (2012), Publisher: American Association for the Advancement of Science, URL: <https://www.science.org/doi/10.1126/science.1217901> (visited on 08/25/2024) (cit. on p. 1).
- [15] H. Busche et al., *Contactless nonlinear optics mediated by long-range Rydberg interactions*, *Nature Physics* **13** (2017), Publisher: Nature Publishing Group S. 655–658, issn: 1745-2481, URL: <https://www.nature.com/articles/nphys4058> (visited on 04/24/2025) (cit. on p. 1).
- [16] X. Wang et al., *Two-color ytterbium magneto-optical trap in a compact dual-chamber setup*, *Physical Review Applied* **23** (2025), Publisher: American Physical Society S. 014004, URL: <https://link.aps.org/doi/10.1103/PhysRevApplied.23.014004> (visited on 03/03/2025) (cit. on pp. 1, 4–6).
- [17] P. Lunt, *Design and Construction of a new ultracold Ytterbium Experiment for Rydberg Physics*, Master: University of Southern Denmark, 2019 (cit. on pp. 1, 4, 10, 52).
- [18] M. Moos, M. Höning, R. Unanyan, and M. Fleischhauer, *Many-body physics of Rydberg dark-state polaritons in the strongly interacting regime*, *Physical Review A* **92** (2015) S. 053846, issn: 1050-2947, 1094-1622, URL: <https://link.aps.org/doi/10.1103/PhysRevA.92.053846> (visited on 07/25/2024) (cit. on p. 1).
- [19] M. J. Gullans et al., *Effective Field Theory for Rydberg Polaritons*, *Physical Review Letters* **117** (2016), Publisher: American Physical Society S. 113601, URL: <https://link.aps.org/doi/10.1103/PhysRevLett.117.113601> (visited on 04/09/2025) (cit. on p. 1).
- [20] B. Zhao et al., *A millisecond quantum memory for scalable quantum networks*, *Nature Physics* **5** (2009), Publisher: Nature Publishing Group S. 95–99, issn: 1745-2481, URL: <https://www.nature.com/articles/nphys1153> (visited on 04/24/2025) (cit. on p. 2).
- [21] T. Kuwamoto, K. Honda, Y. Takahashi, and T. Yabuzaki, *Magneto-optical trapping of Yb atoms using an intercombination transition*, *Physical Review A* **60** (1999), Publisher: American Physical Society R745–R748, URL: <https://link.aps.org/doi/10.1103/PhysRevA.60.R745> (visited on 03/29/2025) (cit. on p. 2).
- [22] S. Uetake, A. Yamaguchi, D. Hashimoto, and Y. Takahashi, *High-resolution laser spectroscopy of ultracold ytterbium atoms using spin-forbidden electric quadrupole transition*, *Applied Physics B* **93** (2008) S. 409–414, issn: 1432-0649, URL: <https://doi.org/10.1007/s00340-008-3225-x> (visited on 04/24/2025) (cit. on p. 2).
- [23] V. A. Dzuba, V. V. Flambaum, and S. Schiller, *Testing physics beyond the standard model through additional clock transitions in neutral ytterbium*, *Physical Review A* **98** (2018), Publisher: American Physical Society S. 022501, URL: <https://link.aps.org/doi/10.1103/PhysRevA.98.022501> (visited on 04/24/2025) (cit. on p. 2).
- [24] M. Kleinert, M. E. Gold Dahl, and S. Bergeson, *Measurement of the Yb I $S_{0} \rightarrow P_{1}$ transition frequency at 399 nm using an optical frequency comb*, *Physical Review A* **94** (2016), Publisher: American Physical Society S. 052511, URL: <https://link.aps.org/doi/10.1103/PhysRevA.94.052511> (visited on 04/24/2025) (cit. on p. 2).
- [25] U. Griesmann et al., *Photoionization cross sections of doubly excited resonances in ytterbium*, *Journal of Physics B: Atomic, Molecular and Optical Physics* **25** (1992) S. 1393–1404, issn: 0953-4075, 1361-6455, URL: <https://iopscience.iop.org/article/10.1088/0953-4075/25/7/011> (visited on 02/18/2025) (cit. on pp. 2, 29, 32, 34, 36).

Bibliography

- [26] M. Peper et al., *Spectroscopy and Modeling of ^{171}Yb Rydberg States for High-Fidelity Two-Qubit Gates*, *Physical Review X* **15** (2025), Publisher: American Physical Society S. 011009, URL: <https://link.aps.org/doi/10.1103/PhysRevX.15.011009> (visited on 04/03/2025) (cit. on pp. 2, 4, 28, 42, 43, 58).
- [27] S. Weber et al., *Calculation of Rydberg interaction potentials*, *Journal of Physics B: Atomic, Molecular and Optical Physics* **50** (2017), Publisher: IOP Publishing S. 133001, ISSN: 0953-4075, URL: <https://dx.doi.org/10.1088/1361-6455/aa743a> (visited on 03/18/2025) (cit. on pp. 2, 3, 28, 32, 42, 43).
- [28] B. C. Yang and F. Robicheaux, *Field ionization of Rydberg atoms in a single-cycle pulse*, *Physical Review A* **91** (2015) S. 043407, ISSN: 1050-2947, 1094-1622, URL: <https://link.aps.org/doi/10.1103/PhysRevA.91.043407> (visited on 03/08/2025) (cit. on pp. 2, 28, 30, 31).
- [29] M. T. Schlagmüller, *A single Rydberg Atom interacting with a Dense and Ultracold Gas*, PhD thesis: Universität Stuttgart, 2016 (cit. on pp. 2, 30–32, 34).
- [30] V. C. Gregoric et al., *Improving the state selectivity of field ionization with quantum control*, *Physical Review A* **98** (2018), Publisher: American Physical Society (APS), ISSN: 2469-9926, 2469-9934, URL: <https://link.aps.org/doi/10.1103/PhysRevA.98.063404> (visited on 03/29/2025) (cit. on pp. 2, 30, 31).
- [31] C. Veit et al., *Pulsed Ion Microscope to Probe Quantum Gases*, *Physical Review X* **11** (2021), Publisher: American Physical Society S. 011036, URL: <https://link.aps.org/doi/10.1103/PhysRevX.11.011036> (visited on 04/24/2025) (cit. on p. 2).
- [32] M. Walker, “The Rise and Fall of an Aryan Physicist”, *Nazi Science: Myth, Truth, and the German Atomic Bomb*, ed. by M. Walker, Boston, MA: Springer US, 1995 S. 5–40, ISBN: 978-1-4899-6074-0, URL: https://doi.org/10.1007/978-1-4899-6074-0_2 (visited on 03/28/2025) (cit. on p. 2).
- [33] H. J. Metcalf and P. v. d. Straten, *Laser cooling and trapping of atoms*, *JOSA B* **20** (2003), Publisher: Optica Publishing Group S. 887–908, ISSN: 1520-8540, URL: <https://opg.optica.org/josab/abstract.cfm?uri=josab-20-5-887> (visited on 03/03/2025) (cit. on p. 4).
- [34] C. J. Foot, *Atomic Physics*, 1st ed., vol. 7, Oxford master series on atomic, optical and laser physics, Oxford: University Press, 2004, ISBN: 978-0-19-152314-4 (cit. on p. 4).
- [35] W. D. Phillips, J. V. Prodan, and H. J. Metcalf, *Laser cooling and electromagnetic trapping of neutral atoms*, *JOSA B* **2** (1985), Publisher: Optica Publishing Group S. 1751–1767, ISSN: 1520-8540, URL: <https://opg.optica.org/josab/abstract.cfm?uri=josab-2-11-1751> (visited on 04/16/2025) (cit. on p. 4).
- [36] J. Dalibard and C. Cohen-Tannoudji, *Laser cooling below the Doppler limit by polarization gradients: simple theoretical models*, *Journal of the Optical Society of America B* **6** (1989) S. 2023, ISSN: 0740-3224, 1520-8540, URL: <https://opg.optica.org/abstract.cfm?URI=josab-6-11-2023> (visited on 07/25/2024) (cit. on pp. 4, 5).
- [37] R. Grimm, M. Weidemüller, and Y. B. Ovchinnikov, *Optical dipole traps for neutral atoms*, 1999, arXiv: [physics/9902072](https://arxiv.org/abs/physics/9902072), URL: <http://arxiv.org/abs/physics/9902072> (visited on 07/25/2024) (cit. on pp. 6, 7).
- [38] J. Kumlin et al., *Quantum optics with Rydberg superatoms*, *Journal of Physics Communications* **7** (2023), Publisher: IOP Publishing S. 052001, ISSN: 2399-6528, URL: <https://dx.doi.org/10.1088/2399-6528/acd51d> (visited on 03/03/2025) (cit. on p. 8).
- [39] I. Mirgorodskiy, *Storage and propagation of Rydberg polaritons in a cold atomic medium*, Accepted: 2018-01-29T15:11:47Z, doctoralThesis, 2017, URL: <http://elib.uni-stuttgart.de/handle/11682/9590> (visited on 08/26/2024) (cit. on pp. 10, 62, 64).

Bibliography

- [40] S. Johannes, *2014-Schmidt-Johannes-Generation-of-non-classical-light-using-ultra-cold-Rydberg-ensembles-MSc*, PhD thesis: Universität Stuttgart, 2014,
URL: <https://www.pi5.uni-stuttgart.de/documents/abgeschlossene-arbeiten/2014-Schmidt-Johannes-Generation-of-non-classical-light-using-ultra-cold-Rydberg-ensembles-MSc.pdf> (visited on 03/06/2025) (cit. on p. 10).
- [41] L. Robert, *2006-Loew-Robert-A-versatile-setup-for-experiments-with-Rubidium-Bose-Einstein-condensates-From-optical-lattices-to-Rydberg-matter-PhD*, PhD thesis: Universität Stuttgart, 2006,
URL: <https://www.pi5.uni-stuttgart.de/documents/abgeschlossene-arbeiten/2006-Loew-Robert-A-versatile-setup-for-experiments-with-Rubidium-Bose-Einstein-condensates-From-optical-lattices-to-Rydberg-matter-PhD.pdf> (visited on 03/06/2025) (cit. on p. 10).
- [42] *Hamamatsu Photonics K.K.: Hamamatsu MCP guide*, 2006,
URL: https://wiki.nqo.uni-bonn.de/images/Hamamatsu_MCP_guide.pdf (visited on 02/06/2025) (cit. on pp. 16, 17, 19).
- [43] *Hamamatsu Photonics K.K.: MCP F4655-13 ASSEMBLY Guide*, 2021,
URL: https://www.hamamatsu.com/content/dam/hamamatsu-photonics/sites/documents/99_SALES_LIBRARY/etd/MCP_assembly_TMCP0003E.pdf (visited on 02/06/2025) (cit. on pp. 16, 24).
- [44] P. Wangyang et al., *Advances in Schottky parameter extraction and applications*, *Journal of Materials Science & Technology* **218** (2025) S. 317–335, ISSN: 1005-0302,
URL: <https://www.sciencedirect.com/science/article/pii/S1005030224008727> (visited on 03/06/2025) (cit. on p. 18).
- [45] S. Instruments, *Time Tagger Series Brochure*, 2024,
URL: <https://www.swabianinstruments.com/static/downloads/TimeTaggerSeries.pdf> (visited on 02/23/2025) (cit. on p. 22).
- [46] A. Patil, *Dead time and count loss determination for radiation detection systems in high count rate applications*, Doctoral Dissertations (2010), URL: https://scholarsmine.mst.edu/doctoral_dissertations/2148 (cit. on p. 24).
- [47] G. Reinaudi, T. Lahaye, Z. Wang, and D. Guéry-Odelin, *Strong saturation absorption imaging of dense clouds of ultracold atoms*, *Optics Letters* **32** (2007), Publisher: Optica Publishing Group S. 3143–3145, ISSN: 1539-4794,
URL: <https://opg.optica.org/ol/abstract.cfm?uri=ol-32-21-3143> (visited on 04/16/2025) (cit. on p. 27).
- [48] D. A. Steck, *Quantum and Atom Optics*, 0.16.2, 2024 (cit. on pp. 28, 40, 43, 51, 75).
- [49] F. Hummel et al., *Engineering Rydberg-pair interactions in divalent atoms with hyperfine-split ionization thresholds*, *Physical Review A* **110** (2024), Publisher: American Physical Society S. 042821,
URL: <https://link.aps.org/doi/10.1103/PhysRevA.110.042821> (visited on 03/29/2025) (cit. on p. 28).
- [50] H. J. Korsch and R. Möhlenkamp, *Field ionization of Rydberg atoms: A semiclassical treatment of complex energy states in intense electric fields*, *Zeitschrift für Physik A Atoms and Nuclei* **314** (1983) S. 267–273, ISSN: 0939-7922,
URL: <https://doi.org/10.1007/BF01412921> (visited on 03/08/2025) (cit. on p. 28).
- [51] J. Hofbrucker, *Two-photon ionization of many-electron atoms*, (2020), ISBN: 9781701146112,
URL: https://www.db-thueringen.de/receive/dbt_mods_00044410 (visited on 02/18/2025) (cit. on p. 35).
- [52] H. B. Bebb, *Quantitative Theory of the Two-Photon Ionization of the Alkali Atoms*, *Physical Review* **149** (1966) S. 25–32, ISSN: 0031-899X,
URL: <https://link.aps.org/doi/10.1103/PhysRev.149.25> (visited on 12/03/2024) (cit. on pp. 35, 38, 39).
- [53] W. Zernik, *Two-Photon Ionization of Atomic Hydrogen*, *Physical Review* **135** (1964) A51–A57, ISSN: 0031-899X,
URL: <https://link.aps.org/doi/10.1103/PhysRev.135.A51> (visited on 12/03/2024) (cit. on pp. 38, 39).
- [54] P. Lambropoulos and M. R. Teague, *Two-photon ionization with spin-orbit coupling*, *Journal of Physics B: Atomic and Molecular Physics* **9** (1976) S. 587, ISSN: 0022-3700,
URL: <https://dx.doi.org/10.1088/0022-3700/9/4/009> (visited on 03/10/2025) (cit. on pp. 38, 39).

Bibliography

- [55] J. Mitroy, M. S. Safronova, and C. W. Clark, *Theory and applications of atomic and ionic polarizabilities*, *Journal of Physics B: Atomic, Molecular and Optical Physics* **43** (2010) S. 202001, ISSN: 0953-4075, URL: <https://dx.doi.org/10.1088/0953-4075/43/20/202001> (visited on 03/02/2025) (cit. on p. 40).
- [56] F. B. Dunning, S. K. Kanungo, and S. Yoshida, *Ultralong-range Rydberg molecules*, *Journal of Physics B: Atomic, Molecular and Optical Physics* **57** (2024), Publisher: IOP Publishing S. 212002, ISSN: 0953-4075, URL: <https://dx.doi.org/10.1088/1361-6455/ad7459> (visited on 03/28/2025) (cit. on p. 46).
- [57] J. P. Shaffer, S. T. Rittenhouse, and H. R. Sadeghpour, *Ultracold Rydberg molecules*, *Nature Communications* **9** (2018), Publisher: Nature Publishing Group S. 1965, ISSN: 2041-1723, URL: <https://www.nature.com/articles/s41467-018-04135-6> (visited on 03/14/2025) (cit. on pp. 46, 48).
- [58] S. Bai et al., *Cesium $nDJ + 6S1/2$ Rydberg molecules and their permanent electric dipole moments*, *Physical Review Research* **2** (2020) S. 033525, ISSN: 2643-1564, URL: <https://link.aps.org/doi/10.1103/PhysRevResearch.2.033525> (visited on 03/23/2025).
- [59] M. Althön, M. Exner, R. Blättner, and H. Ott, *Exploring the vibrational series of pure trilobite Rydberg molecules*, *Nature Communications* **14** (2023), Publisher: Nature Publishing Group S. 8108, ISSN: 2041-1723, URL: <https://www.nature.com/articles/s41467-023-43818-7> (visited on 03/13/2025) (cit. on p. 57).
- [60] W. Li et al., *A Homonuclear Molecule with a Permanent Electric Dipole Moment*, *Science* **334** (2011), Publisher: American Association for the Advancement of Science S. 1110–1114, URL: <https://www.science.org/doi/full/10.1126/science.1211255> (visited on 03/13/2025) (cit. on pp. 46, 58, 61).
- [61] D. Booth, S. T. Rittenhouse, J. Yang, H. R. Sadeghpour, and J. P. Shaffer, *Production of trilobite Rydberg molecule dimers with kilo-Debye permanent electric dipole moments*, *Science* **348** (2015), Publisher: American Association for the Advancement of Science S. 99–102, URL: <https://www.science.org/doi/10.1126/science.1260722> (visited on 03/28/2025) (cit. on p. 46).
- [62] C. H. Greene, A. S. Dickinson, and H. R. Sadeghpour, *Creation of Polar and Nonpolar Ultra-Long-Range Rydberg Molecules*, *Physical Review Letters* **85** (2000), Publisher: American Physical Society S. 2458–2461, URL: <https://link.aps.org/doi/10.1103/PhysRevLett.85.2458> (visited on 03/14/2025) (cit. on pp. 46, 48, 57).
- [63] V. Bendkowsky et al., *Observation of ultralong-range Rydberg molecules*, *Nature* **458** (2009), Publisher: Nature Publishing Group S. 1005–1008, ISSN: 1476-4687, URL: <https://www.nature.com/articles/nature07945> (visited on 03/14/2025) (cit. on pp. 46, 48).
- [64] A. Gaj et al., *From molecular spectra to a density shift in dense Rydberg gases*, *Nature Communications* **5** (2014), Publisher: Nature Publishing Group S. 4546, ISSN: 2041-1723, URL: <https://www.nature.com/articles/ncomms5546> (visited on 08/28/2024) (cit. on pp. 46, 54, 56).
- [65] V. Bendkowsky et al., *Rydberg Trimers and Excited Dimers Bound by Internal Quantum Reflection*, *Physical Review Letters* **105** (2010), Publisher: American Physical Society S. 163201, URL: <https://link.aps.org/doi/10.1103/PhysRevLett.105.163201> (visited on 01/27/2025) (cit. on p. 46).
- [66] B. Butscher et al., *Atom–molecule coherence for ultralong-range Rydberg dimers*, *Nature Physics* **6** (2010), Publisher: Nature Publishing Group S. 970–974, ISSN: 1745-2481, URL: <https://www.nature.com/articles/nphys1828> (visited on 03/14/2025) (cit. on p. 46).
- [67] A. Gaj et al., *Hybridization of Rydberg Electron Orbitals by Molecule Formation*, *Physical Review Letters* **115** (2015), Publisher: American Physical Society S. 023001, URL: <https://link.aps.org/doi/10.1103/PhysRevLett.115.023001> (visited on 03/14/2025) (cit. on p. 46).
- [68] B. J. DeSalvo et al., *Ultra-long-range Rydberg molecules in a divalent atomic system*, *Physical Review A* **92** (2015), Publisher: American Physical Society S. 031403, URL: <https://link.aps.org/doi/10.1103/PhysRevA.92.031403> (visited on 03/14/2025) (cit. on pp. 46, 48, 49).

Bibliography

- [69] F. Camargo et al., *Lifetimes of ultra-long-range strontium Rydberg molecules*, *Physical Review A* **93** (2016), Publisher: American Physical Society S. 022702, URL: <https://link.aps.org/doi/10.1103/PhysRevA.93.022702> (visited on 03/28/2025) (cit. on p. 46).
- [70] J. D. Whalen et al., *Heteronuclear Rydberg molecules*, *Physical Review A* **101** (2020), Publisher: American Physical Society S. 060701, URL: <https://link.aps.org/doi/10.1103/PhysRevA.101.060701> (visited on 03/28/2025) (cit. on p. 46).
- [71] V. Bendkowsky, *Diss_VeraBendkowsky*, PhD thesis: Universität Stuttgart, 2010, URL: https://elib.uni-stuttgart.de/bitstream/11682/4944/1/Diss_VeraBendkowsky.pdf (visited on 08/28/2024) (cit. on p. 48).
- [72] W. Demtröder, *Experimentalphysik 3*, Springer-Lehrbuch, Berlin, Heidelberg: Springer, 2016, ISBN: 978-3-662-49093-8 978-3-662-49094-5, URL: <http://link.springer.com/10.1007/978-3-662-49094-5> (visited on 03/14/2025) (cit. on p. 48).
- [73] V. A. Dzuba and G. F. Gribakin, *Correlation-potential method for negative ions and electron scattering*, *Physical Review A* **49** (1994), Publisher: American Physical Society S. 2483–2492, URL: <https://link.aps.org/doi/10.1103/PhysRevA.49.2483> (visited on 03/14/2025) (cit. on p. 48).
- [74] J. B. Balewski, *A single electron in a Bose-Einstein condensate*, PhD thesis: Universität Stuttgart, 2014, URL: https://wiki.nqo.uni-bonn.de/images/Jonathan_Balewski_-_PhD_%282014%29.pdf (visited on 03/14/2025) (cit. on p. 48).
- [75] C. Fey, F. Hummel, and P. Schmelcher, *Ultralong-range Rydberg molecules*, *Molecular Physics* **118** (2020) e1679401, ISSN: 0026-8976, URL: <https://doi.org/10.1080/00268976.2019.1679401> (visited on 04/24/2025) (cit. on pp. 49, 55).
- [76] K. M. Jones, E. Tiesinga, P. D. Lett, and P. S. Julienne, *Ultracold photoassociation spectroscopy: Long-range molecules and atomic scattering*, *Reviews of Modern Physics* **78** (2006) S. 483–535, ISSN: 0034-6861, 1539-0756, URL: <https://link.aps.org/doi/10.1103/RevModPhys.78.483> (visited on 03/22/2025) (cit. on p. 52).
- [77] J. M. Nipper, *Interacting Rydberg atoms: Coherent control at Förster resonances and polar homonuclear molecules*, PhD thesis: Universität Stuttgart, 2012, URL: <https://elib.uni-stuttgart.de/items/05845682-d2be-4619-b4c0-d11bf99c6f8c> (cit. on pp. 57, 58).
- [78] R. G. Littlejohn, *Physics 221A - The Stark Effect in Hydrogen and Alkali Atoms*, 2019, URL: <https://bohr.physics.berkeley.edu/classes/221/0708/notes/stark.pdf> (visited on 04/20/2025) (cit. on p. 58).
- [79] C. Tresp, *Rydberg polaritons and Rydberg superatoms - novel tools for quantum nonlinear optics*, (2017), URL: <http://nbn-resolving.de/urn:nbn:de:bsz:93-opus-ds-90863> (visited on 03/03/2025) (cit. on p. 62).
- [80] J. Zeiher et al., *Microscopic Characterization of Scalable Coherent Rydberg Superatoms*, *Physical Review X* **5** (2015) S. 031015, ISSN: 2160-3308, URL: <https://link.aps.org/doi/10.1103/PhysRevX.5.031015> (visited on 07/25/2024) (cit. on p. 64).
- [81] N. Stiesdal et al., *Controlled multi-photon subtraction with cascaded Rydberg superatoms as single-photon absorbers*, *Nature Communications* **12** (2021), Publisher: Nature Publishing Group S. 4328, ISSN: 2041-1723, URL: <https://www.nature.com/articles/s41467-021-24522-w> (visited on 04/23/2025) (cit. on p. 67).
- [82] J. Du, T. Vogt, N. Zheng, and W. Li, *Imaging a Chain of Rydberg Superatoms Enabled by Förster-Resonance-Enhanced Interaction*, 2024, arXiv: 2404.00274[quant-ph], URL: <http://arxiv.org/abs/2404.00274> (visited on 04/10/2025) (cit. on p. 67).
- [83] N. Stiesdal, *Collective atom-light interactions with Rydberg superatoms*, (2022), Publisher: Syddansk Universitet. Det Naturvidenskabelige Fakultet, URL: <https://portal.findresearcher.sdu.dk/en/publications/kollektive-interaktioner-mellem-lys-og-atomer-med-rydberg-superat> (visited on 04/23/2025) (cit. on p. 67).

Bibliography

- [84] F. Engel et al., *Observation of Rydberg Blockade Induced by a Single Ion*, *Physical Review Letters* **121** (2018), Publisher: American Physical Society S. 193401, URL: <https://link.aps.org/doi/10.1103/PhysRevLett.121.193401> (visited on 04/23/2025) (cit. on p. 67).

List of Abbreviations

¹⁷⁴Yb Ytterbium-174 [v](#), [3–28](#), [32](#), [34](#), [36](#), [38](#), [39](#), [41](#), [44](#), [46](#), [52–54](#)

EIR Rydberg Excitations to Detected Ions Ratio [23](#), [24](#), [29](#), [30](#)

EIT Electromagnetically induced transparency [4](#)

HQO Hybrid Quantum Optics Experiment [22](#)

HV High Voltage [5](#), [14](#), [15](#)

MCP Microchannel plate [v](#), [5](#), [12](#), [13](#), [16–20](#), [22](#), [23](#), [25](#), [29](#), [32](#)

MCQDT Multi-Channel Quantum Defect Theory Model [41](#)

MOT Magneto-optical Trap [6–9](#), [34](#)

PA Photoassociation [48](#)

PEDM Permanent Electric Dipole Moment [54](#), [55](#), [57](#)

RFI Rydberg Atom Field Ionization [25](#), [34](#)

TPI Two-photon ionization [23](#), [25](#), [32–38](#)

ULRM Ultralong-Range Rydberg Molecules [44](#)

Acknowledgement

Almost three years ago, I joined the NQO group as a bachelor student, and now I've completed my master's project in the same group. I would like to thank everyone - both inside and outside the group - for their support during this long journey, both on a professional and personal level. Sebastian, thank you for making it possible for me to do this Master's thesis within the group and for inspiring me over the past three years - starting with the Quantum Optics lecture! I also appreciate the attention you gave to the YQO project and for sending me to DPG and YAO. Thanks to Daqing Wang for supporting me as a second supervisor!

To the YQO gang - Eduardo Urunuela, Xin Wang, and Tangi Legrand - thank you for giving me the opportunity to work on our experiment, for teaching me how to run it, and for helping me hunt down its bugs. Tangi, thank you for your guidance and support in so many ways. Xin, thank you for teaching me to trust my intuition in the lab - you're the fastest Rydberg state changer ever! Eduardo, thank you for helping me stay organized and approach problems thoroughly. I'm hoping you'll share some more tips with me in the future, like how to use my bialetti properly. Thanks to FYQOLers Ludwig and Knut! And also Wayne for the fun time in the lab. Thanks to the rest of the crew in the lab: Majestix, Obelix, Gutemine, Asterix, Idefix, Adrenaline, Grienoline, Praline, and Blinix, who acted mostly mannerly and well-behaved. Thanks to Wolfgang Alt for sharing your knowledge in such a constructive, helpful and patient way. Thanks to all the proofreaders. Thanks to Matt Eiles and Milena Simić for their theoretical support. Special thanks to my old HQO family, in which I started my Bachelor project, the RQO team, the FCOLers, and Tina for all the shared lunches¹, the cake days (and weeks), and for the nice, uplifting daily atmosphere! Thanks to all members of the [Nonlinear Quantum Optics Group](#) =)



I'd also like to thank all my friends who've been there for me during the last five years of my physics studies. It was an intense but also exciting and cool time. To my family, Kristin, Lucas, Tassilo, Papa and Mama: Thank you for supporting me and always showing me the right way. Your trust and encouragement are always a great source of security for me.

¹ I agree, early lunch is the better lunch! ;)